Design and Implementation of a Microparticle Delivery Device for the Cornea

Thesis by
Dennis Lok Ko

In Partial Fulfillment of the Requirements for the
Degree of
Doctor of Philosophy

CALIFORNIA INSTITUTE OF TECHNOLOGY
Pasadena, California

2024
Defended December 8, 2023

Dennis Lok Ko
ORCID: 0000-0001-8700-0844

ACKNOWLEDGEMENTS

There are not enough words to thank Julie Kornfield for everything over the years. I would not be here without you. You fought for me to be at Caltech and let me fulfill my dream of getting an education here. In the times when I needed someone to lean on the most, you were always there for me. To me, you will always represent the best of Caltech.

Thank you to the Department of Chemical Engineering at Caltech and to my committee members David Tirrell, Mark Davis, Mikhail Shapiro, and Mory Gharib. Thank you to Bala Ambati for teaching me about the cornea and drug delivery.

Thank you to the members of the Kornfield group. Thank you to Raj Mukkamala for being in the office with me while I worked late into the night, and helping me learn LaTeX (this thesis only looks nice because of you). Thank you to Jin Mo Koo for sharing the bio-area space with me and teaching me about bio-related things. Thank you to Rohit Srikanth for never saying no when I needed help and being always down to try new things with me — I wish the high speed camera worked! To Jacque Tawney, Soudabeh Saeid, Akash Dhawan, and Paresh Samantaray, thank you for all the encouragement and conversations we had in the lab. To past group members, thank you to Lealia Xiong for inspiring me with your thesis and your general aesthetic sense. Thank you to Priya Chittur for teaching me about the OCT and Imaris. Thank you to Matthew Mattson for mentoring me as a SURF student and getting me started with corneal research. Thank you to Joyce Huynh helping me get into Caltech for graduate school and for mentoring me. Thank you to Joey Kim, Dan Zhou, and Amy Fu. I want to thank the SURF students I had the privilege of working with: Tiffany Huang and Sinwook Lee. To everyone else that I may have missed, thank you.

Thank you to Alex Groisman at UCSD who taught me about this technology and graciously shared parts and ideas with me. Thank you to Ben Laccetti who also worked on particle delivery in the group.

Thank you to Therese Bagsit, Christine Jary, Abigail McCann, Kate Davies, Sarah Mojarad, and Marcy Fowler for helping me order supplies, schedule meetings with Julie, and generally make my life a bit easier.

Thank you to Candace Rypisi and Carol Casey from the SURF office for the opportunity to do three summer fellowships at Caltech.

None of this work would be possible without the help of the Caltech Machine Shop, namely, Mike Roy and Ricardo Zarazua. Thank you to Joe Drew for taking care of our workspace in Kornfield lab. Thank you to Sabhrant Sachan, Rosa Uribe, Thai Troung, and Yasho Bhawe.

Thank you to all the friends I made playing pickup basketball at Caltech, in particular Sagar Vaidyanathan, Mike Walker and Eric Li. Thank you to my high school friends who were there for me when I needed them the most: Brian Cheng and Paul Woo. Thank you to Jeff Kao and William Chang for playing golf with me at Brookside when I needed time outside the lab.

I would like to acknowledge the Caltech Women's Basketball team, where I was able to serve as an assistant coach during my time here at Caltech. I'd like to thank Sandra Marbut and Bridgette Reyes for giving me a chance to help coach the teams. Coaching the student-athletes at Caltech helped me find my voice as a teacher, communicator, and some of my best memories at Caltech were spent with the team. It was also cool to be part of the winningest team on record (2021–22, 11 wins). I want to acknowledge the friends I made while working on the team, in particular Jessica Watkins, Sarah Wright, Shannon Norton, and Grace Peng. And I want to acknowledge the seniors that graduated while I was here: Kate Lewis,

Michelle Wong, Stephanie Wong, Rachel Hess, Bridget Connor, Elizabeth Eiden, Nika Haleftiras, Madeline Schemel and Madelyn Stroder, Alexa Lauinger, Grace Peng, Lauren Suezaki, Sahana Saikumar, and Faith Pinney.

Special thank you to my cat, Penny.

Thank you to my mom, Jenny Lui, for always giving me the opportunity to get the best education and always supporting me all these years. And to my dad, Benjamin Ko, who only graduated from high school: this one's for you. I hope I made you proud.

To my wife, Lisa Yee, thank you. I could not have done this without you and your support. Meeting you has been the best thing that's ever happened to me.

ABSTRACT

[ABSTRACT PARTIALLY REDACTED]

Biolistic drug delivery offers an alternative path for delivering therapeutics into the cornea. Until now, none of the commercially available gene guns are suitable for clinical delivery of therapeutics due to tissue damage caused by high speed gas used to accelerate microparticles. Here, we demonstrated the use of a device that both eliminates the exit gas, only allowing high speed particles through, and one that works in a clinical setting.

Microparticles ranging from 5 to 22 µm were accelerated and delivered into both the agarose gels and *ex vivo* corneas. In gels, we found that normalized penetration depth was proportional to particle diameter and density. As the standoff distance between the device and the target increased, more particles were left stranded at the surface, as their penetrating power decreased, and their dispersion from the center of mass on the target increased. The orifice size served to control both the number of particles and the amount of exit gas. Increasing the inlet pressure did not a show significant increase in the penetration depth of microparticles.

In the cornea, we found that we were able to use our device to deliver particles into both the epithelium and the stroma, although only higher density particles were able to enter the stroma. There was little to no damage to the cornea due to particle delivery. If epithelial defects were detected in the cornea due to particle penetration, they were quickly resolved within 30 minutes. Our device demonstrated performance (penetration depth) comparable to previous biolistic delivery methods in the cornea, while also maintaining clinical relevance by eliminating exit gas flow.

TABLE OF CONTENTS

LIST OF ILLUSTRATIONS

LIST OF TABLES

Number *Page*

LIST OF SYMBOLS AND ABBREVIATIONS

$(L^*)_{M_1}$	length of tube required to reach M_1
$(L^*)_{M_2}$	length of tube required to reach M_2
$\bar{f}$	average friction factor
η	fluid viscosity
γ	ratio of heat capacities, C_p/C_v
μ_g	viscosity of the carrier gas
μ_t	tissue viscosity
μ_{He}	viscosity of Helium
ρ_t	density of target material
ρ_{He}	density of Helium
σ_y	yield stress of the target material
τ_v	hydrodynamic relaxation time
$\tau_{v,1}$	hydrodynamic relaxation time in Regime 1
$\tau_{v,2}$	hydrodynamic relaxation time in Regime 2
$\tau_{v,e}$	hydrodynamic relaxation time after exit
A_c	cross sectional area of the particle
C_c	slip correction factor
C_p	heat capacity at constant pressure
C_v	heat capacity at constant volume
D_H	hydraulic diameter of duct
d_{ICT}	diameter of inner capillary tube
F_d	drag force on particle

F_f	frictional or viscous resistance force
F_i	force caused by the inertia of the target material
F_y	yield force
L	length of tube
L^*	length required to reach Mach 1
M	Mach number
M_1	Mach number at position 1
M_2	Mach number at position 2
p_i	inlet pressure
Re_p	Reynold’s number of particle
Re_{ICT}	Reynold’s number of particle in the ICT
S	distance traveled by particle
S_∞	stopping distance of particle
T	temperature
u_g	gas velocity
$u_{p,e}$	particle exit velocity from device
$u_{p,i}$	particle impact velocity
z	axial position
z_b	length of tube
z_p	particle position
EY	Eosin Y
FIJI	Fiji is just ImageJ
GDU	Gas diversion unit
ICT	Inner capillary tube

OCT	Optical Coherence Tomography
OrD	Orifice disc
OrD-1	Orifice disc 1
OrD-2	Orifice disc 2
OrD-3	Orifice disc 3
UV	Ultraviolet
UVA	Ultraviolet-A

Chapter 1

INTRODUCTION

1.1 Microparticles as a method of drug delivery

Drugs improve health and extend lives. Their efficacy can often be increased and their side effects reduced by controlling the concentration of drug as a function of time and place in the body. For instance, the side effects of a specific therapeutic agent vary significantly with the method of administration, as this alters its path through the body and the inadvertent dose delivered to non-targeted tissues. Drug delivery systems are used to achieve controlled release transients and/or targeted delivery locations of therapeutic agents. Controlled release is used to maintain a therapeutic concentration of the drug over a sustained period of time. To mitigate side effects associated with systemic administration, drug delivery systems are often designed to intervene at the specific part of the body that is at risk or affected by a disease.

Among the four themes of current research in drug delivery—routes of delivery, delivery vehicles, cargo, and targeting strategies—the present thesis focuses on a particular route of delivery that allows us to quickly deliver a precise dose of drug to a precise location using high-speed particles. In contrast to various means of systemic administration (oral, inhalation, intravenous), high-speed particles provide direct, localized tissue-specific delivery. In contrast to transdermal delivery (or related oral patches), high-speed particles can provide precise control of the dose of drug that penetrates to a precise depth at a specific time. In contrast to subcutaneous injection, high-speed microparticles can be delivered with minimal pain or risk of infection.

Alternatives to injections

Intramuscular and subcutaneous (insulin) injection using a syringe and needle provide delivery of a precise dose at a specified location at a specific time. Despite the prevalence of this practice, there are several limitations to injections including bleeding, pain, risk of cross-infection, improper use/reuse of needles and syringes, low compliance, and needle phobia.[1,2,3] As a result, extensive research has been done on developing alternative routes to administer drugs and vaccines. They can be classified into four distinct categories: liquid-jet injections, powder needleless injections, topical applications, and mucosal application, which can then be further separated according to the routes the drug travels, including ocular, nasal, oral, pulmonary, vaginal, and rectal (Figure 1.1).[4] We will focus on the use of accelerated drug particles to penetrate the desired part of the body.

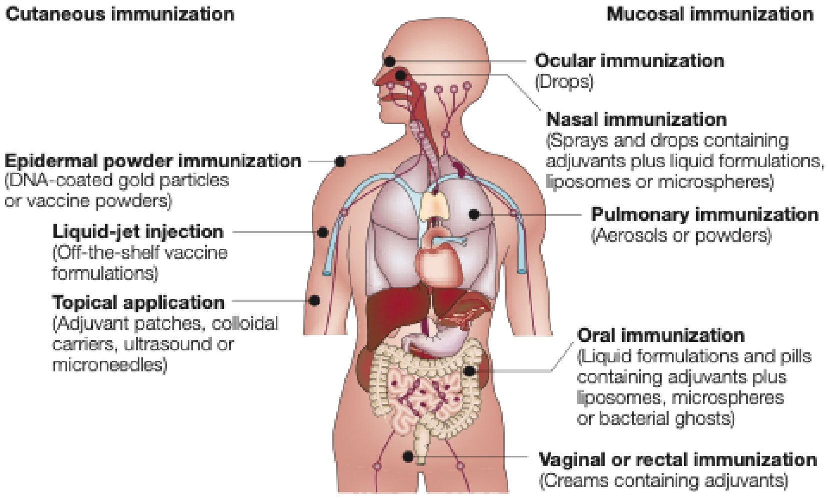

Figure 1.1: Various routes to administer drugs to the human body are shown: liquid-jet injection, epidermal powder immunization and topical application (cutaneous immunization by sprays, drops, aerosols, patches, capsules and creams), and mucosal administration (further classified into ocular nasal, oral, pulmonary, and vaginal or rectal). Reprinted with permission from Mitragotri.[4]

Historical perspective

Throughout history, humans have been fascinated by the use of airborne projectiles. Paleontologists believe that the earliest projectiles were used to hunt for food. Over the last several decades, the focus has shifted to micro-sized projectiles that have the ability to deliver therapeutic agents into the human body for curing diseases.

Ballistics (Greek: "to throw") is the study of the mechanics involved in the launching, flight, behavior, and effects of projectiles. The earliest evidence of projectiles were stone-tipped arrows discovered in South Africa that are approximately 64,000 years old.[5,6] Over the course of time, other projectiles were developed, primarily as ranged weapons. For example, these include the invention of archery (10,000 B.C.) and firearms (1,000 A.D.).[7,8] Ballistics theory has been traced back to Italian mathematician Niccolo Tartaglia in the 16th century.[9] Later, in the Middle Ages, studies of ballistic projectiles in biological tissues began as a way to model injuries. A remarkable development over the past four decades is the use of projectiles for benign purposes, delivering genes or vaccines to living cells and tissues.

1.2 Biolistics

In 1983, Cornell researcher John Sanford modified an air pistol to serve as a "gene gun," delivering DNA on the surface of dense tungsten particles (ca. 19.3 g/cm^3), a mere 400 nm or 800 nm in diameter.[10,11,12] Sanford loaded the carrier particles onto a plastic disc that was mounted at the end of the barrel of the air pistol such that the burst of Helium gas propelled the disc into a mesh "stopping screen" causing the disc to abruptly stop and launch the carrier particles toward the tissue of interest (Figure 1.2). These particles were coated with a marker gene targeted for the cells of onions and the genetic transformation was confirmed when the onion tissue expressed the gene (with greater rate of transfection for 400 nm than 800 nm diameter carrier particles). Further development by Bio-Rad led to the two current variants of the gene gun: the PDS-1000/He System and the Helios Gene Gun (Table 1.1).[13]

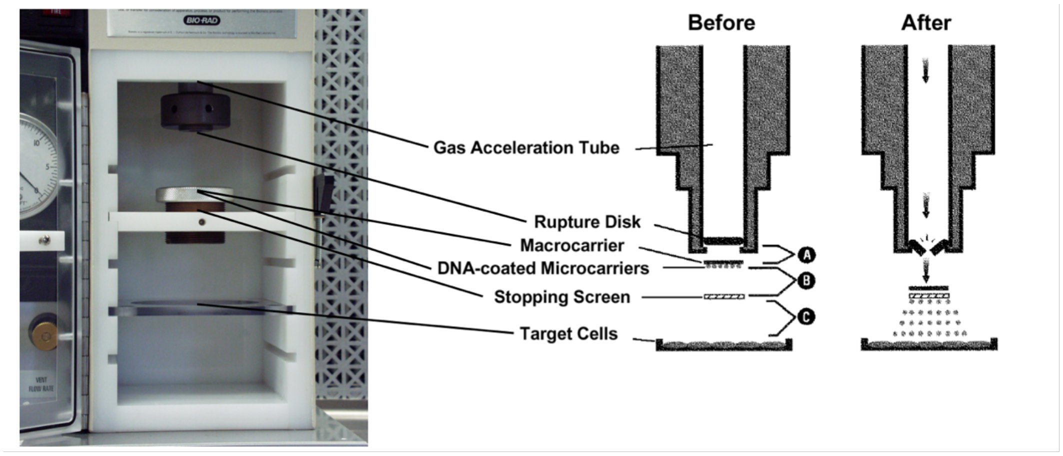

Figure 1.2: Schematic for the Bio-Rad PDS-1000 gene gun. Reproduced from the BioRad PDS-1000 instruction manual.[14]

Figure 1.3: Schematic for the Bio-Rad Helios gene gun. Standoff distance shown is 2.8 cm. Reprinted with permission from O'Brien.[15]

Powder-based needleless injection

A novel drug delivery technique named powder needleless injection (PNI) uses a high-speed gas flow to accelerate particles to sufficiently high velocities to breach the surface of target tissues and penetrate to a certain depth in order to achieve a therapeutic response within the tissue.[16,17] The basic design of any powder-based needleless injection uses compressed gas as a carrier fluid, a compartment where the

Table 1.1: Comparison between commercial gene guns

	PDS-1000	**Helios Gene Gun**
System	*In vitro* and *ex vivo*	*In situ*
Operating Environment	Evacuated Chamber (vacuum)	Exposed system
Target Size	Large area (50 cm^2)	Small Area (2 cm^2)
Inlet Pressure	450–2200 psi	100–600 psi
Targets	Cell culture, embryos, algae, fungi	Animals, skin, organs, plants, leaves
Agents Delivered	450–2200 psi	100–600 psi
Particle Size	0.5–1.0 μm	0.5–3 μm gold particles
Penetration Depth	One layer of cells	Maximum 50 μm depth

powdered drug formulation is loaded and a nozzle to direct the particle flow towards the target. There are several different well researched devices that achieve the above criteria, and they are listed below (Table 1.2).[18] Key parameters in determining particle delivery into tissue are impact velocity, particle radius and particle density. Research has shown that smaller (0.5 to 3.7 μm), high density (> 10 g/cm^3) particles embed intracellularly.[19] Larger particles (25 to 100 μm) with lower densities (< 10 g/cm^3) tend to travel extracellularly. The most commonly studied particles for PNI are made of gold due to its high density, low toxicity and low chemical reactivity. Because PNI chooses small nano- or micro-sized particles, the microscopic holes caused from the delivery process are small enough to limit undesired effects such as pain, irritation and infection. Many drugs such as insulin need to be injected rather than orally administered due to their instability and the required bioavailability. PNI, as its name states, requires the drug to be in powdered form. Typically, to be suitable for use in PNI, a drug powder has high strength, hardness, and density because the powder is delivered through physical impact. As a result, polymeric-based and other low-density drugs (around 1 g/cm^3) have been avoided in previous research. Only Kendall[20] and Li[3] have done studies of delivery of such low-density particles and only into skin.

Table 1.2: Types of gene guns in literature

Type of gene gun	Materials of Particles	Diameter of Particles (µm)	References
Powder particle gun (PGG)	Tungsten	4	Klein (1987)[11]
Helium-driven apparatus (HDA)	Tungsten	3.9	Williams (1991)[21]
	Gold	1.3, 3–5	
Conical nozzle (CN)	Tungsten	4.7, 15.5, 26.1	Quinlan (2001)[22]
Converging-diverging nozzle (CDN)	Polystyrene	4.7	Kendall (2004)[20]
Pneumatic capillary gun (PCG)	Gold	0.47, 1.1, 1.27	Rinberg (2005)[23]
	Silicon	2–18	Zilony (2013)[24]
	Gold	1.6	
Light gas gun (LGG)	Stainless steel	25	Mitchell (2003)[19]
	Polystyrene	15.5, 25.2, 48, 99	
	Gold	3.03	Troung (2006)[25]
Contoured shock tube (CST)	Polystyrene	15, 48	Mitchell (2003)[19]
	Glass	46	
	Gold	2.7, 3.5	
	Polystyrene	39	Liu (2006)[26]
Helios gene gun	Gold	0.6, 1.0, 1.6	Uchida (2009)[27]
		1	O'Brien (2011)[28]
Biolistic PDS-1000 He system	Gold	0.6, 1.0, 1.6	Kuriakose (2012)[29]
BioWare low pressure gene gun	Gold	1	Yen (2013)[30]

High speed gas impingement

While use of PNI provides advantages such as being needle-free and the particles themselves are relatively pain-free, clinical trials on the skin have reported irritation and injury. These are primarily believed to be caused by the high speed gas that impinges on the skin for most PNI device designs. However, the overall effects due to exit gas pressure, outlet gas velocity, and the distance between the device and the target have yet to be fully studied.[31] In relation to this research, the focus on transient particles with high drug loading relatively low-density particles (ca. 1 g/cm^3), the particles will have relatively low inertia and will decelerate relatively quickly after moving from high velocity air to low velocity air near the tissue. Therefore, biolistic delivery of therapeutics motivates research on the interplay of inlet gas pressure, outlet gas velocity and distance between the device and the tissue. Uchida demonstrated that while DNA transfection was effective using a gene gun, cell damage occurred when the operating pressure of the device exceeded 200 psi (1482 kPa).[27] Xia also asserted that an inlet pressure of 200 psi (1482 kPa)[32] is the upper limit, coinciding with onset of tissue damage by a PNI application. Damage to the cells and tissue can be reduced by decreasing the particle size and/or decreasing the operating pressure of the devices. However, both of these choices decrease the penetration depth of the particles into the tissue. This remains a major drawback to PNI as a method of drug delivery.

1.3 Pneumatic capillary gun without gas impingement

A novel pneumatic gun for ballistic delivery of microparticles to tissue diverts gas flow to minimize damage to soft tissues (Figure 1.4).[23] Like other devices, it accelerates particles using a high-speed flow of gas in a capillary tube. The key difference lies near the outlet, where vacuum suction is applied through a concentric, larger diameter tube. This design diverts the flow of gas away from the outlet, thereby eliminating the damaging effects of the outlet gas on the tissue. The inertia of the particles carries them forward through an orifice where they travel through stagnant air between the outlet of the device and the tissue of interest. Vacuum is adjusted to null the velocity of air at the exit orifice (for example, a gauge pressure of –86 kPa was used with a gas inlet pressure of 120 kPa to deliver gold particles ranging from 0.47 to 1.27 m). A clinically relevant example that would benefit from the ability to deliver particles without high speed gas is the treatment of keratoconus, a disease of the eye that results in progressive thinning of the cornea.

1.4 Corneal anatomy and implications with biolistics

To understand keratoconus and its treatment, some background on the structure of the cornea is required (Figure 1.5). The importance of stable cornea shape is un-

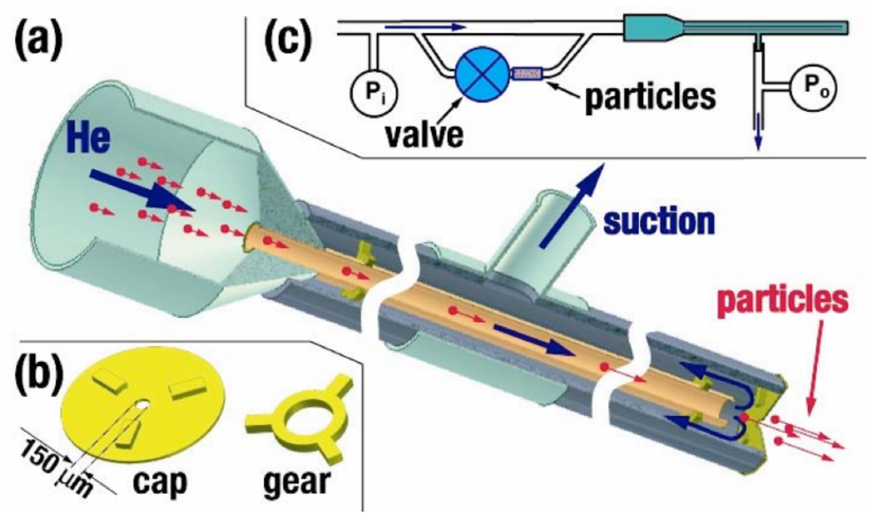

Figure 1.4: A schematic of the pneumatic capillary gun. The device shows a) the design and operation of the capillary gun, b) the micro-machined concentric “gear” and end cap, and c) the connection of the gun to pressurized helium and vacuum system. Reprinted with permission from Rinberg.[23]

derscored by the fact that it provides two-thirds of the focusing power of the human eye. Stable shape requires that the cornea be sufficiently strong that it does not undergo deformation due to the elevated intraocular pressure that maintains the relatively round shape of the eye. Of the five main layers of the cornea–epithelium, Bowman’s membrane, stroma, Descemet’s membrane, and endothelium—the stroma makes up about 90% of the cornea’s thickness and gives the tissue its strength.

The cornea is protected from pathogens and contaminants by the corneal epithelium, a highly organized multilayer of cells that is about 50 microns thick and covers the anterior surface of the cornea. Bowman’s membrane, located at the boundary between the epithelium and the corneal stroma, is an acellular layer that is about 8–12 microns thick in adult human corneas. The posterior surface of the cornea is covered by a single layer of cells, the corneal endothelium, that is responsible for pumping water out of the cornea to regulate its state of hydration and control transport of solutes and nutrients between the cornea and the aqueous humor. The thin, acellular layer that supports the endothelium and separates it from the stroma,

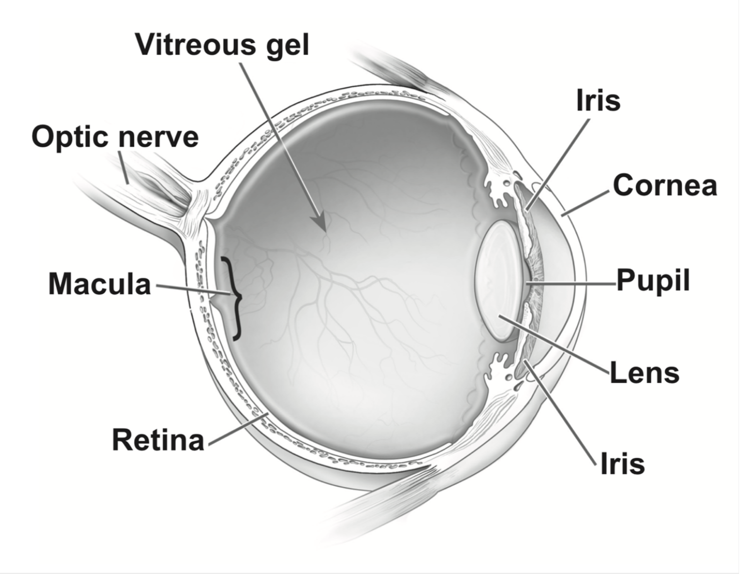

Figure 1.5: The anatomy of the eye. Reproduced from the National Eye Institute, National Institutes of Health.

Descemet's membrane, is typically 8–10 microns in adult human corneas. One of the inspirations for this doctoral research is to deliver drugs to the corneal stroma without disrupting the epithelium or endothelium which is essential for the healthy homeostasis of the cornea as a whole.

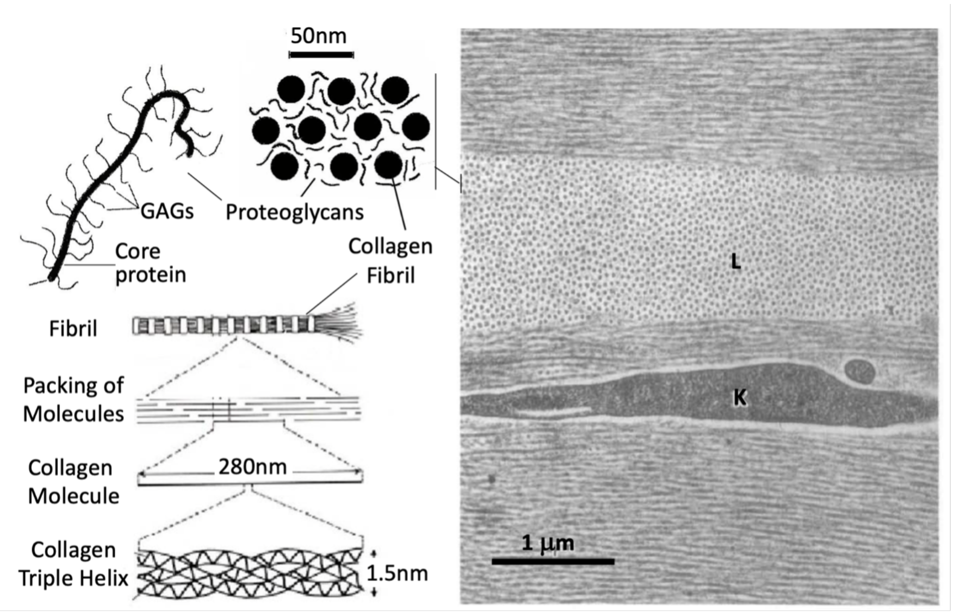

Figure 1.6: The structure of the corneal stroma. L = Lamellae, K = Keratocyte, G = Glycosoaminoglycans. Adapted from Oyster[33] and Komai and Ushiki.[34]

The stroma has a hierarchical organization from the nanometer scale of its constituent proteins to its overall thickness of hundreds of microns (Figure 1.6). The stroma's transparency results from the highly ordered arrangement of its collagen fibers and the uniformity in their diameters, ranging between 15 to 25 nm. The collagen fibers are organized into about 200 lamellae (labeled L in Figure 1.6). Each lamella has an anisotropic shape. In the plane of the cornea, lamellae are typically millimeters long and 10–100 μm wide; they are typically 2–3 microns thick. Within a given lamella, collagen fibers are uniformly oriented parallel to the long axis of the lamella. The lamellae are arranged into a superstructure of approximately orthogonal alternating layers that provide balanced strength in the plane of the tissue.

There are very few cells in the stroma. One type of these cells are keratocytes, which are sparsely distributed and regulate their intracellular protein concentration to provide a refractive index match to the surrounding lamellae. In a healthy homeostasis the keratocytes are relatively quiescent, performing gradual turnover and replacement of the constituents of the stroma. The proper composition, orientation, uniformity and superstructure of the stroma are essential to maintaining the clarity and shape of the cornea.

During the course of this research, we discovered that delivering particles to the epithelium offers complementary advantages relative to the delivery to the stroma. Thus, the layered structure of the anterior cornea — epithelium, basement membrane, and stroma — has profound implications for biolisitc delivery of therapeutics to treat ocular diseases.

1.5 Keratoconus and its treatment

Keratoconus is a corneal disease characterized by the thinning, protrusion, and scarring of the cornea. The cornea steepens as it thins paracentrally, resulting in the characteristic protrusion of the cornea leading initially to an increase in the focusing power (i.e., myopia or nearsightedness) and later to severe higher order aberrations and visual impairment that cannot be corrected by spectacles or even with special hard contact lenses used to deform the cornea into the correct shape. Ultimately, when the refractive correction loses its efficacy, keratoplasty (corneal transplant), is required. Approximately 20% of all keratoconus patients eventually require a corneal transplant, which translates to about 1 in 10,000 Americans for a total of 30,000 corneal transplants per year for keratoconus alone. The need for a treatment that halts the progression of keratoconus at a stage that is still amenable to refractive correction motivated the development of corneal crosslinking therapies.

Wollensak and Spoerl pioneered a way to increase the strength of the cornea by using ultraviolet light to activate riboflavin to create protein-protein cross-links within the stroma.[35,36] By using light activated crosslinking, the treatment provides spatial and temporal control over the application of the crosslinks. The treatment involves the removal of the central 7 mm diameter of the corneal epithelium and then applying drops of a 0.1% riboflavin solution every 5 minutes for 30 minutes prior to ultraviolet (UV) exposure and every 5 minutes during a 30-minute period while the cornea is exposed to UV-A light. In typical cases, the epithelium regenerates within 7–10 days. The key differences from the previously listed treatments is that riboflavin/UVA crosslinking can actually halt the progression of keratoconus as opposed to merely correcting refractive errors caused by the disease. However, there are several drawbacks to this treatment. The first is the requirement to remove the corneal epithelium. Because the epithelium's function is to protect the eye and prevent toxins and pathogens from entering the tissue, it also blocks the delivery of riboflavin molecules into the stroma. As a result, the epithelium is typically removed to ensure delivery of a proper dosage of drug. In addition, the epithelium is home to 325,000 nerve endings, which when removed, risks other problems including losing sensation in detecting foreign particles on the surface of the eye and triggering the blink reflex. Secondly, the UV light in combination with riboflavin has toxic effects on the keratocytes present within the corneal stroma. (Even if the epithelium is left intact early the procedure, it is killed during the UV irradiation.) Removal of the epithelium and death of keratocytes elicit an inflammatory response that causes the cornea to swell and become hazy. In most patients, the cornea recovers within 6 months; however, many patients have permanent haze in their cornea after the procedure.

To address the toxicity of the riboflavin/UVA crosslinking treatment, Joyce Huynh[37] and Matthew Mattson[38] in the Kornfield lab developed a treatment to mechanically strengthen the cornea using visible light activation of Eosin Y (EY). They demonstrated that the Eosin Y/visible light treatment produced similar crosslinking effects to riboflavin/UVA, and dramatically reduced the toxicity to the keratocytes in the corneal stroma. The treatment itself would not be toxic to the epithelium, offering the potential to maintain the protective function of the epithelium and avoid disrupting the nerves of the epithelium.

Unfortunately, it took several hours for an adequate amount of EY to penetrate the corneal epithelium. Early in my thesis work, I explored diverse adjuvants in an effort to reduce the time required to deliver EY to the cornea. Although adjuvants demonstrated potential in enhancing drug delivery across the corneal epithelium, their effectiveness seemed to hinge on destroying epithelial cells. This approach, however, entails the typical drawback of necessitating several days for the epithelium to successfully regrow and heal. Thus, despite these efforts, the Eosin Y/visible light treatment would still involve the removal of the epithelium.

The risks involved with a corneal debridement include pain, risk of infection, decreased vision, and corneal hazing. Moreover, anomalous swelling has been documented in the stroma following epithelial debridement. When Bowman's membrane is disturbed, scattering centers could form in the stroma, with increased light scattering, matrix disorder, collagen diameter, along with the appearance of larger than normal proteoglycans.[39]

1.6 Application of therapeutic particle delivery to treat keratoconus

Our group has previously examined the opportunity to use therapeutic particle delivery to introduce Eosin Y into the cornea without debridement. However, prior results from the pneumatic capillary gun[23] designed by Professor Alex Groisman from UCSD showed the inability to deliver low-density particles ($\sim$ 1 g/cm^3) into the corneal stroma for use in keratoconus treatment.[40] This research focuses on altering the Groisman design of the pneumatic capillary gun to better accelerate and deliver therapeutic particles without exit gas damage into the stroma. Furthermore, the cornea provides the perfect tissue to study this new technology because it is transparent, unlike many other tissues within the human body. Transparent tissues allow for the visualization of the drug particles that enter the tissue, as well as the biological responses. Some effects that will be monitored include scar formation, epithelium closure, drug uptake, cell migration and damage, and inflammatory responses within an *ex vivo* model. In turn, if proven effective, therapeutic drug delivery can then be applied to opaque tissues, such as the skin and liver.

1.7 Outline of the thesis

Following the work of our group, Laccetti (Caltech ChE PhD 2020)[40] has shown promising results in delivering high density particles ($>$ 1 g/cm^3) using the BioRad PDS-1000 Helium System into corneal tissue. However, inherent weaknesses of the BioRad PDS-1000 device exist — that is, it is not clinically able to deliver drugs into patients. The objective therefore is, as described in Chapter 2, to design a device building upon Groisman's pneumatic capillary gun (with no exit gas velocity) that allows us to deliver drug particles into the corneal stroma. The particles this device can deliver are not only low density, clinically relevant drug particles, such as Eosin Y, but also higher density, deeper penetrating particles such as those previously examined by our group. For our work to be clinically relevant, we require the particles to be delivered into the stroma with minimal tissue damage. In Chapter 3, we examine the short-term physical effects of particle delivery, including whether the corneal surface maintains its visual acuity and the epithelial barrier function recovers quickly. In **??**, the microparticles delivered into the cornea are tracked to quantify whether they are clinically significant, spatially controlled, and stable over a period of time.

References

[1] W. H. Organization. *Making all injections safe*. 2015.

[2] S. Mitragotri. “Immunization without needles”. In: *Nat Rev Immunol* 5.12 (Dec. 2005), pp. 905–16. ISSN: 1474-1733 (Print) 1474-1733 (Linking). DOI: 10.1038/nri1728.

[3] C. Y. Li et al. “Needle-free injection of insulin powder: delivery efficiency and skin irritation assessment”. English. In: *Journal of Zhejiang University-Science B* 15.10 (Oct. 2014), pp. 888–899. ISSN: 1673-1581. DOI: 10.1631/jzus.B1400065.

[4] S. Mitragotri. “Current status and future prospects of needle-free liquid jet injectors”. In: *Nature Reviews Drug Discovery* 5.7 (July 2006), pp. 543–548. ISSN: 1474-1784. DOI: 10.1038/nrd2076. URL: https://doi.org/10.1038/nrd2076.

[5] M. Lombard. “Quartz-tipped arrows older than 60 ka: further use-trace evidence from Sibudu, KwaZulu-Natal, South Africa”. English. In: *Journal of Archaeological Science* 38.8 (Aug. 2011), pp. 1918–1930. ISSN: 0305-4403. DOI: 10.1016/j.jas.2011.04.001.

[6] Y. Sahle et al. “Earliest Stone-Tipped Projectiles from the Ethiopian Rift to Date > 279,000 Years Ago (vol 8, e78092, 2013)”. English. In: *PLoS One* 10.4 (Apr. 2015). ISSN: 1932-6203. DOI: ARTNe012606410.1371/journal.pone.0126064.

[7] E. Mcewen, R. L. Miller, and C. A. Bergman. “Early Bow Design and Construction”. English. In: *Scientific American* 264.6 (June 1991), pp. 76–82. ISSN: 0036-8733.

[8] W. Y. Carman. *A history of firearms: from earliest times to 1914*. Vol. 7. Routledge, 2015. ISBN: 1-317-41116-1.

[9] M. Valleriani. *Metallurgy, Ballistics and Epistemic Instruments: The Nova scientia of Nicolò Tartaglia*. epubli GmbH, 2013. ISBN: 3-8442-5258-4.

[10] J. C. Sanford. “The development of the biolistic process”. English. In: *In Vitro Cellular & Developmental Biology-Plant* 36.5 (Oct. 2000), pp. 303–308. ISSN: 1054-5476. DOI: DOI10.1007/s11627-000-0056-9.

[11] T. M. Klein et al. “High-Velocity Microprojectiles for Delivering Nucleic-Acids into Living Cells”. English. In: *Nature* 327.6117 (May 1987), pp. 70–73. ISSN: 0028-0836. DOI: DOI10.1038/327070a0.

[12] J. C. Sanford et al. “An improved, helium-driven biolistic device”. In: *Technique* 3.1 (1991), pp. 3–16.

[13] J. R. Kikkert. “The Biolistic(R) Pds-1000 He Device”. English. In: *Plant Cell Tissue and Organ Culture* 33.3 (June 1993), pp. 221–226. ISSN: 0167-6857. DOI: Doi10.1007/Bf02319005.

[14] *PDS-1000/He Biolisitic Particle Delivery System*. Version B. Available at https://www.bio-rad.com/webroot/web/pdf/lsr/literature/10000070900.pdf. Bio-Rad Laboratories, Inc. Hercules, CA, USA.

[15] J. A. O'Brien and S. C. Lummis. "Biolistic transfection of neuronal cultures using a hand-held gene gun". In: *Nature protocols* 1.2 (2006), pp. 977–981.

[16] A. Arora, M. R. Prausnitz, and S. Mitragotri. "Micro-scale devices for transdermal drug delivery". In: *Int J Pharm* 364.2 (Dec. 2008), pp. 227–36. ISSN: 0378-5173 (Print) 0378-5173 (Linking). DOI: 10.1016/j.ijpharm.2008.08.032.

[17] T. R. Kale and M. Momin. "Needle free injection technology-An overview". In: *Innovations in pharmacy* 5.1 (2014), p. 10. ISSN: 2155-0417.

[18] D. W. Zhang, D. B. Das, and C. D. Rielly. "Potential of microneedle-assisted micro-particle delivery by gene guns: a review". English. In: *Drug Deliv* 21.8 (Dec. 2014), pp. 571–587. ISSN: 1071-7544. DOI: 10.3109/10717544.2013.864345.

[19] T. J. Mitchell, M. A. Kendall, and B. J. Bellhouse. "A ballistic study of micro-particle penetration to the oral mucosa". In: *International journal of impact engineering* 28.6 (2003), pp. 581–599. ISSN: 0734-743X.

[20] M. Kendall, T. Mitchell, and P. Wrighton-Smith. "Intradermal ballistic delivery of micro-particles into excised human skin for pharmaceutical applications". In: *J Biomech* 37.11 (Nov. 2004), pp. 1733–41. ISSN: 0021-9290 (Print) 0021-9290 (Linking). DOI: 10.1016/j.jbiomech.2004.01.032.

[21] R. S. Williams et al. "Introduction of foreign genes into tissues of living mice by DNA-coated microprojectiles." In: *Proceedings of the National Academy of Sciences* 88.7 (Apr. 1991), p. 2726. DOI: 10.1073/pnas.88.7.2726. URL: http://www.pnas.org/content/88/7/2726.abstract.

[22] N. J. Quinlan et al. "Investigations of gas and particle dynamics in first generation needle-free drug delivery devices". English. In: *Shock Waves* 10.6 (Jan. 2001), pp. 395–404. ISSN: 0938-1287. DOI: Doi10.1007/Pl00004052.

[23] D. Rinberg, C. Simonnet, and A. Groisman. "Pneumatic capillary gun for ballistic delivery of microparticles". In: *Applied Physics Letters* 87.1 (2005), p. 014103. ISSN: 0003-6951.

[24] N. Zilony et al. "Bombarding cancer: biolistic delivery of therapeutics using porous Si carriers". In: *Scientific reports* 3 (2013). ISBN: 2045-2322 Publisher: Nature Publishing Group, p. 2499.

[25] N. K. Truong, Y. Liu, and M. A. F. Kendall. "Gas and particle dynamics of a contoured shock tube for pre-clinical microparticle drug delivery". English. In: *Shock Waves* 15.3-4 (July 2006), pp. 149–164. ISSN: 0938-1287. DOI: 10.1007/s00193-006-0034-1.

[26] Y. Liu and M. A. F. Kendall. “Numerical analysis of gas and micro-particle interactions in a hand-held shock-tube device”. English. In: *Biomedical Microdevices* 8.4 (Dec. 2006), pp. 341–351. ISSN: 1387-2176. DOI: 10.1007/s10544-006-9596-z.

[27] M. Uchida et al. “Transfection by particle bombardment: delivery of plasmid DNA into mammalian cells using gene gun”. In: *Biochim Biophys Acta* 1790.8 (Aug. 2009), pp. 754–64. ISSN: 0006-3002 (Print) 0006-3002 (Linking). DOI: 10.1016/j.bbagen.2009.05.013.

[28] J. A. O’Brien et al. “Modifications to the hand-held Gene Gun: improvements for in vitro biolistic transfection of organotypic neuronal tissue”. In: *J Neurosci Methods* 112.1 (Nov. 2001), pp. 57–64. ISSN: 0165-0270 (Print) 0165-0270 (Linking).

[29] B. Kuriakose, E. Du Toit, and A. Jordaan. “Transient gene expression assays in rose tissues using a Bio-Rad Helios® hand-held gene gun”. en. In: *South African Journal of Botany* 78 (Jan. 2012), pp. 307–311. ISSN: 02546299. DOI: 10.1016/j.sajb.2011.06.002. URL: https://linkinghub.elsevier.com/retrieve/pii/S0254629911000925 (visited on 11/12/2020).

[30] M.-C. Yen and M.-D. Lai. “Biolistic DNA delivery to mice with the low pressure gene gun”. In: *Biolistic DNA Delivery*. Springer, 2013, pp. 169–174.

[31] D. F. Sarphie et al. “Bioavailability following transdermal powdered delivery (TPD) of radiolabeled inulin to hairless guinea pigs”. In: *Journal of Controlled Release* 47.1 (1997), pp. 61–69. ISSN: 0168-3659. DOI: https://doi.org/10.1016/S0168-3659(96)01616-1. URL: http://www.sciencedirect.com/science/article/pii/S0168365996016161.

[32] J. X. Xia et al. “Evaluation of biolistic gene transfer methods in vivo using non-invasive bioluminescent imaging techniques”. English. In: *Bmc Biotechnology* 11 (June 2011). ISSN: 1472-6750. DOI: Artn6210.1186/1472-6750-11-62.

[33] C. W. Oyster. “The human eye: structure and function”. In: *(No Title)* (1999).

[34] Y. Komai and T. Ushiki. “The three-dimensional organization of collagen fibrils in the human cornea and sclera.” In: *Investigative ophthalmology & visual science* 32.8 (1991), pp. 2244–2258.

[35] G. Wollensak, E. Spoerl, and T. Seiler. “Riboflavin/ultraviolet-A–induced collagen crosslinking for the treatment of keratoconus”. In: *American journal of ophthalmology* 135.5 (2003), pp. 620–627.

[36] G. Wollensak, E. Spoerl, and T. Seiler. “Stress-strain measurements of human and porcine corneas after riboflavin–ultraviolet-A-induced cross-linking”. In: *Journal of Cataract & Refractive Surgery* 29.9 (2003), pp. 1780–1785.

[37] J. Huynh. “Factors governing photodynamic cross-linking of ocular coat”. PhD thesis. California Institute of Technology, 2011.

[38] M. S. Mattson. “Understanding and Treating Eye Diseases: Mechanical Characterization and Photochemical Modification of the Cornea and Sclera”. PhD thesis. California Institute of Technology, 2008.

[39] C. Boote et al. “Quantitative Assessment of Ultrastructure and Light Scatter in Mouse Corneal Debridement Wounds”. In: *Investigative Ophthalmology & Visual Science* 53.6 (May 2012), pp. 2786–2795. ISSN: 1552-5783. DOI: `10.1167/iovs.11-9305`. URL: `https://doi.org/10.1167/iovs.11-9305` (visited on 01/26/2021).

[40] B. J. Laccetti. “Therapeutic Microparticles and Biolistic Drug-Delivery to the Cornea”. PhD thesis. California Institute of Technology, 2020.

Chapter 2

PHYSICS OF BALLISTIC PARTICLE DELIVERY

2.1 Introduction

The cornea presents special requirements and offers unique opportunities for drug delivery. As an avascular tissue, the cornea cannot be addressed by recent advances in drug delivery through the gastrointestinal, pulmonary, or vascular system. The exposed anterior surface of the cornea provides a route to deliver drugs, usually using drops or gels. In contrast to other alternatives (Table 2.1, biolistic delivery could be developed to meet the following requirements relevant for drug delivery to the cornea:

1. Vehicle delivery must occur within clinical time constraints (this chapter),
2. Delivery process must allow for rapid recovery of epithelial barrier function (Chapter 3),
3. Drug dose must be quantitatively controlled and clinically significant (**??**).

The opportunities include improved treatment of corneal diseases and sustained release of drugs placed in the corneal stroma for treatment of prolonged or chronic ocular conditions. However, as explained in Chapter 1, significant progress is required beyond inertial delivery of therapeutic agents into the skin.

Prior literature on particle delivery to the cornea is scant, consisting of a few articles and a book chapter.[1,2] Only three particle sizes (0.6, 1, 1.6 µm diameter) of a single composition (gold) were examined that all similarly resulted in a penetration depth of approximately 50 µm in the epithelium of mice or rats.

Little information is provided regarding the effects of particle delivery on the corneal surface or epithelial integrity. Our interest in drug delivery motivates research on particles of larger size than the 1.6 µm diameter and lower density than 19.3 g/cm^3 reported previously. For example, corneal crosslinking therapy requires a dose of drug that would require $\sim 2 \times 10^5$ particles of 2 µm diameter per square millimeter of cornea — if composed of pure drug ([REDACTED]). The low density of drugs relative to gold would decrease the ability of the particles to penetrate into the tissue. An initial study of corneal biolistic delivery as a function of particle size and density by Laccetti and Kornfield guides us to focus on particles of diameters ranging from 5 to 30 µm and density from 1.2 to 19.3 g/cm^3, as discussed in greater detail below. We were unable to find any other studies on the use of biolistics to deliver microparticles greater than 5 µm diameter into the cornea or other ocular tissues.

This work is motivated by corneal ectasias (e.g., keratoconus) that cause visual impairment in 1 out of every 2000 Americans due to progressive, irregular changes in the shape of the cornea that are difficult or impossible to correct using spectacles or contact lenses. The current standard of care for corneal ectasias is therapeutic corneal cross-linking, a surgical intervention. In the US, the approved procedure requires epithelial scraping, riboflavin drops, and prolonged exposure to UVA. Stripping the epithelium is associated with severe pain, stromal haze, and infections. As described in the preceding chapter, Matthew Mattson (Caltech APh PhD 2008) and Joyce Huynh (Caltech ChE PhD 2011) in the Kornfield group showed that Eosin Y can be used to strengthen the cornea using green light with very low toxicity, in contrast to the toxicity caused by the current clinical practice of using riboflavin with UV light. *Ex vivo* experiments on enucleated rabbit eyes showed that if the epithelium were not compromised during EY delivery, the epithelium would retain its barrier function after irradiation with green light. This opens the possibility of a non-surgical procedure — if a quantitatively controlled dose of drug can be delivered *through* the corneal epithelium in a clinically acceptable time.

Prior studies have been done to avoid the debridement step, such as employing injections, implementing pre-procedure eye drop regimens, having medical staff administer eye drops, and incorporating adjuvants into the drug-containing eye drops, but no approach has achieved US FDA clinical approval. Our own prior research examined many adjuvants (e.g., EDTA, VEGF, EGF, and combinations of these) with the goal of achieving rapid (ca. 5 min) delivery of an adequate, consistent dose of drugs through the intact corneal epithelium, but the observed increase in drug delivery proved to be marginal (approx. 20%), consistent with prior literature. Thus, there is an unmet need for fast (< 5 min), quantitative (specific dose), safe (preserving the epithelium) delivery of drug to the cornea to treat anterior segment diseases.

Significant progress in the design of ballistic delivery devices has been achieved since the introduction of "gene guns" in the 1980s to deliver DNA on metallic nanoparticles to cells at or very near the surface of biological specimens.[5] The most widely used apparatus, the Bio-Rad PDS-1000 (Figure 1.2), requires the biological specimen to be placed in a vacuum chamber at –15 psi (–100 kPa or –1 atm). DNA-coated nanoparticles are loaded onto a rupture disc rated to the desired rupture pressure; helium pressure is increased until the disc ruptures (450–2200 psi, 3.1–15.2 MPa) and propels the gene carriers into cells—usually plant cells. Due to the necessity of a vacuum enclosure, the PDS-1000 is not suitable for animal studies or clinical applications.

A handheld adaptation was subsequently developed for use at ambient pressure (Figure 1.3).[6] DNA-coated submicron metal particles are loaded on the inner surface of a cartridge; high pressure helium (100–600 psi, 0.7–4.1 MPa) is used as the

Table 2.1: Evaluation of alternative corneal drug delivery mechanisms

	Debridement	**Adjuvants**	**Biolistics**	**Groisman device**	**This thesis**
Drug delivery mechanism	Surgical removal of the corneal epithelium allows drug to diffuse into the corneal stroma.	Adjuvants enhance the efficacy of topical drops by temporarily increasing the permeability of the corneal epithelium.	Delivers genes intracellularly using metal carrier nanoparticles (tungsten, gold) that are not readily absorbed by the body.	Literature precedent for delivery of particles having density similar to 100% drug particle ($\sim$ 1 g/cm^3).	Particles with varying densities delivered into cornea without exit gas damage.
Relevant timescale	The patient's eye is retracted (lid held open) for 5 minutes.	Hours are needed (even with adjuvants) to deliver a sufficient dose.	A single or multiple delivery of ballistic particles can be accomplished within seconds, followed by dissolution and diffusion over a few to several minutes while the patient rests with eyes closed.		
Intact epithelium	The gel is placed on top of the cornea for diffusion into the stroma.	Adjuvants are able to allow drugs to pass through without permanently modifying the epithelium.	Tissue damage from high exit gas velocity.[3,4]	Diverts exit gas so velocity that tissue is undamaged.	Divert exit gas, Preliminary results suggest elasticity rapidly restores epithelial continuity.
Quantity of drug	Sufficient drug* is transferred from gel placed on the debrided cornea in a time as short as 5 minutes.	Adjuvants only increase the transport rate through intact epithelium by 20%; relevant drug dose* requires hours (above).	Approximately 10^{15} drug particles of 1 nm per mm^2 are needed for a clinically relevant dose.*	Approximately 60 drug particles of about diameter 30 μm per mm^2 of cornea can deliver a clinically relevant dose.*	

*Calculations based on the amount of photosensitizer Eosin Y required for corneal crosslinking

carrier gas to entrain and accelerate the particles (Figure 1.2). However, eliminating the vacuum chamber does not enable the use of the Bio-Rad device on mammalian cells or animals because the gas that carries the nanoparticles also injuring mammalian cells and animal tissues[3,7].

More than twenty years passed before a method was found to deliver particles to soft-tissue without injury due to impingement of high velocity gas — a device invented by Prof. Alex Groisman at UCSD that redirects the high-speed carrier gas away from the outlet of the ballistic particle delivery device (Figure 1.4).[8,9] In the present study, a two-stage gas diversion unit (GDU) that, diverts most of the gas using a disc with a small orifice ("first orifice disc," OrD-1) approximately 600–900 μm from the end of the inner capillary tube (ICT), to redirect carrier gas radially out-

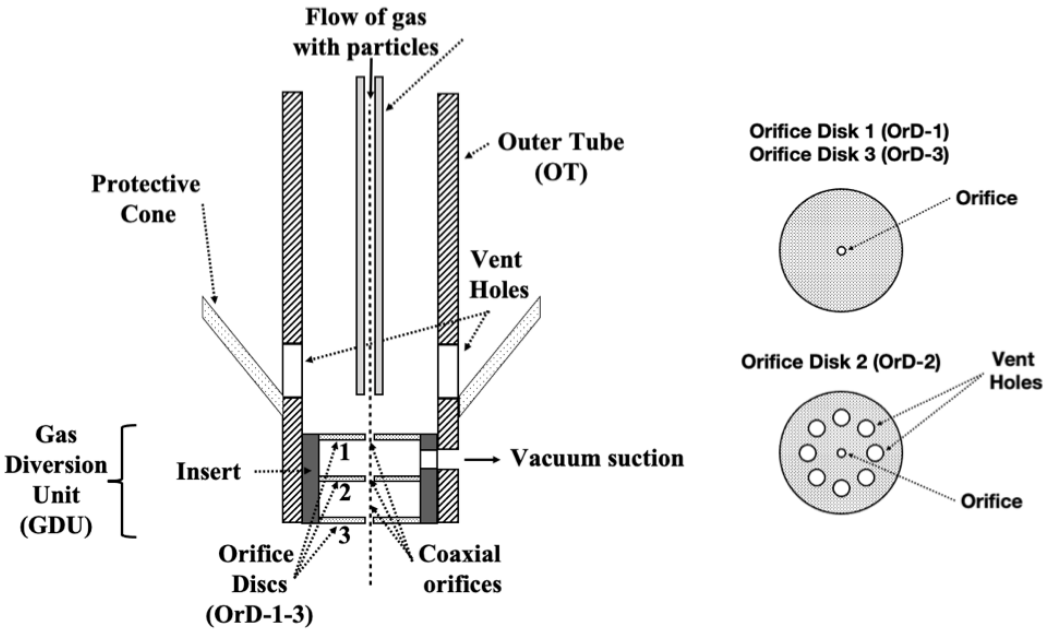

Figure 2.1: Detailed schematic of an improved particle delivery device.

ward through large vent holes in the outer tube (OT) (Figure 2.1), allowing most of the particles to pass through the orifice due to their inertia and an imposed vacuum on the opposite side of OrD-1. The second stage of gas diversion occurs between OrD-1 and OrD-3 by application of vacuum, which brings the carrier gas pressure down to ambient, such that negligible gas leaves the device through the orifice in OrD-3. Of particular importance to the present research, Groisman was able to deliver particles of the same density as the target tissue, indicating it is feasible to deliver particles that consist almost entirely of drug and bioresorbable components that dissolve completely — a key requirement for drug delivery to the cornea.[10]

The remainder of this chapter examines the physics of delivering particles having density close to that of neat drug and comparison with higher densities: the analysis culminates with the physics of penetration of particles in gel (Regime 3, Figure 2.2), which dictates the required impact velocity, $u_{p,i}$, and, allows for deceleration as the particle moves through stagnant air (Regime 2, Figure 2.2), which dictates the velocity the particles must have when exiting the device, $u_{p,e}$. The analysis begins

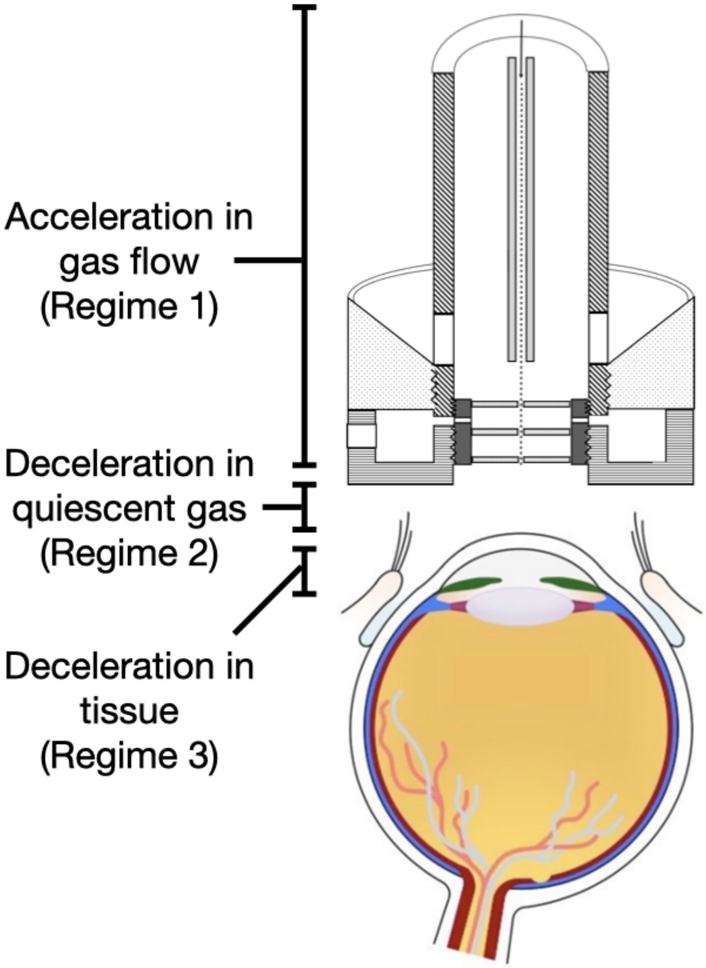

Figure 2.2: Analysis of particle velocity is divided into three regimes: 1. The acceleration of the gas as it moves through the device undergoing approximately adiabatic expansion and the acceleration of drug particles introduced into the gas flow; 2. the particles leave the device and decelerate due to drag forces acting on them by the surrounding stagnant air; and 3. drug particles penetrate the tissue and eventually come to rest.

with the acceleration of the particles in the device (Regime 1, Figure 2.2), which suggest device improvements that I investigate in this thesis. In the course of the analysis, I highlight areas in which literature knowledge is lacking, motivating subsequent chapters of this thesis.

2.2 Acceleration of the gas (Regime 1)

To determine the particle velocity, we first estimate the gas velocity, u_g, as a function of axial position in the inner tube. We approximate the flow as steady, one-dimensional and adiabatic (there is no perceptible heat exchange with the environment) and approximate the gas as ideal, solving for the gas velocity, pressure, and temperature as a function of axial position following Saad and Levenspiel.[11]

Using the ideal gas law, mass balance, momentum balance, energy balance, definition of Mach number ($M = u_g/c$, where u_g is the gas velocity and c is the speed of sound in the gas) and the second law of thermodynamics leads to the following implicit function for the gas Mach number at axial position z, denoted M_2, as a function of the inlet Mach number, M_1, the hydraulic diameter of the duct, D_H, the heat capacity ratio $\gamma = C_p/C_v$, and the friction factor, $\bar{f}$, averaged over the length of the tube L.

$$\frac{4\bar{f}z}{D_H} = \frac{1}{\gamma}\left(\frac{1}{M_1^2} - \frac{1}{M_2^2}\right) + \frac{\gamma+1}{2\gamma}\ln\left(\frac{M_1^2}{M_2^2}\cdot\frac{1+\frac{\gamma-1}{2}M_2^2}{1+\frac{\gamma-1}{2}M_1^2}\right) \tag{2.1}$$

The heat capacity ratio used is appropriate for monatomic gases (here, helium), $\gamma = 1.67$. We do not intend to exceed Mach 1, so we first use Equation 2.1 to obtain an expression for L^*, the axial distance at which the gas would reach Mach 1 (Equation 2.2), by replacing M_2 by 1 and introducing a specific value of M_1:

$$\frac{4\bar{f}L^*}{D_H} = \frac{1-M_1^2}{\gamma M_1^2} + \frac{\gamma+1}{2\gamma}\ln\left(\frac{(\gamma+1)M_1^2}{2\left(1+\frac{\gamma-1}{2}M_1^2\right)}\right). \tag{2.2}$$

In a scenario where we have two inlet Mach numbers, M_1 and M_2, we can determine the L^* for each inlet Mach number — $(L^*)_{M_1}$ corresponding to Mach M_1 and $(L^*)_{M_2}$ corresponding to Mach M_2. The difference between the two values, $(L^*)_{M_1}$ and $(L^*)_{M_2}$, represents the length of duct that is between the gas where their Mach numbers are M_1 and M_2.

$$L_{1-2} = L_a = (L^*)_{M_1} - (L^*)_{M_2} \tag{2.3}$$

This relationship generalizes to describe the increase in the gas velocity from the inlet, M_1, to any arbitrary position between the inlet and exit (L < L^*) for constant $\bar{f}$ and D_H. If we replace M_1 in the right hand side of Equation 2.2 by M_2, where $1 > M_2 > M_1$, we can evaluate the corresponding distance upstream of the point at which the flow would reach Mach 1 if the inlet velocity were M_2, $(L^*)_{M_2}$ and use the difference between L^* and $(L^*)_{M_2}$ to evaluate the axial position at which gas velocity reaches M_2

$$\frac{4\bar{f}L_a}{D_H} = \left(\frac{4\bar{f}L^*}{D_H}\right)_{M_1} - \left(\frac{4\bar{f}L^*}{D_H}\right)_{M_2}. \tag{2.4}$$

The acceleration of the gas given its position along the tube is shown in Figure 2.3a. Similarly, the pressure at which the flow would reach Mach 1, p^*, can be calculated for a specific inlet pressure p_1, using

$$\frac{p_1}{p^*} = \frac{1}{M_1}\sqrt{\frac{\gamma+1}{2+(\gamma-1)M_1^2}}. \tag{2.5}$$

As with Equation 2.2, we can replace M_1 in the right-hand side of Equation 2.5 by arbitrary $M_a > M_1$ to determine the pressure at the corresponding axial position (Figure 2.3b).

2.3 Acceleration of the particles (Regime 1)

To estimate the velocity of a drug particle, we consider its acceleration once it is entrained in the gas that is itself accelerating (Figure 2.3a, $z_p \approx 120$ mm, $p_i \approx 200$ kPa, T $\approx$ 225K, ρ_{He}= 0.138 $\frac{kg}{m^3}$, $\mu_{He} = 2 \times 10^{-5} \frac{kg}{m \cdot s}$). Three types of particles are considered based on their similarities with existing therapeutics (Table 2.2). Based on the expectation of turbulent flow (Reynolds number based on the diameter of the inner capillary d_{ICT}=1.8 mm, $Re_{ICT} = \frac{\rho_{He} U \ d_{ICT}}{\mu_{He}}$, increases from 1.1×10^4 at the inlet to 1.6×10^4 where the gas velocity reaches 800 m/s), we neglect radial dependence of the velocity profile (for a drug particle with diameter, $d_p = 10 - 30$ µm $\ll d_{ICT}$, the time-smoothed flow is approximately uniform). The axial position at which particles are introduced is taken to be zero, $z_p = 0$ at $t_1 = 0$ of Regime 1 (subscript i indicates the i-th Regime and time is "reset to zero," i.e., $t_i = 0$, when the particle enters the i-th Regime), and the axial velocity of particles at that point is negligible, $u_p = 0$ at $t_1 = 0$. Consequently, the difference between the particle and the gas velocities is large when the particles are first entrained; acceleration of the particles brings their velocity closer to that of the carrier gas, so both the particle Reynolds number and the force on the particles decrease over the first 60 mm of the inner capillary tube.

As a particle moves through the inner capillary, it is affected by the local conditions at its current position $z_p(t)$. Consequently, it is exposed to changing temperature, pressure, gas velocity and gas properties. In an example relevant to biolistic delivery, the temperature, pressure and velocity of helium change from 298 K, 800 kPa and 200 m/s at $z_p = 0$, to approximately 225 K, 200 kPa and 800 m/s at z_p =120 mm

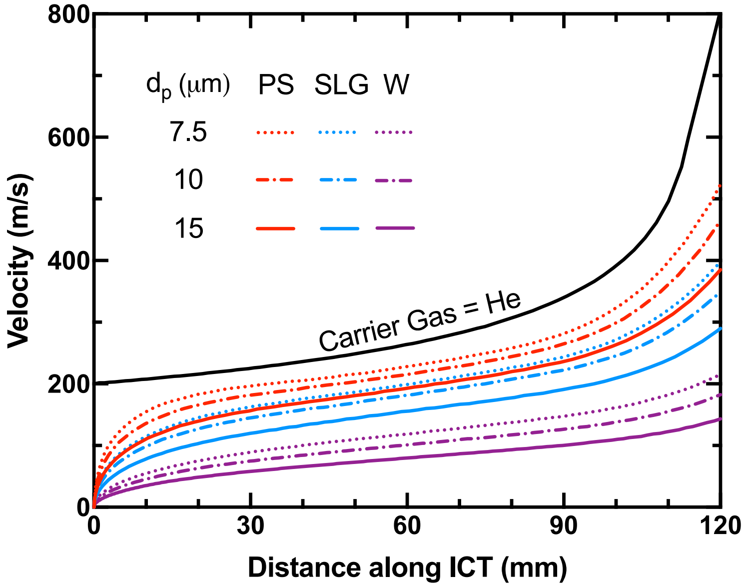

(a) Gas and particle velocity in ICT

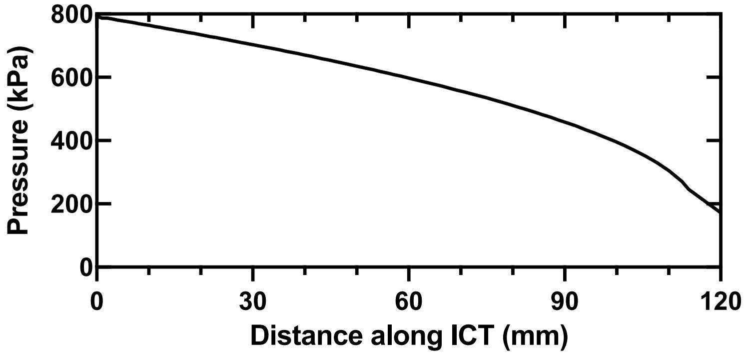

(b) Pressure profile inside the ICT

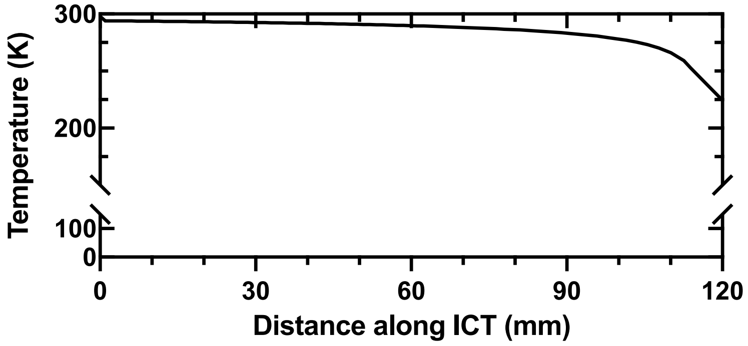

(c) Temperature profile inside the ICT

Figure 2.3: The a) velocity, b) pressure and c) temperature profiles calculated for an ideal gas (to approximate helium) expanding adiabatically as it flows through the inner capillary tube (D_H = 1.8mm, $\bar{f}$ = 0.002 for stainless steel), initially at 7.6 atm (100 psi gauge, 115 psi) and 298 K. The gas velocity, pressure and temperature profiles are determined from Equation 2.1 and Equation 2.5. PS = Polystyrene, ρ_p = 1.05 g/cm^3, SLG = Soda Lime Glass, ρ_p = 2.85 g/cm^3, W = Tungsten, ρ_p = 19.3 g/cm^3

Table 2.2: Types of microparticles modeled

Material	Density	Density
Polystyrene	1.05 g/cm^3	Density comparable to Eosin Y
Soda lime glass	2.85 g/cm^3	Density comparable to copper minerals
Tungsten	19.3 g/cm^3	Density comparable to gold microparticles

(Figure 2.3a). Helium's viscosity is a weak function of pressure and its temperature dependence approximately follows the kinetic theory for gases: $\mu \sim \rho\bar{u}\lambda$, where density and mean free path are inversely proportional to each other, leaving $\mu \sim \bar{u} \sim \sqrt{kT/m}$.

We model the acceleration of drug particles by approximating the flow as uniform with carrier gas axial velocity, $u(z)$. For the particle sizes and flow conditions of interest, the particle Reynolds number $Re_p < 180$, allowing the drag to be computed using a finite-Re_p correction to the Stokes drag (Equation 2.7 rather than Equation 2.6):

$$F_d = 3\pi\eta(u - u_p)d_p \text{ for creeping flow } (Re_p < 1)\text{, or} \tag{2.6}$$

$$F_d = 3\pi\eta(u - u_p)d_p[1 + 0.15Re_p^{0.687}] \quad \text{for } (1 < Re_p < 1000). \tag{2.7}$$

Newton's second law (Equation 2.8) relates the force exerted by the fluid on the particle to the particle's acceleration,

$$F = m\frac{du_p}{dt}, \tag{2.8}$$

where m is particle mass,

$$m = \frac{1}{6}\pi d_p^3 \rho_p. \tag{2.9}$$

If the particle experienced Stokes flow in a fluid of constant viscosity, the force acting to accelerate it would simply be proportional to the difference between the gas and particle velocities, $(u - u_p)$, causing that difference to decrease exponentially with time;[12] and it is useful to write the acceleration of the particle in terms of the resulting hydrodynamic relaxation time, τ_v,

$$\frac{du_p}{dt} = \frac{[u - u_p]}{\tau_v}. \tag{2.10}$$

In Regime 1, $\tau_{v,1}$, (Equation 2.11 and, with inertial correction, Equation 2.12) varies with the instantaneous viscosity of the carrier gas, μ_{cg}, at the local temperature and pressure at the particle's current position, z_p, using the appropriate drag expression above, either

$$\tau_{v,1} = \left(\frac{d_p^2 \rho_p}{18\mu}\right) \quad \text{for} \quad (Re_p < 1) \tag{2.11}$$

$$\tau_{v,1} = \left(\frac{d_p^2 \rho_p}{18\mu}\right) [1 + 0.15 Re_p^{0.687}]^{-1} \quad \text{for} \quad (1 < Re_p < 1000). \tag{2.12}$$

If the mean free path of the gas were comparable to the particle size, the relaxation time would require a slip correction factor, C_c:

$$\tau_v = \frac{\rho_p d_p^2 C_c}{18}. \tag{2.13}$$

However, for helium at STP, the largest correction (for the smallest particle of interest) is less than 5% and can be neglected (Table 2.3).

Table 2.3: Slip correction factor values for air and helium at STP

Particle size	C_c in Air at STP	C_c for Helium at STP
10 μm	1.015	1.046
30 μm	1.005	1.015

The increase in particle velocity is given by the solution of Equation 2.10 (with the initial condition $u_p = 0$ at $t = 0$), which is obtained numerically accounting for the variation of $\tau_{v,1}$, due to changes in Re_p and μ_{cg}, (colored curves, Figure 2.3a).

To solve Equation 2.10, we first rearrange the differential equation to isolate u_p terms on one side.

$$\frac{du_p}{dt} + \frac{u_p}{\tau_{v,1}} = \frac{u}{\tau_{v,1}} \tag{2.14}$$

Then, using an integrating factor for a first-order differential equation, $e^{\int \frac{1}{\tau_{v,1}} dt} = e^{t/\tau_{v,1}}$, we can multiply and and rearrange to yield Equation 2.15.

$$e^{t/\tau_{v,1}} \frac{du_p}{dt} + e^{t/\tau_{v,1}} \frac{u_p}{\tau_{v,1}} = e^{t/\tau_{v,1}} \frac{u}{\tau_{v,1}} \tag{2.15}$$

The left side of the previous equation then becomes the derivative of $e^{t/\tau_v} u_p(t)$ with respect to t. Integrating both sides with respect to t gives the equation Equation 2.16.

$$\int \frac{d}{dt} \left(e^{t/\tau_{v,1}} u_p(t) \right) dt = \int e^{t/\tau_{v,1}} \frac{u(t)}{\tau_{v,1}} dt \tag{2.16}$$

Applying the fundamental theorem of calculus and ignoring the constant of integration for now yields Equation 2.17.

$$e^{t/\tau_{v,1}} u_p(t) = \int e^{t/\tau_{v,1}} \frac{u(t)}{\tau_{v,1}} dt \tag{2.17}$$

Finally, solving for $u_p(t)$ and integrating from 0 to t yields Equation 2.18.

$$u_p(t) = \exp\left(-\frac{t}{\tau_{v,1}}\right) \frac{1}{\tau_{v,1}} \int_0^t u(t') \exp\left(\frac{t'}{\tau_{v,1}}\right) dt' \tag{2.18}$$

The variation of $\tau_{v,1}$ with axial position in the capillary due to the increase in carrier gas velocity and decreases in density, viscosity and relative velocity with respect to the particle are modest (e.g., Re_p decreases less than 1.5-fold from ∼190 to ∼120 and carrier gas viscosity decreases less than 1.3-fold $\mu_{cg} \sim \sqrt{T}$), causing approximately a 25% variation in the following factor in (Equation 2.12),

$$\frac{1}{\mu_{cg}[1 + 0.15 Re_p^{0.687}]} \tag{2.19}$$

to vary from 0.155 to 0.202 $s \cdot \frac{m}{kg}$ (varying less than 3% in the range 0.190 ± 0.006 $s \cdot \frac{m}{kg}$ while the particle moves from z_p = 25 mm to 120 mm).

By the time the particle reaches the end of the barrel, $z_p = L$ = 120 mm, u_p reaches approximately 70% of the gas velocity. In our ideal scenario where the gas approaches Mach 1 (approximately 800 m/s for helium) at the exit and a 30 µm diameter particle reaches approximately 580 m/s.

2.4 Deceleration of the particles through quiescent air (Regime 2)

As the particle transitions from an accelerating gas flow into still air ($u = 0$ in Equation 2.10, where air (viscosity = 1.8×10^{-5} Pa · s, air density = 1.225 kg/m^3) after it leaves the device (Re ∼ 400), the drag force changes sign and the particle decelerates.[13] It slows exponentially from its exit velocity, $u_{p,e}$, to rest (Equation 2.20, Figure 2.5) with relaxation time $\tau_{v,2}$ (Equation 2.21).

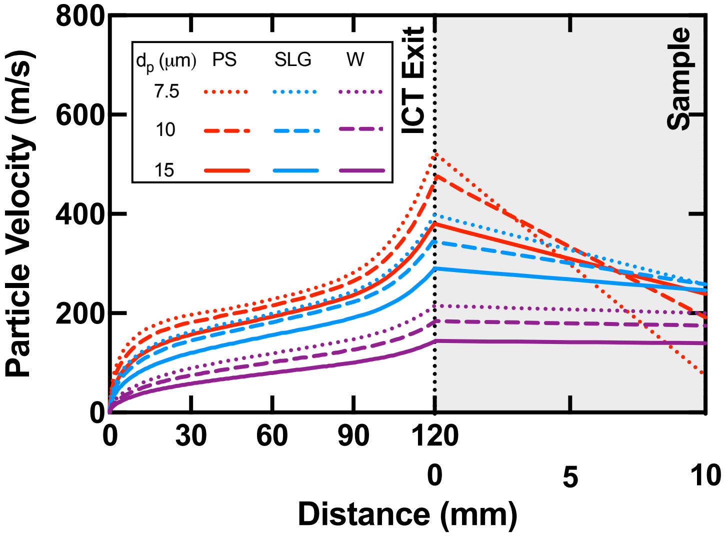

Figure 2.4: Predicted particle velocity profile through Regimes 1 and 2.

$$u_p(t) = u_{p,e} e^{-t/\tau_{v,2}} \tag{2.20}$$

$$\tau_{v,2} = \frac{\rho_p d_p^2}{18\mu_{air}} [1 + 0.15 Re_p^{0.687}]^{-1} \tag{2.21}$$

For a given particle diameter and density, its distance traveled, $S(t_2)$, obtained by integrating Equation 2.20, and consequently its stopping distance, S_∞, (the distance traveled before the velocity reaches zero) are proportional to its exit velocity, $u_{p,e}$,

$$S(t_2) = u_{p,e} \tau_{v,2} [1 - e^{-t_2/\tau_{v,2}}] \tag{2.22}$$

$$\text{which yields as } t \to \infty, \quad S_\infty = u_{p,e} \tau_{v,2}. \tag{2.23}$$

Particle delivery requires that the distance between the exit of the device and the cornea z_a must be less than S_∞ (i.e. the dimensionless distance, $\frac{z_a}{S_\infty} < 1$); the smaller the gap between the device and the cornea, the higher the particle velocity will be when it impacts the anterior surface of the cornea. Specifically, an expression for the velocity as a function of distance from the exit of the device (Figure 2.5a) is obtained by rearranging Equation 2.22,

$$1 - \frac{S(t)}{u_{p,e}\tau_{v,e}} = e^{-t/\tau_{v,e}}, \tag{2.24}$$

and eliminating the exponential in favor of the particle velocity Equation 2.20,

$$\frac{u_p(t)}{u_{p,e}} = 1 - \frac{S(t)}{u_{p,e}\tau_{v,e}}. \tag{2.25}$$

The particle velocity at impact, $u_{p,i}$, for impact distance, z_i = 1.0 cm (commonly used distance at which non-contact tonometers delivery air to the patient's cornea) and for particle sizes of interest for corneal drug delivery reveals the advantage of using larger particles: for a particle density similar to drugs ($\rho_p \sim 1$ kg/m^3), the 20 and 30 µm diameter particles retain above 70% of their exit velocity while smaller particles slow (10 µm) or even stop (5 µm) before impact (Table 2.4).

When considering particles of higher density, they retain their velocity much better through quiescent air. Soda lime glass particles (ρ_p = 2.85 g/cm^3) retain 70% of their exit velocity down to particle sizes of around 10 µm. All of the tungsten particles (ρ_p = 19.3 g/cm^3) in the sizes that was considered (5–30 µm) retain at least 88% of their exit velocity (Table 2.4).

In Figure 2.5, the fraction of initial exit velocity ($\frac{u_p}{u_{p,e}}$) from the tube is shown as a function of time and distance after the particle leaves the tube. When combining with the acceleration of the particles from Figure 2.3a, the velocity profiles of the particles are shown in Figure 2.4.

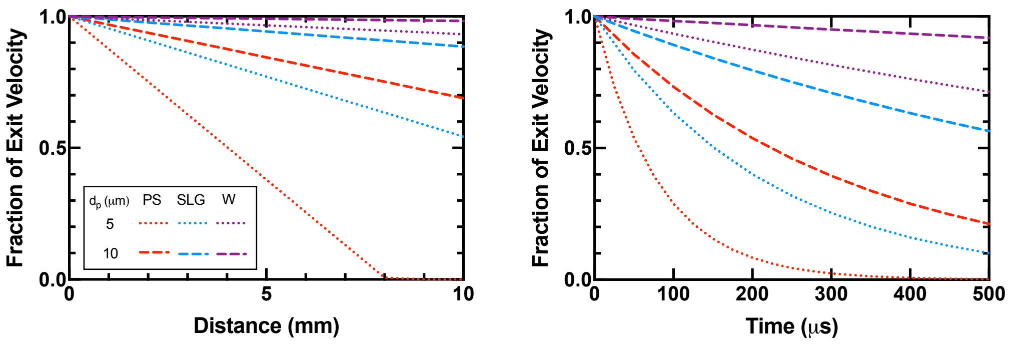

(a) Fraction of exit velocity vs distance

(b) Fraction of exit velocity vs time

Figure 2.5: Fraction of exit velocity (i.e., particle velocity divided by its exit velocity) as a function of distance and time. After the particle leaves the device, its velocity decays to zero as a function of a) time and b) distance traveled. Smaller particles decelerate faster than larger particles due to the quadratic dependence of $\tau_{v,2}$ on d_p (Equation 2.21). Results are shown for all particle having an exit velocity of 100 m/s, which enters in the expression for $\tau_{v,2}$ due to the correction for finite $\mathrm{Re_p}$.

2.5 Modeling penetration depth within the tissue (Regime 3)

In relation to the cornea, we seek delivery of particles into the epithelium and stroma (a depth at least 50 μm below the apical epithelium), but less than 400 μm (above the endothelium). The penetration depth is simply the distance a particle travels within a tissue before coming to rest due to the sum of the force acting on it as it moves through the tissue. Treating all of the forces as antiparallel to the direction of motion (e.g., neglecting particle rotation), permits scalars to describe the magnitude of each force: the frictional or viscous resistance (F_f), the inertia of the target material (F_i), and the yield force (F_y),[14]

$$m\frac{du_p}{dt} = \sum F = -(F_i + F_f + F_y). \tag{2.26}$$

The friction force is usually approximated using Stokes Law with a rate-independent tissue viscosity, μ_t,

$$F_f = 6\pi\mu_t r_p u_p(t). \tag{2.27}$$

Although tissue is expected to be viscoelastic, uncertainty in the treatment of this term might not be important. Prior research by Kendall and coworkers showed that frictional forces are negligible for skin penetrated by particles in the size range from 1 to 60 µm. They hypothesize that during particle impact, a thin film of fluid forms between the projectile and tissue, reducing friction to a negligible level compared to the inertial and yield forces[15,16,17]. Given the high-water content of the cornea, his observations may hold for the cornea, too.

Therefore, we approximate the force balance as

$$m\frac{du_p}{dt} = \sum F = -(F_i + F_y) = -\left(\frac{1}{2}\rho_t A_c u_p(t)^2 + 3A_c\sigma_y\right), \tag{2.28}$$

where the inertial resistance of the target material (here, a biological tissue) scales as the tissue density, the square of the instantaneous velocity of the particle and the cross-sectional area of the particle, and the yield force has been approximated as the force required to propagate a crack through the material if the process were quasi-static, which requires the particle to exert a pressure that is 3-times the yield stress independent of the particle velocity. Integration of Equation 2.28 gives the expression for penetration depth:

$$d = \frac{4\rho_p r_p}{3\rho_t}\left[\ln\left(\frac{1}{2}\rho_t u_{p,i}^2 + 3\sigma_y\right) - \ln(3\sigma_y)\right]. \tag{2.29}$$

Unfortunately, there is scant data to test the validity of the quasi-static crack propagation approximation. For skin, Kendall notes that a yield stress that is twice the maximum value reported in prior literature ($\sigma_y \sim 4.9 - 22$ MPa for skin) is required

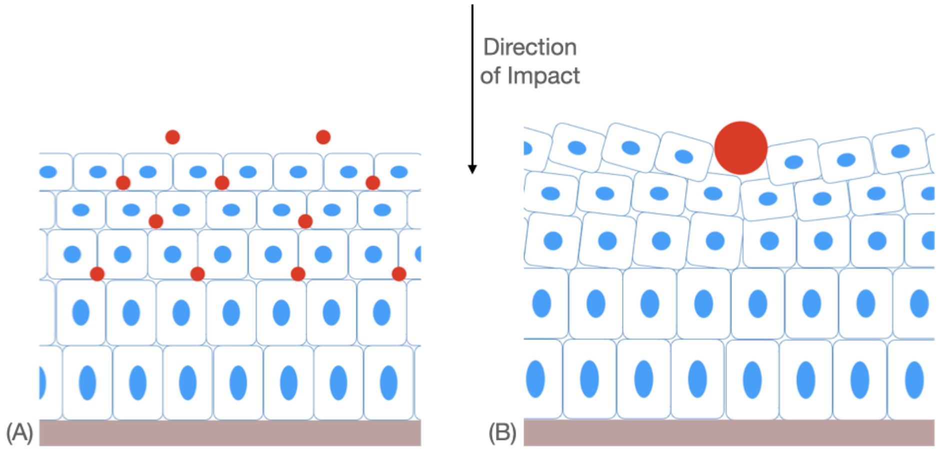

Figure 2.6: A simple schematic showing the two possible tissue failure mechanisms. (A) An intracellular mechanism for smaller particles where they can pass through the cells directly. (B) An extracellular mechanism for larger particles where they have to disrupt the layering of cells in order to pass through. The direction of impact is from above, as denoted in the image.

to describe their experimental results ($\sigma_y \sim 40$ MPa best fit Kendall's particle penetration vs impact velocity data).[15] This disparity causes Kendall to question the quasi-static assumption: literature "tensile tests do not take into account the high local strain rates that occur in the tissue upon particle impact." Furthermore, Kendall speculates that the mechanism of penetration may depend on particle size, particularly for particles of sizes comparable to biological cells and extracellular matrix structures (Figure 2.6).[18] Specifically, for particles that are larger than epithelial cells, such as polystyrene particles of diameter > 15um, Kendall envisions yielding through an extracellular mechanism of failure (Figure 2.6), with relatively low yield stress $\sim$ 1 MPa. In contrast, smaller particles (e.g., 1–3 μm diameter, gold) penetrate intracellularly passing through individual cell membranes (for which Kendall estimates 10 MPa yield stress). Thus, at the outset of this thesis, it is not possible to predict the depth that the particles will reach: the values of key parameters are unknown (especially the tissue yield stress as a function of strain rate and relative size of the particle compared with structural length scales of the tissue).

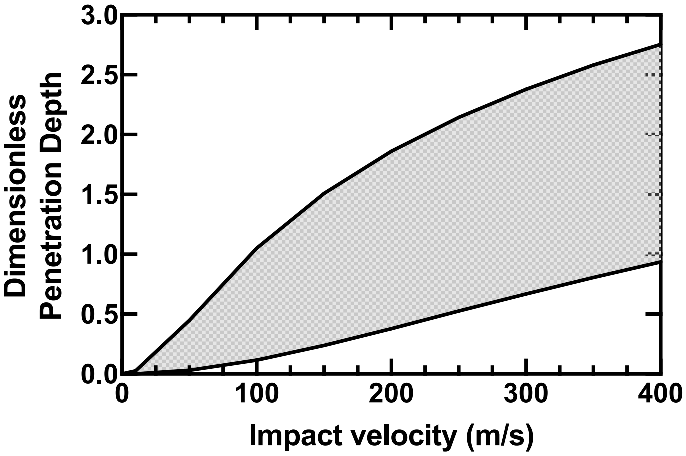

Figure 2.7: An estimation of non-dimensionalized penetration depth ($\frac{d\rho_t}{2r_p\rho_p}$) as a function of impact velocity calculated using Equation 2.28 for yield stress values spanning 0.5 to 5 MPa. The huge uncertainty in the penetration depth is due primarily to the unknown yield stress of the corneal tissue.

Despite the large uncertainty in the yield stress, the model can be used for a feasibility calculation using the entire range of yield stress values in the literature to calculate the envelope of possible penetration depth, d, as a function of impact velocity, $u_{p,i}$ (Figure 2.7). The result suggests that accessible impact velocity values should enable particles to penetrate at least one particle diameter ($\frac{d}{2r_p} = 1$). For example, if the particle's density is twice that of the tissue ($\frac{\rho_p}{\rho_t} = 2$), the critical velocity to penetrate one particle diameter is in the range from 50 m/s to 250 m/s (Figure 2.7, reading from the graph the velocity range for dimensionless penetration $\frac{d\rho_t}{2r_p\rho_p} = 0.5$). Even the highest of these velocities should be accessible using a device that protects the patient's eye from the carrier gas (Figure 1.4).[3,19] Thus, the model indicates feasibility of particle delivery, with uncertainly in the degree of difficulty.

One limitation to consider is the maximum penetration into the cornea — specifically, whether particles can penetrate beyond the endothelium, which is located 450–500 μm from the anterior surface of the eye. Our model predicts that for both polystyrene and soda lime glass particles, even if the impact velocity were to reach

Mach 1 (a scenario that not possible traveling through ambient air), these particles would only penetrate approximately half of the corneal thickness, about 250 µm. In the case of tungsten, our model suggests that if impact velocities for 15 µm particles could achieve Mach 1, or Mach 0.5 for 20 µm particles, then these particles might have the necessary momentum to penetrate the full thickness of the cornea. However, achieving such impact velocities would require a 3-4 fold increase in particle acceleration requiring a clinically insignificant tube length.

To better understand the properties of the cornea, exploring questions of the role of deformation rate and particle size relative to natural length scales of the tissue, we will first establish the range of particle sizes and velocities that can produced using Groisman's general design. There is no literature on the role of device geometry and operating conditions on the velocity and yield of particles leaving the device. To gain this information, we present a novel apparatus that permits experimental quantification of these performance metrics as functions of the geometry of the gas diversion unit (particularly the number of orifice discs, their spacing and orifice sizes) and the operating conditions (inlet pressure, vacuum pressure, and particle size).

2.6 New apparatus design

Groisman's ballistic delivery device provides the unique ability to eliminate injury due to high velocity gas that can severely damage biological tissues. We designed an apparatus (Figure 2.8a) to study the effects of the geometry of the gas diversion unit and vacuum pressure that diverts the carrier gas. The device retained the previously established ability to vary the inlet pressure, mass and size of particles loaded and device-to-sample distance. The new design facilitated changing the orifice size, number and position of the orifice discs, and the strength and symmetry of the imposed vacuum in the gas diversion unit. Anticipating potential clinical

Table 2.4: Predicted penetration depth for particle types

Particle type	d_p	**Exit Velocity (m/s)**	**Impact[4] Velocity (m/s)**	**% Velocity Retained**	**Predicted Penetration Depth (µm)**	**Normalized Penetration Depth**
PS[1]	5	569	0	0%	0.0	0.0
	7.5	523	74.6	14.3%	1.6	0.2
	10	476	192	40.3%	8.5	0.9
	15	380	238	62.6%	16.0	1.0
	20	341	252	73.9%	22.6	1.1
	30	293	247	84.3%	33.2	1.1
SLG[2]	5	492	209	42.5%	12.7	2.5
	7.5	398	257	64.6%	23.4	3.1
	10	344	258	75.0%	31.4	3.1
	15	290	246	84.8%	44.9	3.0
	20	238	212	89.1%	51.5	2.6
	30	205	191	93.2%	68.8	2.3
W[3]	5	267	237	88.8%	97.8	19.6
	7.5	215	200	93.0%	122.7	16.4
	10	184	175	95.1%	140.4	14.0
	15	144	140	97.2%	158.8	10.6
	20	121	118	97.5%	166.8	8.3
	30	95	93.7	98.6%	176.1	5.9

[1] Polystyrene (PS), density: 1.05 g/cm^3

[2] Soda Lime Glass (SLG), density: 2.85 g/cm^3

[3] Tungsten (W), density: 19.3 g/cm^3

[4] Standoff distance 10 mm. Inlet pressure 100 psi. Assumes atmospheric pressure at exit of inner capillary tube.

translation, we designed the apparatus from commercially available components (mainly acquired from Thorlabs, Newton, NJ, USA), custom modified as needed (documented in SOLIDWORKS to facilitate automated production, numerically controlled machining demonstrated by the Caltech Instrument Shop). We studied the mass fraction of particles delivered and the spatial distribution (radial and depth) of delivered particles as functions of the following parameters (Table 2.5), for which no literature exists today.

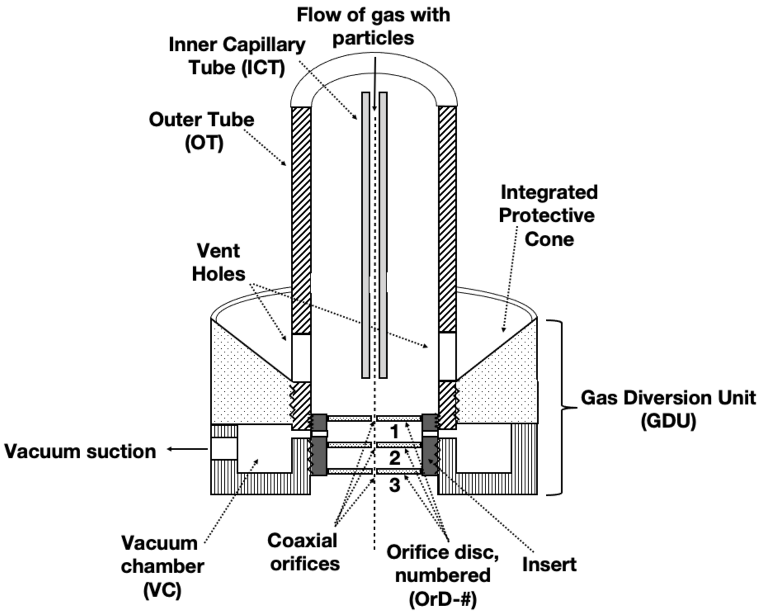

(a) New apparatus design for biolistic drug delivery

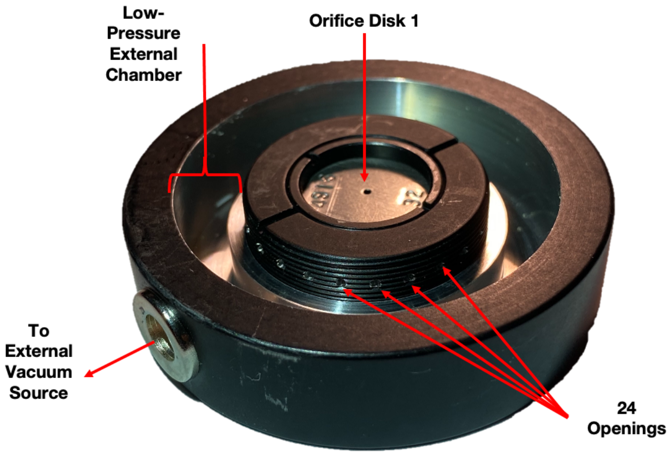

(b) Gas Diversion Unit of our device

Figure 2.8: Our proposed design that integrates a more uniform vacuum suction, interchangeable orifice discs (with difference orifice sizes), and varying orifice disc gap distance. To minimize the lateral deflection of particle trajectories, the new gas diversion unit (GDU) has 24 evenly spaced openings to provide symmetric flow of carrier gas outward to a low-pressure vacuum chamber (VC) allowing particles to continue on axis and pass through the coaxial orifices. The GDU can be disassembled for inspection of the various surfaces within it to characterize the spatial distribution of particle loss.

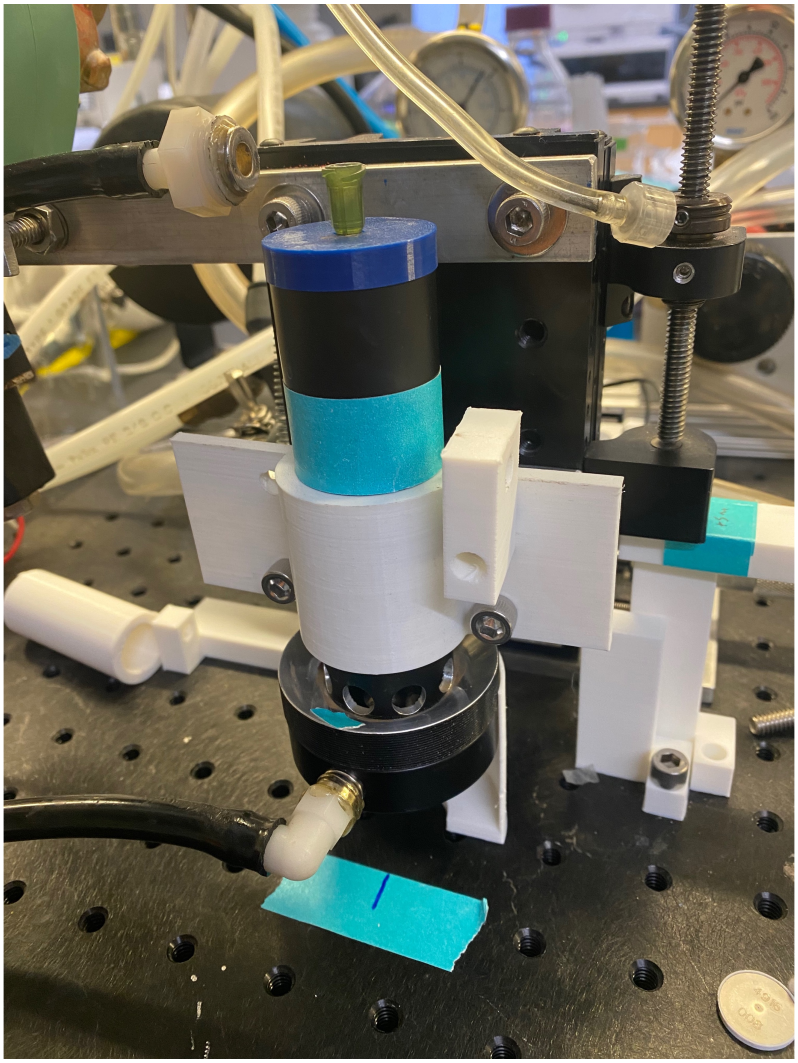

Figure 2.9: Photograph of our biolistic microparticle delivery device

Figure 2.10: Cartridges were prepared by loading 0.5 μL of 1% w/w 5–22 μm silver-coated soda lime glass particles in water/ethanol mixture.

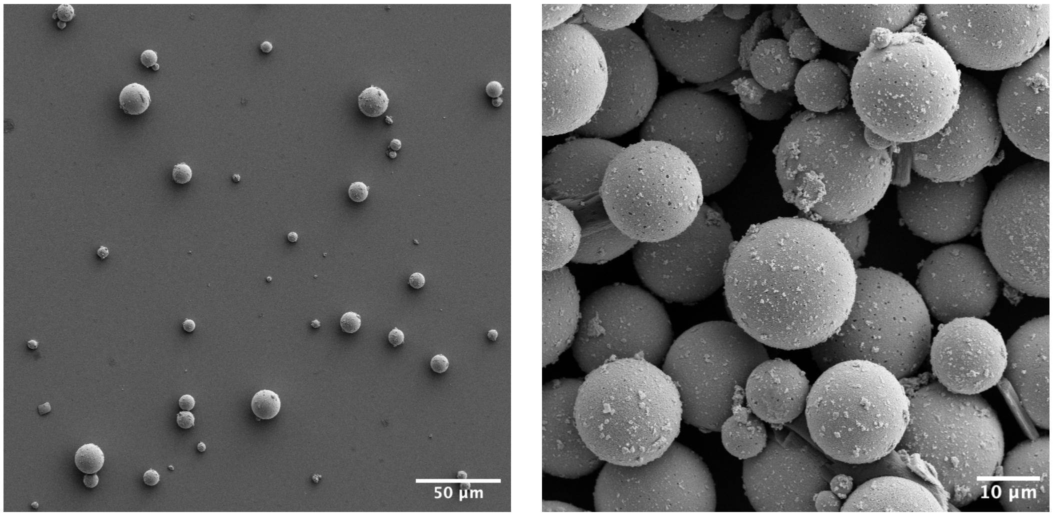

(a) Mag = 150x, EHT = 5.00 kV (b) Mag = 1000x, EHT = 10.00 kV

Figure 2.11: Scanning electron micrographs of silver coated soda lime glass particles (ρ_p = 2.85 g/cm^3).

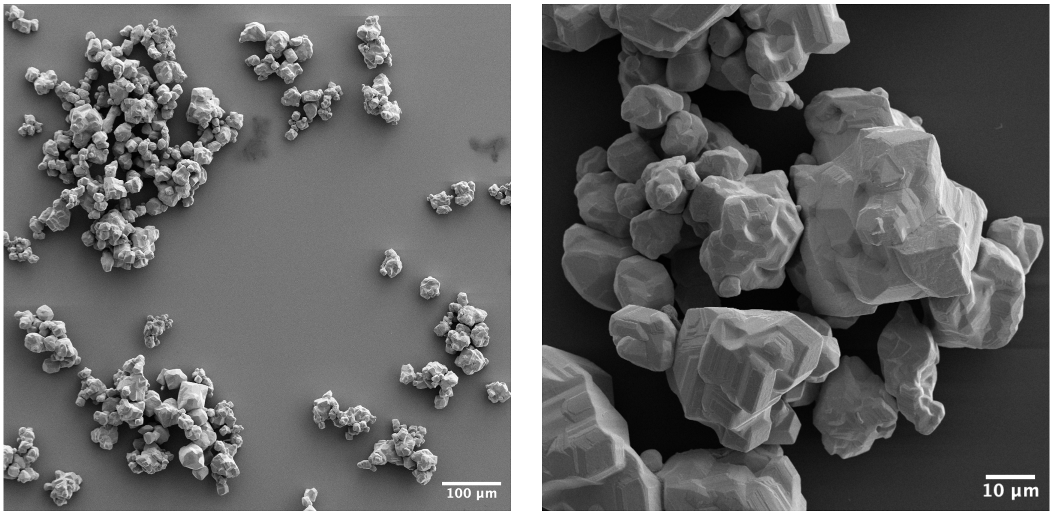

(a) Mag = 100x, EHT = 10.00 kV (b) Mag = 750x, EHT = 10.00 kV

Figure 2.12: Scanning electron micrographs of tungsten (ρ_p = 19.3 g/cm^3).

2.7 Materials and methods

Agarose gels as a surrogate for corneal tissue

To characterize the penetration with our novel ballistic delivery device, particles were delivered into agarose gels, which is used in lieu of direct measurement of velocity vs. distance from the device exit. Gels were prepared by mixing 1% w/w agarose (Sigma Aldrich, St. Louis, MO) gels into PBS, heating until the solution boils and then poured into petri dishes to achieve a thickness of approximately 500 µm. Gels in petri dishes were sealed with Parafilm and placed in the refrigerator at 4°C for at least 30 minutes prior to use, and were used within 48 hours of preparation.

Microparticle delivery parameters

Three types of particles with differing densities (Table 2.2) — polystyrene particles (ρ_p = 1.05 g/cm^3, Cospheric, Somis, CA) ranging from 10 to 30 µm diameter, silver-coated soda lime glass microspheres (ρ_p = 2.85 g/cm^3, Cospheric, Somis, CA) ranging from 5 to 22 µm diameter, and tungsten particles (ρ_p = 19.3 g/cm^3, US Research Nanomaterials, Houston, TX) were ballistically delivered into these gels with varying parameters (Table 2.5) — inlet pressures (50–150 psi), standoff distances (5–15 mm), orifice sizes (200–400 um), and orifice setup (2–3 disks). The device used was the custom modified pneumatic capillary gun as described in Section 2.6. Unless otherwise noted, all deliveries were performed using vacuum of –10 psi (–69 kPa) in the GDU.

Imaging of agarose gels and data processing

Immediately following particle delivery, agarose gels were imaged with optical coherence tomography using a Ganymede 210 Series Spectral Domain OCT imaging System with an OCTP-900 scanner and 8 m later resolution scan lens (Thorlabs, Newton, NJ). Three-dimensional images with pixel sizes of 2.03 µm (x) by 2.03 µm

Table 2.5: Parameters along with their ranges to be evaluated

Parameter	**Definition**	**Range**
r_O	Orifice sizes	200 to 300 µm
z_a	Standoff distance to target	5 to 15 mm
p_i	Inlet pressure	50 to 150 psi
d_p	Particle diameter	5 to 30 µm
n_o	Number of orifice discs	2 to 3

(y) by 2.03 µm (z) were acquired using the medium speed, medium sensitivity of 15 kHz A-scan rate or the low-speed, high sensitivity of 5.5 kHz A-scan rate. Images were exported as a three-dimensional stack of XZ-slices. Images were processed using FIJI (FIJI Is Just ImageJ) and the built-in 3D object counter plugin was used to identify spherical particles with diameters within 5–25 µm. Statistics containing the particles position as well as the gel's surface was then exported and analyzed using custom Python code, which would determine each particle's depth within the gel.

2.8 Results and discussion

Our studies of this particular ballistic delivery device centered on its clear advantage in its clinical application — namely, it delivered high speed microparticles into targets with minimal gas damage. In previous work in our group, ballistic particle delivery mainly focused on the Bio-Rad PDS-1000, which accelerated particles to high speeds with particles riding a rupture disc in a vacuum chamber. The vacuum chamber presents one obvious downside — it cannot be used in a clinical setting where the *in vivo* cornea can be placed in the chamber. Another downside is the mechanism at which particles are propelled into the target. A microcarrier carrying microparticles is accelerated by gas whereby a stopping screen catches the microcarrier and only allows the microparticles to continue towards the target. Along

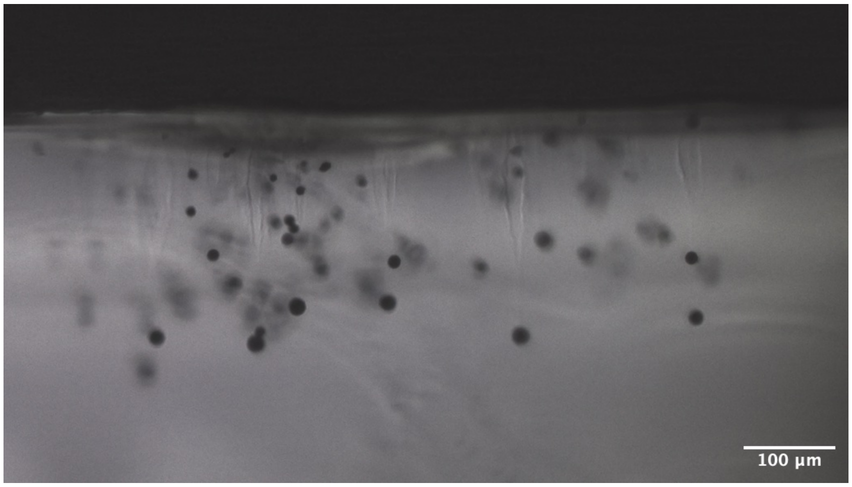

Figure 2.13: Representative side profile image of soda lime glass particles of density, ρ_p = 2.85 g/cm^3, delivered into 1% w/w agarose gel. Particles were delivered with the following instrument parameters: inlet pressure p_i = 125 psi (862 kPa), standoff distance z_a = 10 mm and three orifice discs with 200 µm diameter orifice. Larger particles tended to penetrate deeper, while smaller particles were found closer to the surface.

with the microparticles is the movement of air towards the target, and at pressures used in the PDS-1000, would result in tissue damage.

In our device, we aimed to solve both deficiencies, by diverting all outlet gas flow and allowing this to be used in a clinical setting (for example, we could modify it as a handheld device that can be pressed onto an animal's body). We needed to study the flow of the particles because unlike the PDS-1000, where every microparticle despite its size travels at the same velocity towards the target, in our device, particles are entrained in a gas flow meaning different sized particles would reach different speeds. These particles then pass through stagnant, ambient air, where they are decelerated, again, the particle's properties play a role in their deceleration, before reaching the target. The penetration into the target should behave similarly to previous studies, but considering the path the particle takes to reach that initial entry into the target is crucial.

We began by examining soda lime glass particles (density = 2.85 g/cm^3), with particle diameters ranging from 5 to 22 µm, because based on our models, their density and diameters offer the most promise in penetrating into corneal tissue. Polystyrene particles were initially examined but due to their low density, we hypothesized that while they would accelerate up to speed, they would also decelerate quite quickly through ambient air, effectively diminishing their penetrating power. Tungsten particles provided the most penetrating power, but given their high density, particles may not reach sufficient speeds in order for sufficient penetration.

Standoff distance affects smaller particles as well as spatial resolution

Initial observations confirm that shorter standoff distances reduce the radial distribution of the particles found within the agarose gel (Figure 2.14). Furthermore, we noted a 2–3 fold increase in the presence of particles with diameters of 10–14 microns at shorter distances (Figure 2.15). This observation is supported by quantitative measurements using microscopic analysis, which revealed a clear gradient in particle distribution as a function of distance. This increased penetration at shorter distances can be attributed to reduced air resistance and the maintenance of particle velocity, which are critical factors in overcoming the gel's resistance.

Regarding particles achieving normalized depths greater than 2, our data indicate a distinct pattern. These particles, which successfully penetrate deep into the gel rather than merely adhering to the surface, predominantly belong to the 10–14 micron diameter range. At standoff distances of 5 mm, a significant proportion of these particles managed to achieve such penetration depths, whereas at 15 mm, the occurrence of deep penetration markedly decreased. This trend underscores the influence of standoff distance on the effective delivery of therapeutic particles.

Particles of 12 microns in diameter or smaller showed an insignificant contribution to deep penetration, even in the relatively less dense agarose gel compared to the

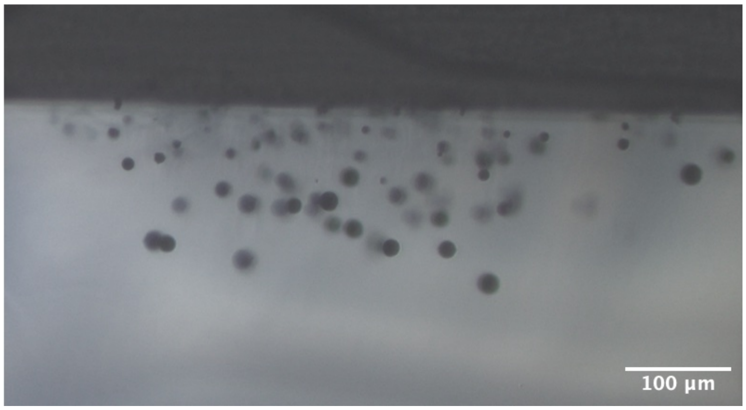

(a) Cross sectional view of soda lime glass particles in 1% w/w agarose gel

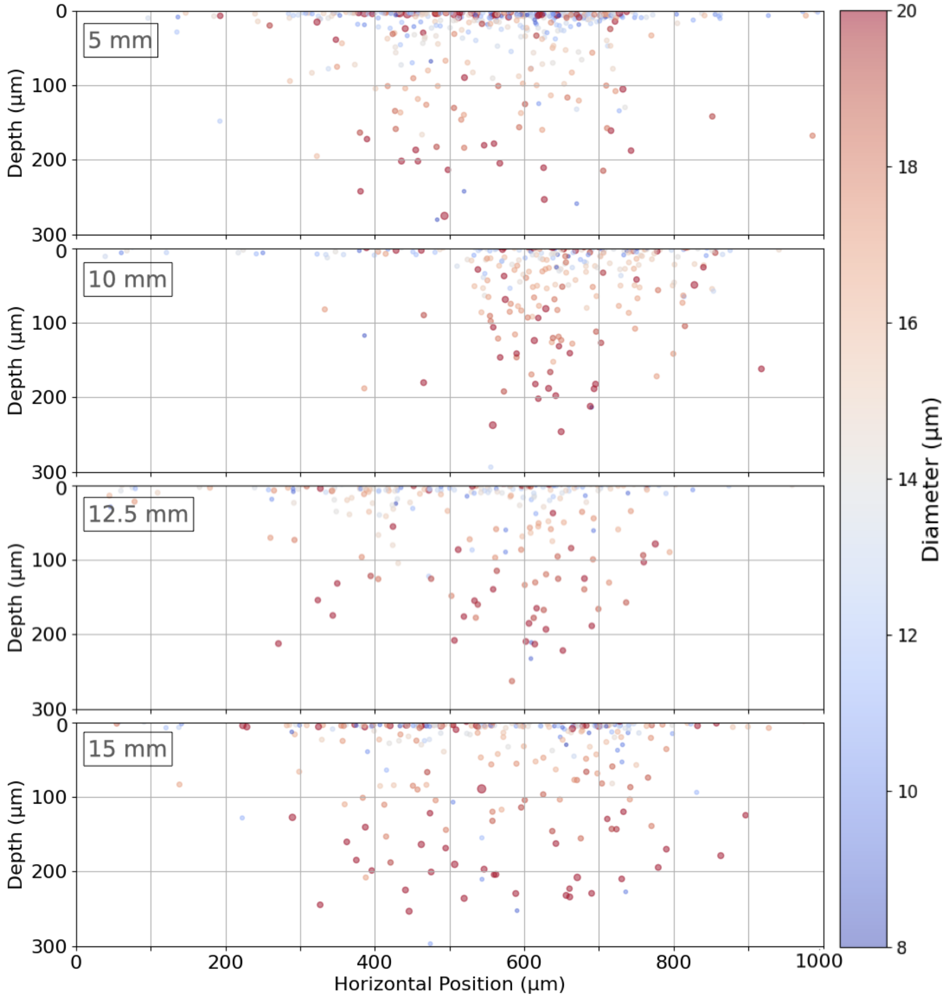

(b) Soda lime glass particle distribution in 1% w/w agarose

Figure 2.14: Penetration depth and horizontal positions of silver-coated soda lime glass particles (ρ_p = 2.85 g/cm^3) in 1% w/w agarose as a function of standoff distance increasing from top to bottom (5, 10, 12.5, 15 mm) for the following instrument parameters: p_i = 125 psi (862 kPa), 3 orifice discs with 200 µm diameter orifice size. Each symbol represents a single particle. The relative size of the symbol represents their relative diameter. Results from n = 4 replicates are pooled.

corneal tissue. This observation suggests a threshold effect where smaller particles, despite their higher initial velocities, lack sufficient momentum to overcome the surface resistance of the gel. In contrast, particles in the 14–16 micron range represent a transitional phase, exhibiting significant penetrating power at a 5 mm standoff distance, which diminishes with increased air travel.

The 14–16 micron particles serve as an inflection point in our study (Figure 2.15). Within this size range, the particles exhibit a notable decrease in penetration efficacy as the standoff distance increases. This trend is particularly evident in the data showing a higher percentage (62.5% to 77.1% to 78.0% to 83.0%) of these particles failing to penetrate the gel surface at greater distances. This finding provides valuable insights into the balance between particle size and travel distance, suggesting an optimal range for effective drug delivery in ophthalmologic applications.

Larger particles, particularly those in the 16–20 micron range, presented an interesting dynamic. Our model predicted that these larger particles would retain more momentum through the stagnant air, a hypothesis that was corroborated by our experimental data. These particles, despite potentially lower exit velocities from the delivery device, maintained sufficient momentum to penetrate the agarose gel effectively. This behavior highlights the importance of considering both particle size and delivery dynamics in designing effective ophthalmologic therapies.

The findings regarding 16–20 micron particles are particularly relevant for clinical applications. Their size makes them visually imperceptible, reducing potential discomfort or visual disturbances for patients. Additionally, their effective penetration at a range of standoff distances from 5 to 15 mm underscores their suitability for varied clinical scenarios, offering flexibility and forgiveness in the delivery process. This adaptability is vital for designing clinically viable ophthalmologic treatments that are both effective and patient-friendly.

When examining the effect of standoff distance to the radial distance from the mass center (Figure 2.17), the weight of particles found at increased distances (300–500 µm) away from the mass center increases as the standoff distance increases from 5 mm to 15 mm. For clinical relevance, this suggests that the smaller the standoff distance, the finer the spatial resolution achieved in particle delivery. Commercialized gene guns such as the Helios gene gun uses a standoff distance of 2.8 cm (Figure 1.3), in part because they use distance to reduce the damage caused by the exit gas on the target. As a result, the dispersion of the particles which the manufacturer estimates to be over 2 cm wide (20% of the diameter of a human cornea).

Our experimental setup was designed to examine the precision of particle delivery in relation to standoff distance, with a particular focus on the dispersion pattern upon impact with the target. Utilizing a 200 µm exit orifice, our data indicates that at a standoff distance of 10 mm, the particles maintain a collimated trajectory and disperse over a confined area of approximately 1 mm by 1 mm on the agarose target. This collimation results in a maximal deflection angle of roughly 3.5 degrees when a single orifice disc is used. However, the alignment of three consecutive orifice discs significantly reduces this angle, ensuring that particles exit the delivery device and travel almost perpendicular to the target surface, as detailed in Section 2.10.

In ophthalmologic applications, the precision of drug delivery is crucial for both efficacy and safety. The non-contact tonometer sets a benchmark for standard distance in diagnostic equipment, prompting an investigation into the optimal standoff distance for particle delivery in therapeutic contexts. We hypothesize that closer standoff distances lead to increased penetration depths due to higher particle velocity, primarily because particles decelerate less over shorter distances, maintaining higher impact velocities upon entering the target, in this case, agarose gel. This study selected standoff distances ranging from 5 mm to 15 mm, based on preliminary tests that indicated this range as potentially significant for particle penetration.

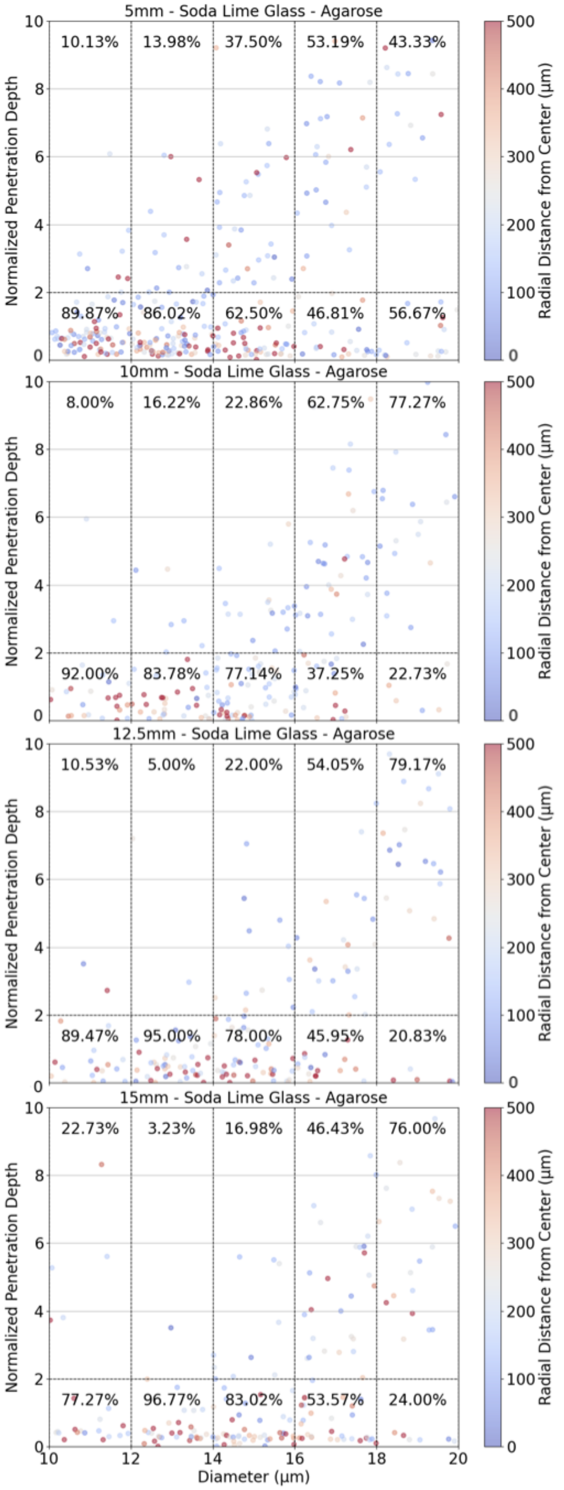

Figure 2.15: Distribution of normalized penetration depth d/D_p, from 0–2 and 2–10 for soda lime glass particles (ρ_p = 2.85 g/cm^3) in 1% w/w agarose as a function of standoff distance increasing from top to bottom (5, 10, 12.5, 15 mm) for the following instrument parameters: p_i = 125 psi (862 kPa), 3 orifice discs with 200 µm diameter orifice size. Particles were binned by their diameter in 2 µm intervals and their distance from the XY-center is shown on the color bar. Percentage of particles in each bin that is found between normalized penetration depth 0–2 and 2–10 is shown on each graph. Each symbol represents a single particle. Results from n = 3 replicates are pooled.

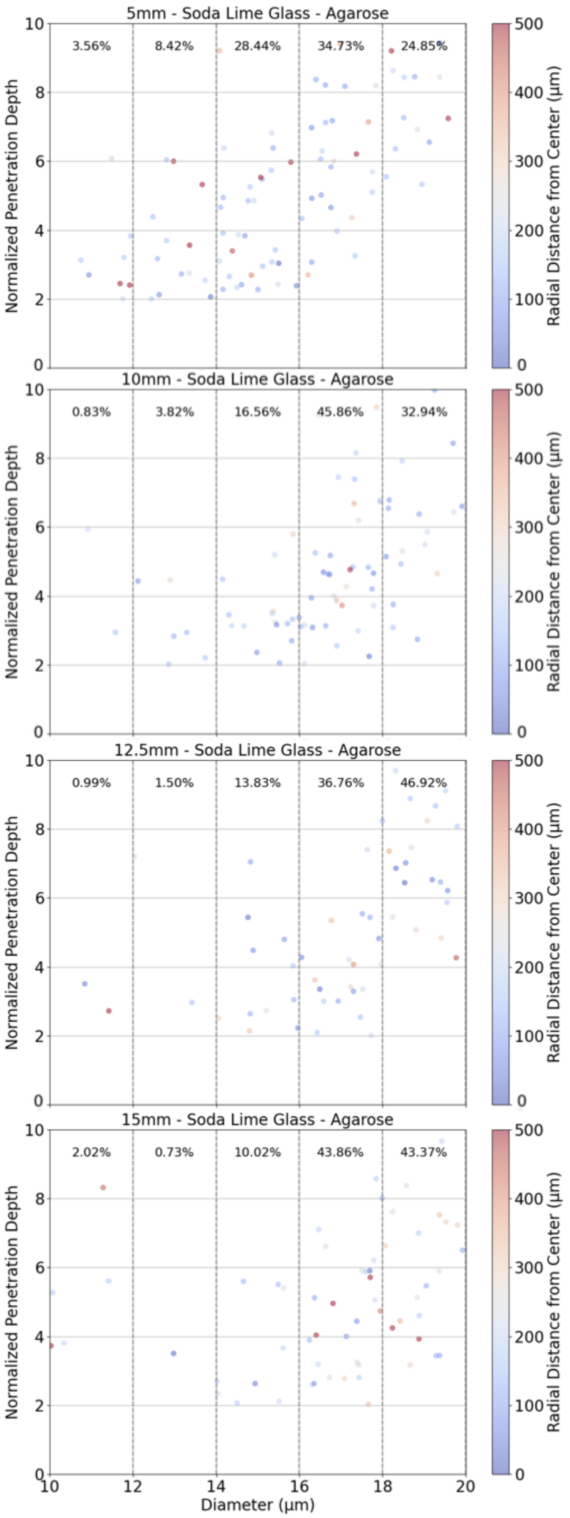

Figure 2.16: Distribution of normalized penetration depth d/D_p, from 0–2 and 2–10 for soda lime glass particles (ρ_p = 2.85 g/cm^3) in 1% w/w agarose as a function of standoff distance increasing from top to bottom (5, 10, 12.5, 15 mm) for the following instrument parameters: p_i = 125 psi (862 kPa), 3 orifice discs with 200 μm diameter orifice size. Particles were binned by their diameter in 2 μm intervals and their distance from the XY-center is shown on the color bar. Weight fraction that is found between normalized penetration depth 2–10 is shown on each graph. Each symbol represents a single particle. Results from n = 3 replicates are pooled.

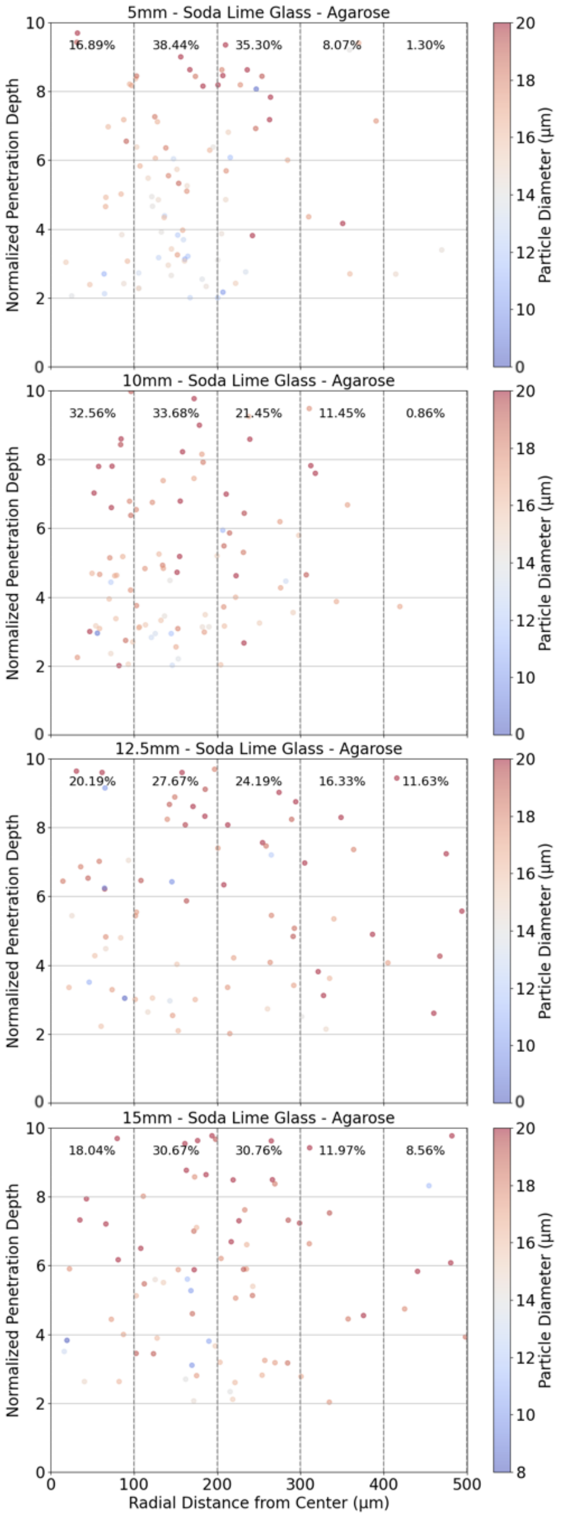

Figure 2.17: Distribution of normalized penetration depth d/D_p, from 2–10 for soda lime glass particles (ρ_p = 2.85 g/cm^3) in 1% w/w agarose as a function of radial distance and standoff distance increasing from top to bottom (5, 10, 12.5, 15 mm) for the following instrument parameters: p_i = 125 psi (862 kPa), 3 orifice discs with 200 μm diameter orifice size. Particles were binned by their diameter in 2 μm intervals and their distance from the XY-center is shown on the color bar. Weight fraction that is found between normalized penetration depth 2–10 is shown on each graph. Each symbol represents a single particle. Results from n = 3 replicates are pooled.

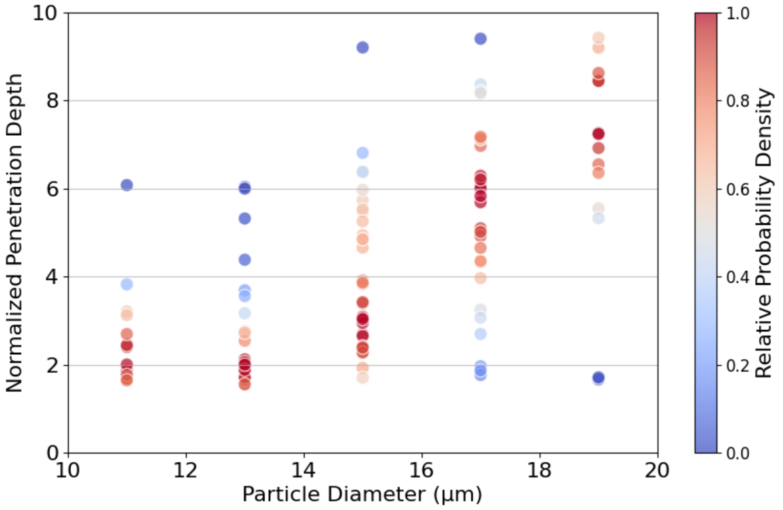

(a) 5 mm standoff distance

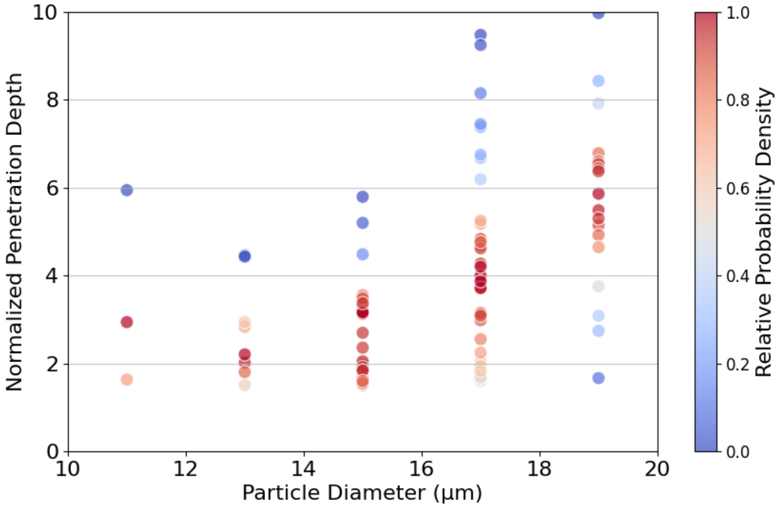

(b) 10 mm standoff distance

Figure 2.18: Distribution of normalized penetration depth d/D_p, for soda lime glass particles (ρ_p = 2.85 g/cm^3) in 1% w/w agarose as a function of standoff distance increasing from top to bottom (5, 10, 12.5, 15 mm) for the following instrument parameters: p_i = 125 psi, 3 orifice discs with 200 µm diameter orifice size. Only particles with d/D_p between 1.5 and 10 are shown. Particles were binned by their diameter in 2 µm intervals and their relative probability density is shown on the color bar. Results from n = 3 replicates are pooled.

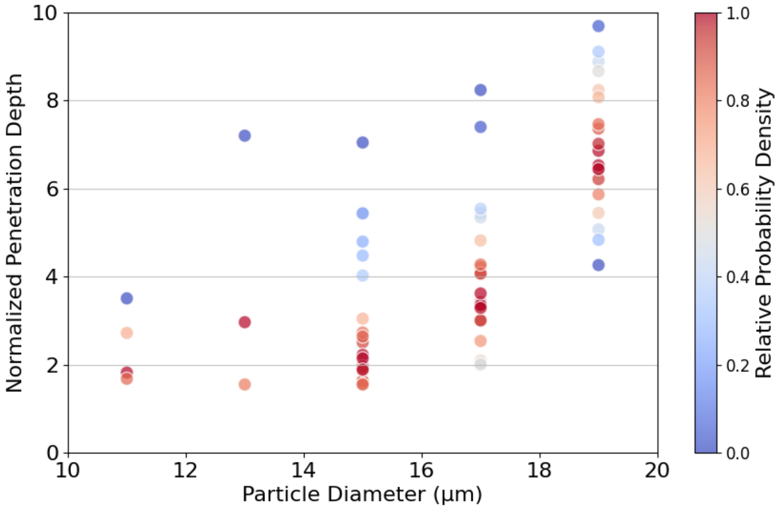

(c) 12.5 mm standoff distance

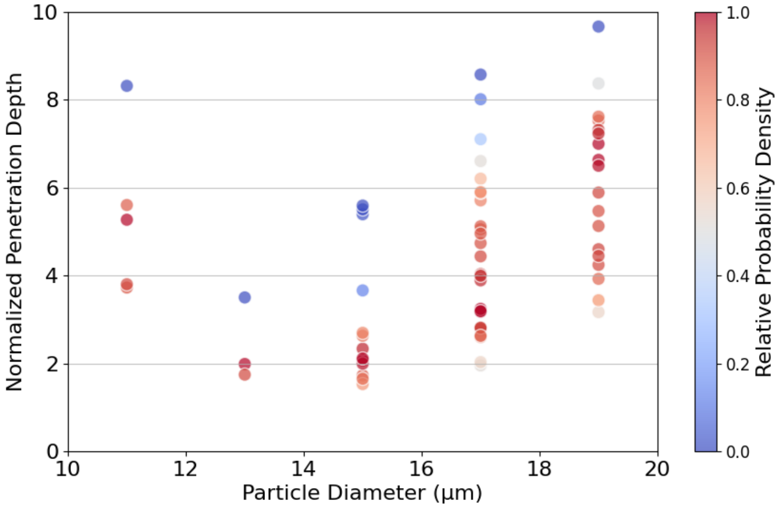

(d) 15 mm standoff distance

Figure 2.18: Distribution of normalized penetration depth d/D_p, for soda lime glass particles (ρ_p = 2.85 g/cm^3) in 1% w/w agarose as a function of standoff distance increasing from top to bottom (5, 10, 12.5, 15 mm) for the following instrument parameters: p_i = 125 psi, 3 orifice discs with 200 μm diameter orifice size. Only particles with d/D_p between 1.5 and 10 are shown. Particles were binned by their diameter in 2 μm intervals and their relative probability density is shown on the color bar. Results from n = 3 replicates are pooled.

These distances also mirror the practical constraints faced in clinical ophthalmologic settings.

As we scrutinize the impact of varying standoff distances, our hypothesis that reduced distances would correlate with more concentrated particle distribution was confirmed. This was most evident in the 5 mm standoff distance experiments, where the majority of the particle weight fraction is centralized within 200 µm of the target's center. However, as the standoff distances increase to 10, 12.5, and 15 mm, we observe a discernible shift in particle dispersion. With greater distance comes a reduction in particle velocity and an increased vulnerability to air resistance, leading to a broader spread of particles across the agarose surface. This pattern of dispersion underscores the delicate balance between standoff distance and particle velocity in achieving targeted and spatially controlled delivery.

Inlet pressure shows weak effect on penetration depth

The flow of particles through the ICT (Regime 1) was expected to be driven by the pressure gradient. We expected inlet pressure and by extension, pressure gradient, down our capillary tube to drive the flow of particles and accelerate them in Regime 1. Naturally, it would be easy to hypothesize that as the pressure difference increases, the higher the gas velocity would be. Even if the maximum gas velocity is limited by reach sonic speeds, we would expect the velocity to reach the maximum speed earlier, allowing for a larger gradient between particle and gas velocity to drive the velocity of the particles. Thus, when keeping the physics of the particle in Regimes 2 and 3 constant, it would be logical to assume that a higher pressure gradient would allow for deeper penetration depths in the target because the particle would exhibit a higher exit velocity, translating to a higher impact velocity.

However, our studies show that pressure has almost no correlation to penetration depth in the agarose gels (Figure 2.19 and Figure 2.20). As shown with the prior

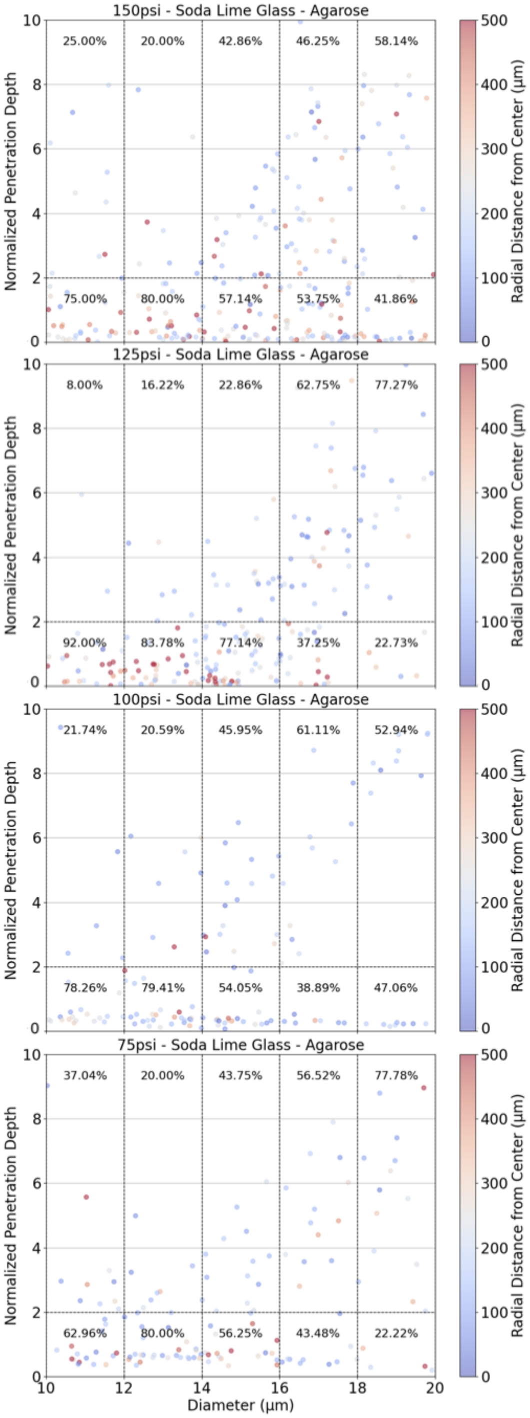

Figure 2.19: Distribution of normalized penetration depth d/D_p, for soda lime glass particles (ρ_p = 2.85 g/cm^3) in 1% w/w agarose as a function of inlet pressure decreasing from top to bottom (150, 125, 100, 75 psi) for the following instrument parameters: z_a = 10 mm, 3 orifice discs with 200 μm diameter orifice size. Particles were binned by their diameter in 2 μm intervals and their distance from the XY-center is shown on the color bar. Percentage of particles in each bin that is found between normalized penetration depth 0–2 and 2–10 is shown on each graph. Each symbol represents a single particle. Results from n = 3 replicates are pooled.

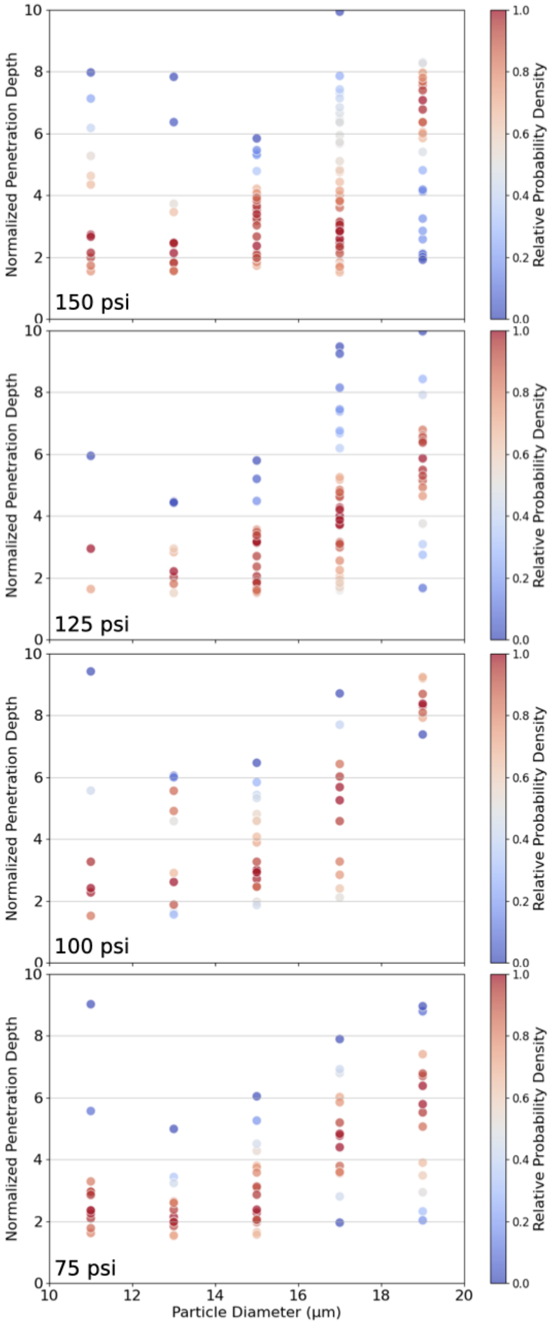

Figure 2.20: Distribution of normalized penetration depth d/D_p, for soda lime glass particles (ρ_p = 2.85 g/cm^3) in 1% w/w agarose as a function of inlet pressure decreasing from top to bottom (150, 125, 100, 75 psi) for the following instrument parameters: z_a = 10 mm, 3 orifice discs with 200 μm diameter orifice size. Only particles with d/D_p between 1.5 and 10 are shown. Particles were binned by their diameter in 2 μm intervals and their relative probability density is shown on the color bar. Results from n = 3 replicates are pooled.

standoff distance studies, larger particles tended to penetrate deeper into the gels. This trend was evident despite varying the inlet pressure from 75, 100, 125, and 150 psi.

One important factor to limiting inlet pressures to below 150 psi was the capacity of our gas diversion unit to successfully divert all the exit gas. At inlet pressures above 150 psi, exit gas began escaping through the third orifice disc, which would negate any clinical benefit our device brings.

Higher inlet pressures may allow an increase in force to remove of the particles from the cartridges. Because we were unable to readily quantify the loading of each particle and the particles that remained on the cartridge, this cannot be verified and will be studied in the future.

Orifice size controls number of particles delivered and amount of exit gas

The probability density graphs in Figure 2.21 reveal that there is a slight increase in penetration depth as the orifice diameter is increased. The trend that larger particles end up in deeper parts of the agarose gel persists.

As discussed earlier, the first orifice disc primarily reduces the speed of the carrier gas that leaves the inner capillary tube. The second disc is to further reduce the speed by creating a small space between the first two orifice discs and applying vacuum into that space. Finally, the third disc is to completely eliminate the remaining carrier gas. As the orifice size increases from 200 to 300 µm, the amount of particles delivered into the sample greatly increased. As we examined the SEM images of the particles (Figure 2.11 and Figure 2.12), a number of the particles appeared to be clustered together. We theorize that some of these clusters travel along the ICT as a larger unit and only when they enter the tissue, they break up and appear as individual particles. This might explain why small particles individually would decelerate in ambient air rather quickly, but when they act as one larger particle,

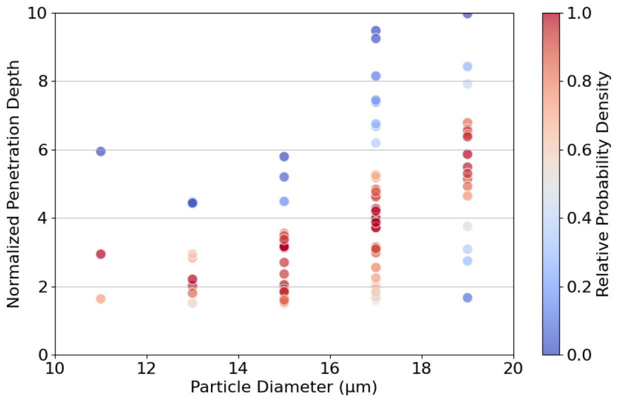

(a) Three orifice discs of 200 µm diameter

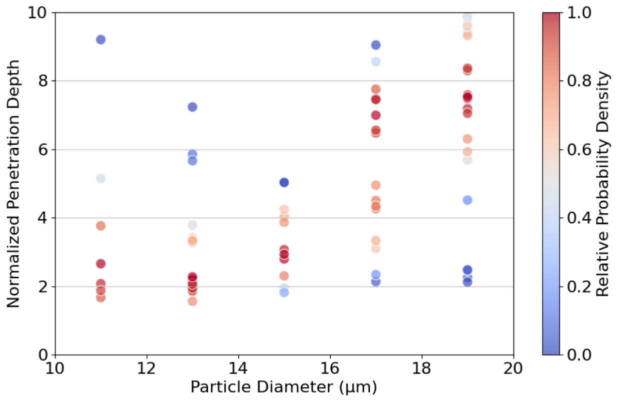

(b) Three orifice discs of 250 µm diameter

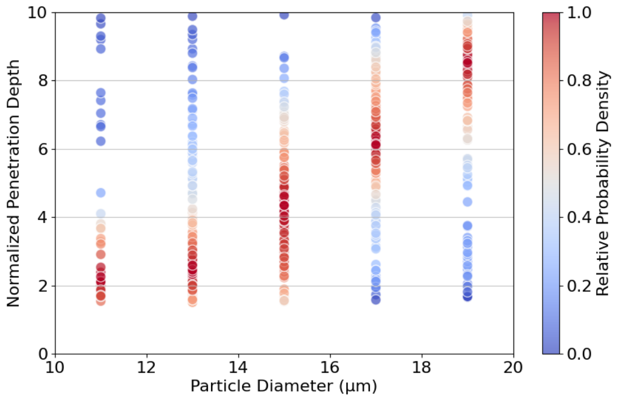

(c) Three orifice discs of 300 µm diameter

Figure 2.21: Distribution of normalized penetration depth d/D_p, for soda lime glass particles ($\rho_p = 2.85$ g/cm^3) in 1% w/w agarose as a function of orifice sizes increasing from top to bottom (200, 250, 300 µm) for the following instrument parameters: z_a = 10 mm, 3 orifice discs with 200 µm diameter orifice size. Only particles with d/D_p between 1.5 and 10 are shown. Particles were binned by their diameter in 2 µm intervals and their relative probability density is shown on the color bar.

they readily keep their momentum as they enter the target. When the orifice size is increased, it allows for more of these clusters to pass through the three orifice discs. In the case of tungsten particles that we examine below, since they nominally are denoted as 20 µm particles, but cluster as much larger particles, these clusters are blocked from even exiting the ICT when the orifice disc is too small. When we enlarge the orifice disc, more meaningful numbers of particles are allowed to pass through into the target.

For 400 µm, the amount of exit gas detected was no longer negligible at high inlet pressures.

Density increase needed to achieve depths for clinical relevance

This section of the study aims to ascertain the necessary density increase in particles to achieve penetration depths relevant for clinical applications. We utilized soda lime glass particles to explore the impact of various parameters on their penetration depth in agarose gels. This choice was informed by the fact that porcine corneas, used in *ex vivo* testing in subsequent chapters, have an epithelium thickness of approximately 70 microns.

While acknowledging that agarose is not an exact substitute for corneal tissue, we highlight its benefits as a surrogate. Agarose gels are transparent, facilitating ease of imaging. Additionally, previous studies, notably by the Groisman lab, have employed agarose as a target material in ballistic testing. Its ease of preparation and consistency, coupled with relative insensitivity to local environmental conditions, make it an ideal choice for our experiments.

Focusing on the penetration capabilities of soda lime glass microparticles in agarose, we noted that although they demonstrate significant penetration, a loss in penetration efficiency is anticipated when transitioning to corneal tissue. This necessitates a deeper understanding of the relationship between particle density and penetration

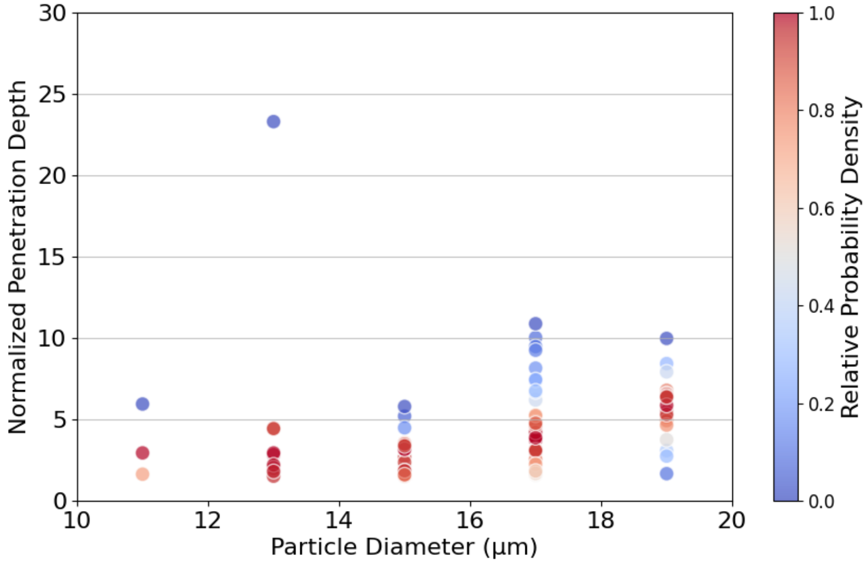

(a) Distribution of soda lime glass particles (ρ_p = 2.85 g/cm^3)

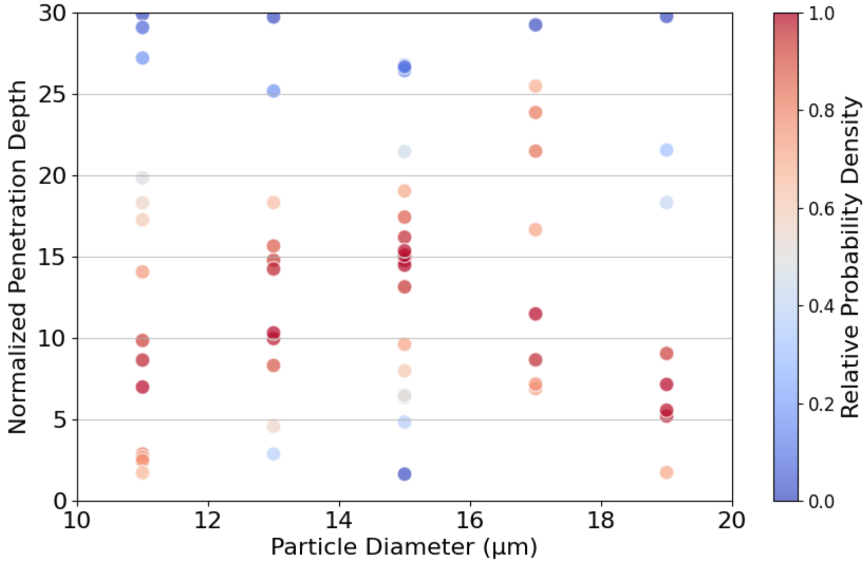

(b) Distribution of tungsten particles (ρ_p = 19.3 g/cm^3)

Figure 2.22: Distribution of normalized penetration depth, d/D_p, for soda lime glass (a) and tungsten (b) particles, which were delivered into 1% w/w agarose gel using inlet pressure, p_i = 125 psi (862 kPa), standoff distance, z_a = 10 mm, and orifice discs denoted in the subcaption. Only particles with d/D_p between 1.5 and 30 are shown. Particles were binned by their diameter in 2 µm intervals and their relative probability density is shown on the color bar.

depth. Our objective is to identify suitable particles for delivery into the cornea in both *ex vivo* and *in vivo* settings.

This study examined depositing microparticles of soda lime glass and tungsten onto cartridges, which were then delivered with inlet pressure, p_i, of 125 psi, standoff distance, z_a of 10 mm, and with three orifice discs into 1% agarose gels. We quantified the penetration of these particles (normalized depth of 1.5 or greater) and categorized them based on their diameters, as illustrated in Figure 2.22. The results for soda lime glass particles mirrored earlier findings regarding standoff distance, where particles with diameters ranging from 16–20 µm exhibited deeper penetration into the agarose gels, surpassing the epithelium threshold consistently.

In contrast, tungsten particles (with a density of 19.3 g/cm³) showed a marked increase in penetration across all examined diameters. Particularly in the 14–16 µm range, penetration depths reached nearly 15 diameters into the agarose gel, translating to approximately 225 microns. However, tungsten particles in the higher diameter range (18–20 µm) demonstrated reduced penetration compared to those in the 14–16 µm range, likely due to the difficulty in accelerating larger, denser particles to the required speed.

Referring back to the predicted penetration depth based on our model (Table 2.4), we expected tungsten particles to decrease in normalized penetration depth as the diameter size is increased. The penetration profile for tungsten particles (Figure 2.22) reveals two trends. First, as the particle size increases from 10–16 µm, the penetration depth increases contrary to our model. However, this behaves in accordance to all the studies of soda lime glass particles which suggest that the particle diameter has little effect on normalized penetration depth, or shows an upwards linear trend. As the particle sizes increase beyond 16 µm, the normalized penetration depth decreases. As our model predicted, although larger particles carry more penetrating power in the material they are entering, they also do not reach high speeds in the ICT. For a density such as tungsten, most if not all, the particle sizes retain their exit velocity fairly well ($\frac{v_i}{v_e} > 0.89$).

In contrast, with soda lime glass particles, the opposite trend holds. Particles ranging from 10–16 µm appear to reach a very similar penetration depth. However, particles larger than 16 µm, were found at greater depths, suggesting they reached the target at higher velocities than the smaller ones. Taking one step back, this suggests the smaller particles either decelerated much faster in the stagnant air, because the alternative hypothesis that the larger particles accelerated to higher velocities as compared to the smaller ones is very unlikely. (Recall, in a normalized penetration depth vs. diameter plot if the impact velocity was the same and if penetration depth was proportional to diameter, the normalized penetration depth would show a horizontal line.)

2.9 Conclusion

This chapter presents the design of new particle delivery apparatus to study the effects of the configuration the gas diversion that protects tissue from the carrier gas. The device was successfully used to characterize the effects of the standoff distance, the inlet pressure, the number of orifice discs and the diameter of the orifice in each disc. The results reveal some surprising features that do not agree with expectations for particle acceleration and deceleration (e.g., Figure 2.20). Future research to discover the origin of discrepancies could include quantitative measurements of particle velocities as they leave the delivery device and as the slow moving through stagnant air. The experiments also show features that accord with expectations for acceleration and deceleration (e.g., Figure 2.22). The ability to achieve significant penetration in the hydrogel for both particles of density 2.85 and 19.3 g/cm^3 guides the selection of delivery parameters to test in corneas *ex vivo*. Specifically, we choose a standoff distance of 10 mm: clinically, variations in the distance between the exit orifice of a delivery device and the position of the cornea's anterior surface could occur, and this chapter shows that delivery is consistent over a +/-25% range in standoff distance about 10 mm. We choose an inlet pressure of 125 psi, based on its ability to consistently strip particles from the cartridge. And we chose to use a configuration with three orifice discs with orifice diameter of 200 µm for soda lime glass and 300 µm for tungsten, based on the number of particles delivered and their ability to still eliminate the exit gas. These parameters are next examined for delivery of particles to porcine corneas *ex vivo*.

2.10 Supplemental information

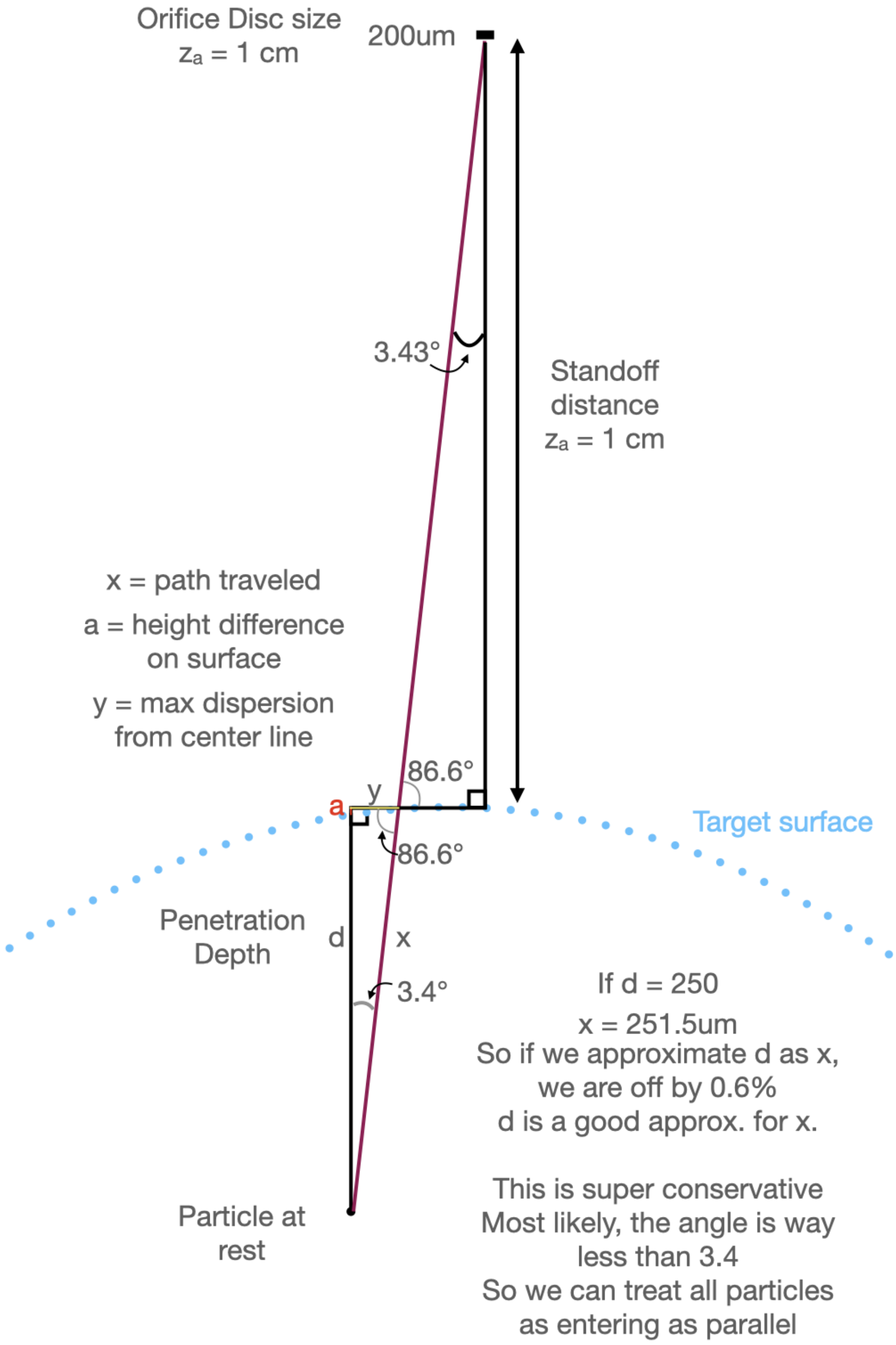

Figure 2.23: Calculations showing particles travel towards target in a collimated pattern.

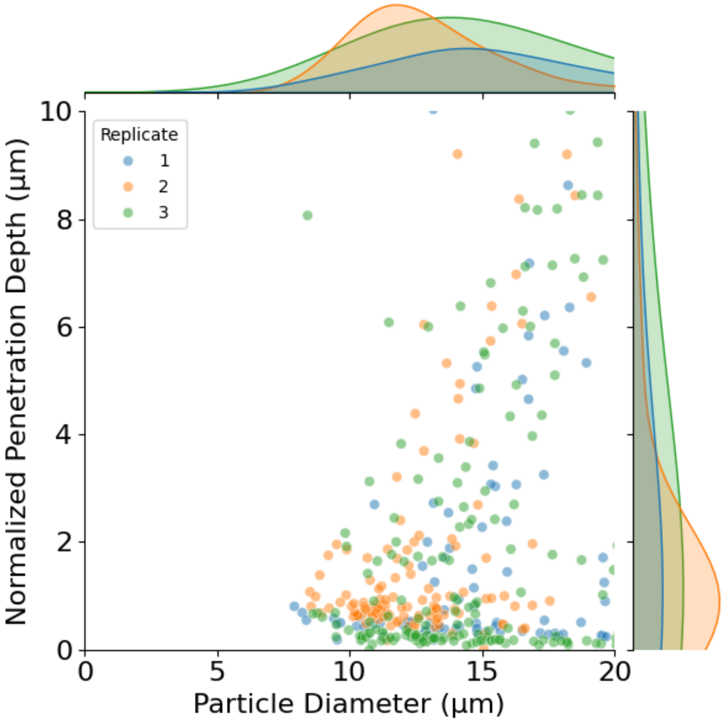

Figure 2.24: Distribution of soda lime glass particles (ρ_p = 2.85 g/cm^3) in 1% w/w agarose at a standoff distance of 5 mm.

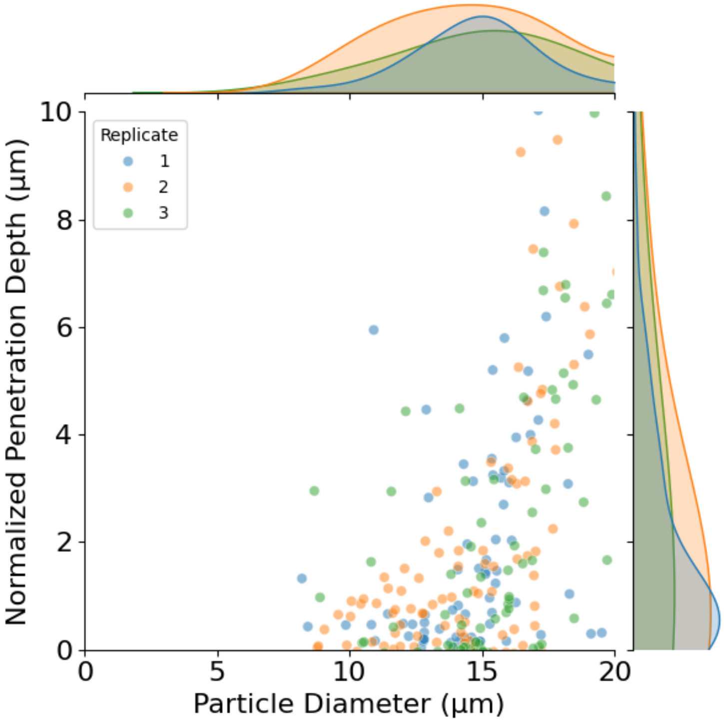

Figure 2.25: Distribution of soda lime glass particles (ρ_p = 2.85 g/cm^3) in 1% w/w agarose at a standoff distance of 10 mm.

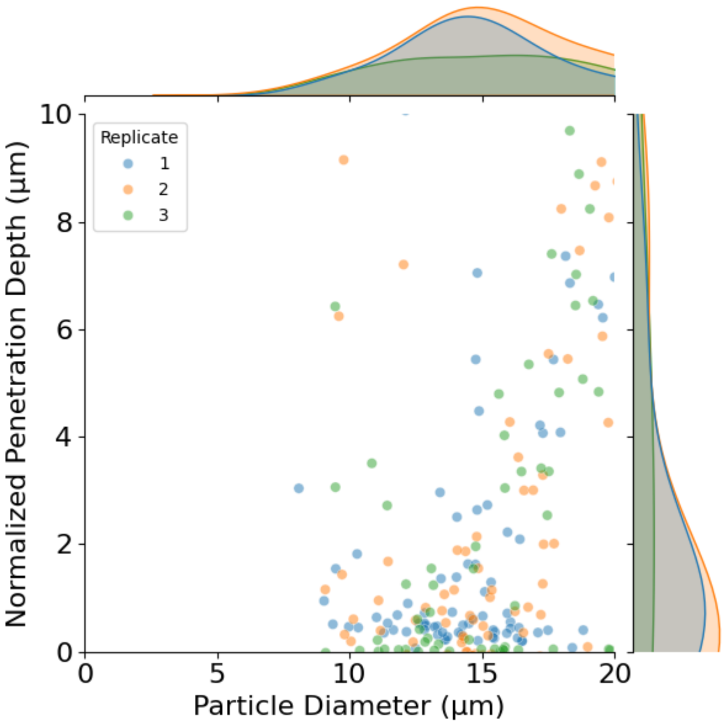

Figure 2.26: Distribution of soda lime glass particles (ρ_p = 2.85 g/cm^3) in 1% w/w agarose at a standoff distance of 12.5 mm.

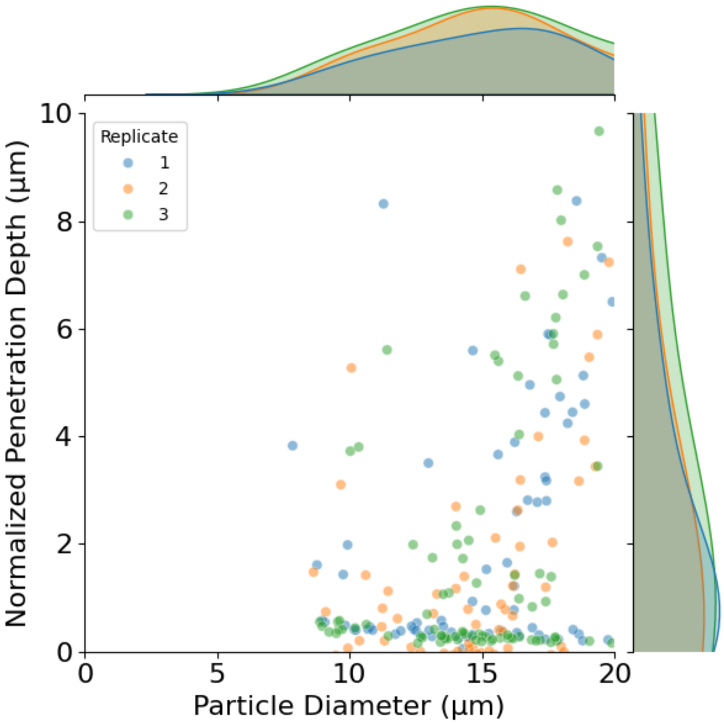

Figure 2.27: Distribution of soda lime glass particles (ρ_p = 2.85 g/cm^3) in 1% w/w agarose at a standoff distance of 15 mm.

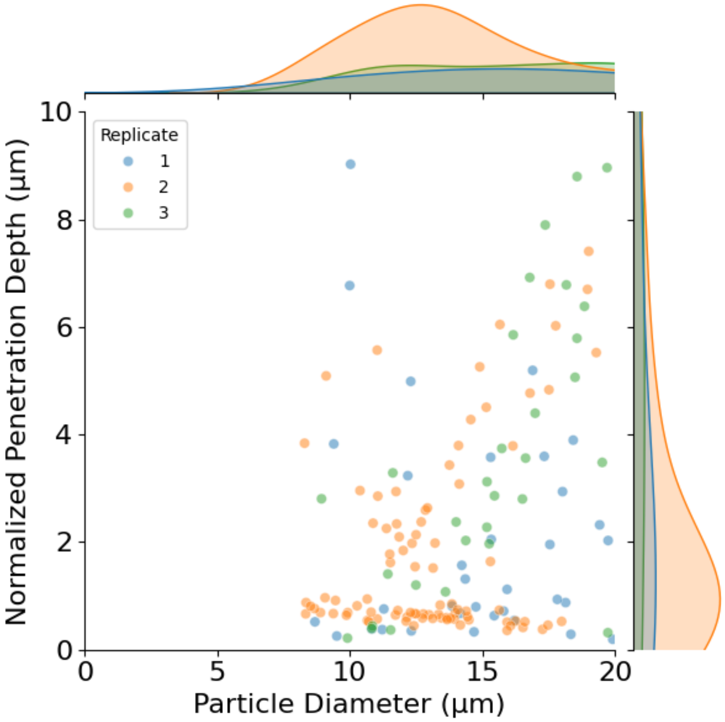

Figure 2.28: Distribution of soda lime glass particles (ρ_p = 2.85 g/cm^3) in 1% w/w agarose at a inlet pressure of 75 psi.

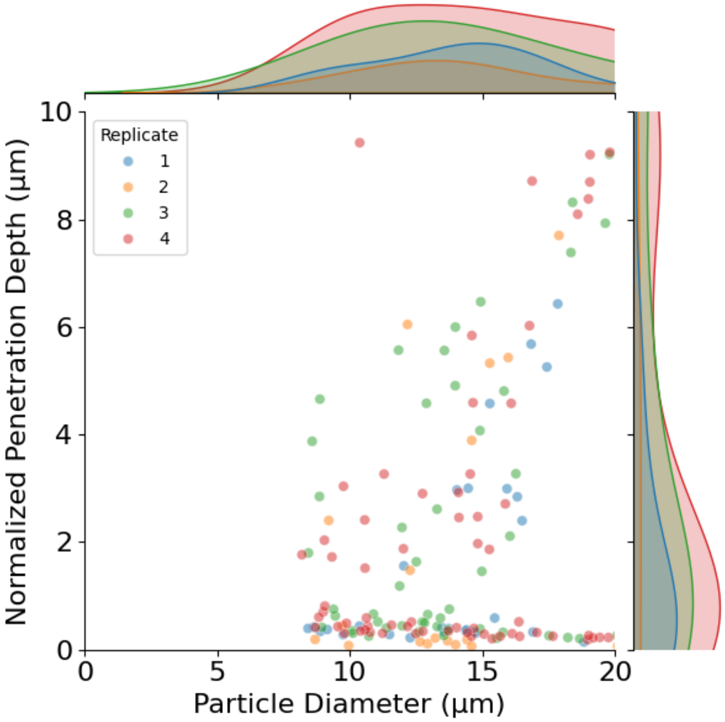

Figure 2.29: Distribution of soda lime glass particles (ρ_p = 2.85 g/cm^3) in 1% w/w agarose at a inlet pressure of 100 psi.

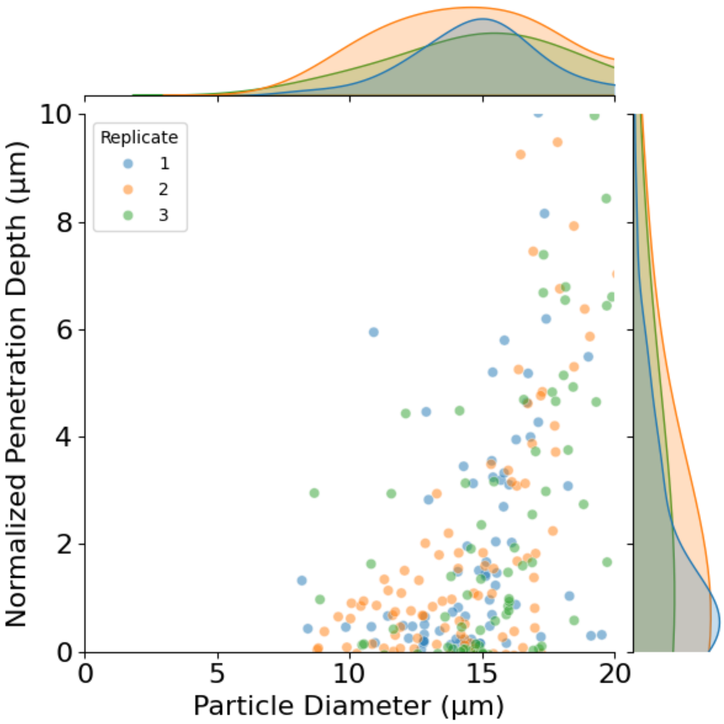

Figure 2.30: Distribution of soda lime glass particles (ρ_p = 2.85 g/cm^3) in 1% w/w agarose at a inlet pressure of 125 psi.

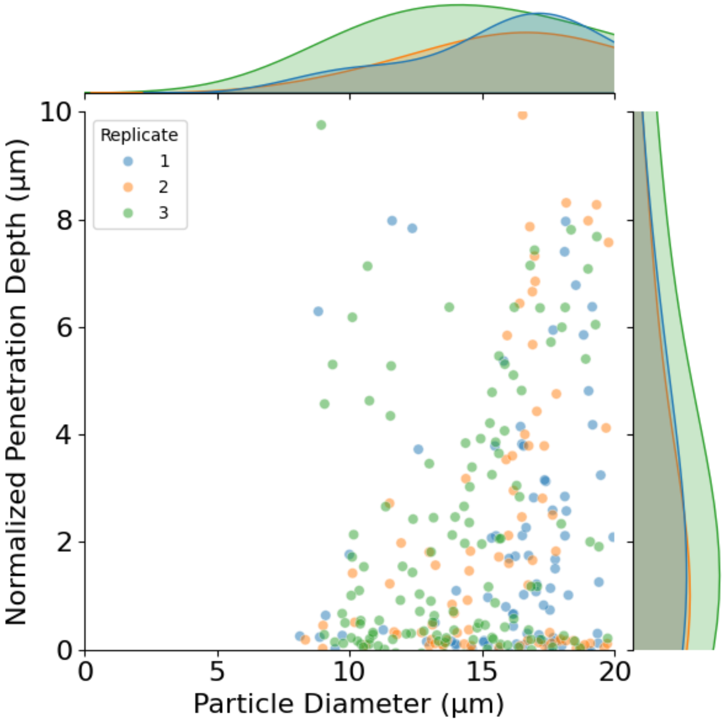

Figure 2.31: Distribution of soda lime glass particles (ρ_p = 2.85 g/cm^3) in 1% w/w agarose at a inlet pressure of 150 psi.

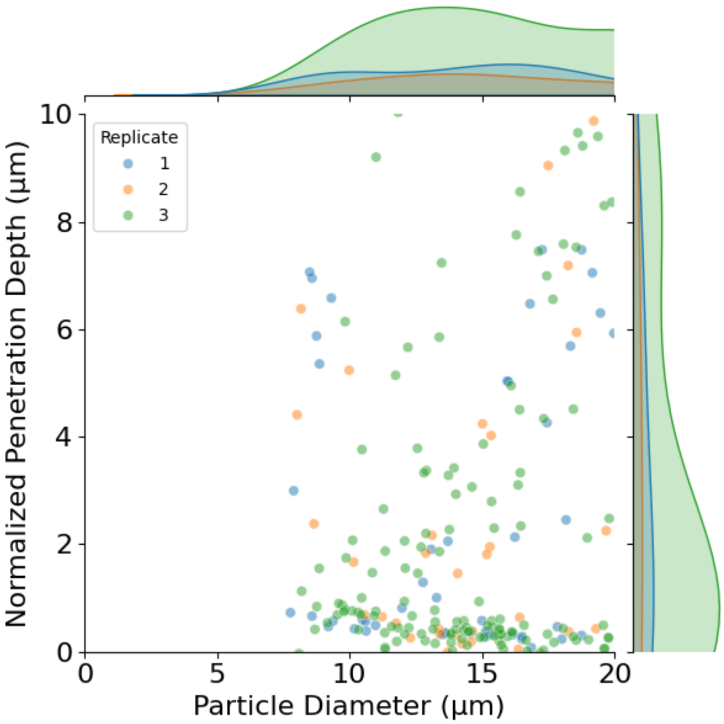

Figure 2.32: Distribution of soda lime glass particles (ρ_p = 2.85 g/cm^3) in 1% w/w agarose with orifice diameter of 250 μm.

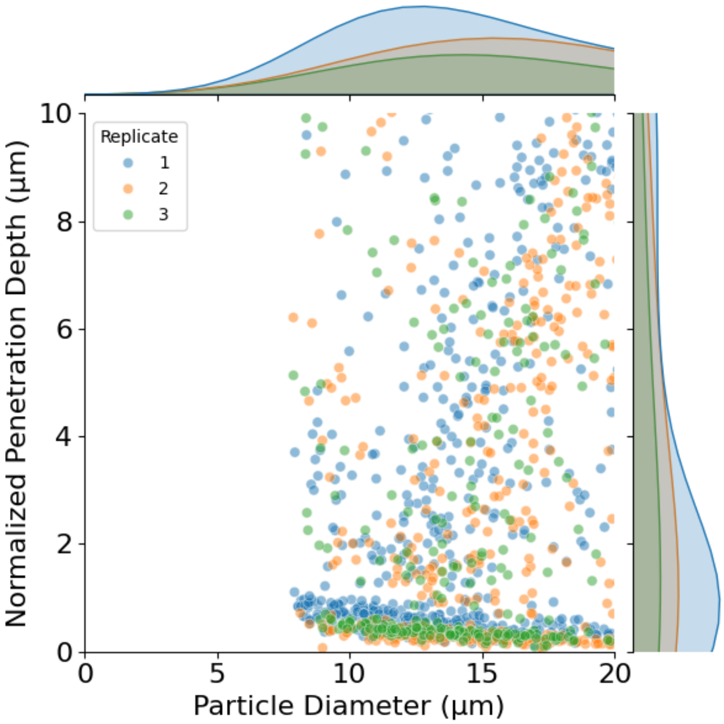

Figure 2.33: Distribution of soda lime glass particles (ρ_p = 2.85 g/cm^3) in 1% w/w agarose with orifice diameter of 300 μm.

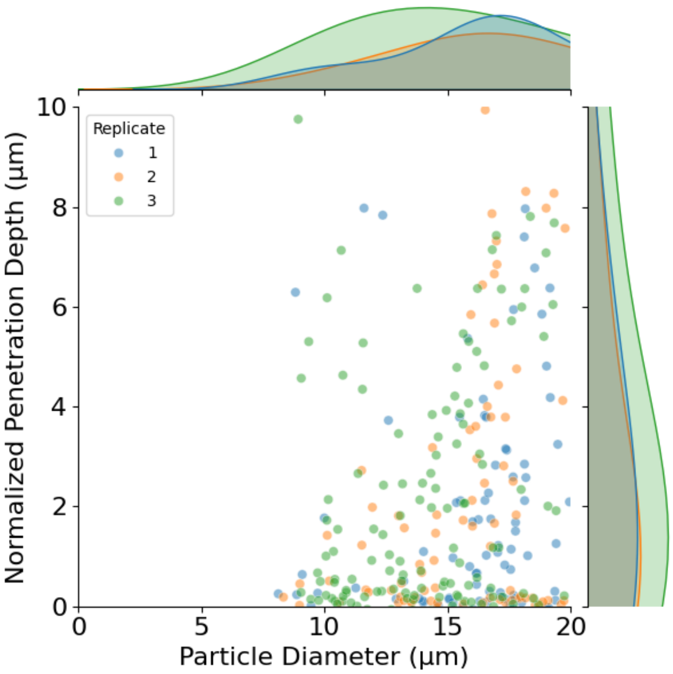

Figure 2.34: Distribution of soda lime glass particles (ρ_p = 2.85 g/cm^3) in 1% w/w agarose with three orifice discs and diameter of 200 µm.

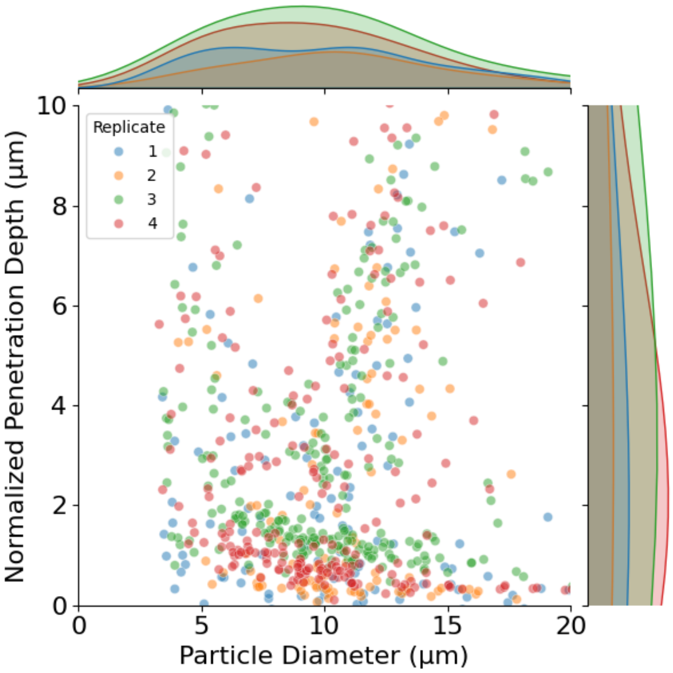

Figure 2.35: Distribution of soda lime glass particles (ρ_p = 2.85 g/cm^3) in 1% w/w agarose with two orifice discs and diameter of 200 µm.

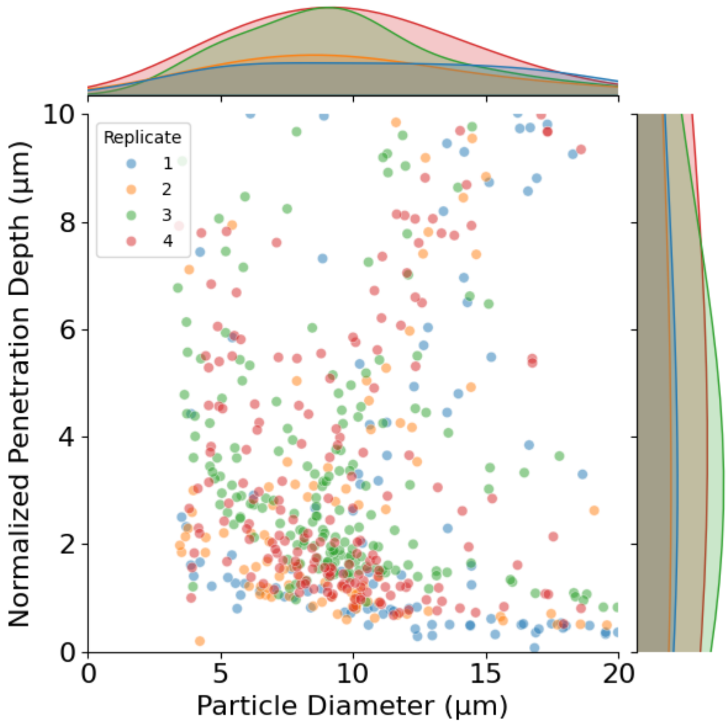

Figure 2.36: Distribution of soda lime glass particles (ρ_p = 2.85 g/cm^3) in 1% w/w agarose with three orifice discs and diameter of 300 µm.

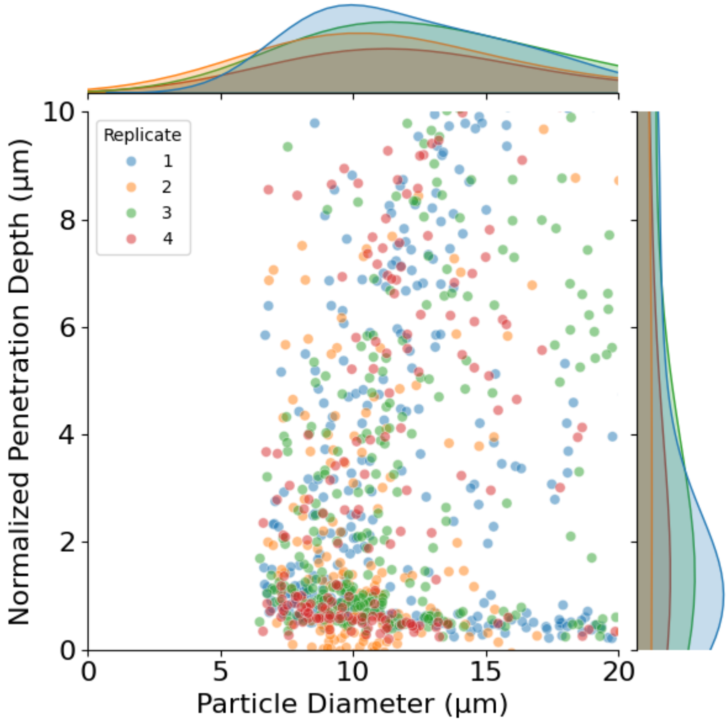

Figure 2.37: Distribution of soda lime glass particles (ρ_p = 2.85 g/cm^3) in 1% w/w agarose with two orifice discs and diameter of 300 µm.

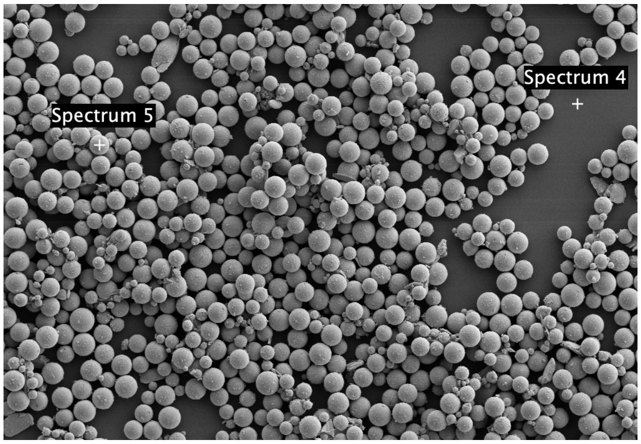

(a) Scanning electron micrograph of soda lime glass particles

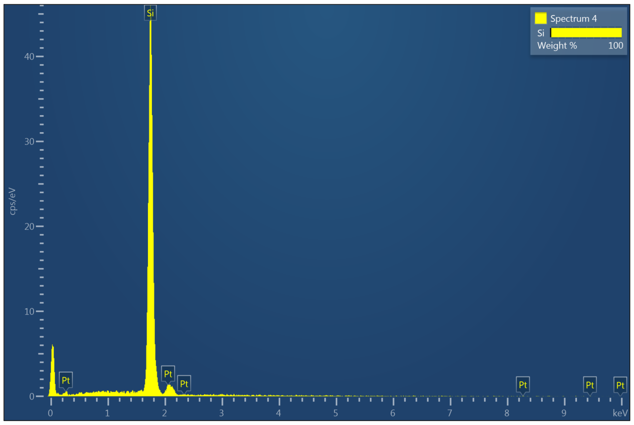

(b) Spectrum 4

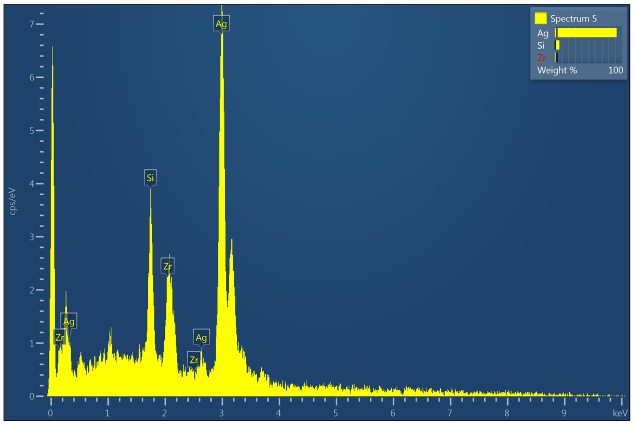

(c) Spectrum 5

Figure 2.38: Scanning electron micrograph of silver coated soda lime glass particles casted onto silicon wafer and corresponding electron dispersive spectroscopy spectra. Spectrum 4 shows high counts of silicon from a point on the wafer. Spectrum 5 shows counts of silver, silicon and platinum from a point on the particle. Magnification = 200x, EHT = 10 kV.

References

[1] D. Bauer et al. “Immunomodulation by topical particle-mediated administration of cytokine plasmid DNA suppresses herpetic stromal keratitis without impairment of antiviral defense”. In: *Graefe’s Archive for Clinical and Experimental Ophthalmology* 244 (2006), pp. 216–225.

[2] D. Bauer et al. “Particle-mediated administration of plasmid DNA on corneas of BALB/c mice”. In: *Biolistic DNA Delivery: Methods and Protocols* (2013), pp. 215–220.

[3] M. Uchida et al. “Transfection by particle bombardment: delivery of plasmid DNA into mammalian cells using gene gun”. In: *Biochim Biophys Acta* 1790.8 (Aug. 2009), pp. 754–64. ISSN: 0006-3002 (Print) 0006-3002 (Linking). DOI: `10.1016/j.bbagen.2009.05.013`.

[4] D. W. Zhang, D. B. Das, and C. D. Rielly. “Microneedle assisted microparticle delivery by gene guns: Mathematical model formulation and experimental verification”. English. In: *Chemical Engineering Science* 125 (Mar. 2015), pp. 176–190. ISSN: 0009-2509. DOI: `10.1016/j.ces.2014.06.031`.

[5] J. C. Sanford. “The development of the biolistic process”. English. In: *In Vitro Cellular & Developmental Biology-Plant* 36.5 (Oct. 2000), pp. 303–308. ISSN: 1054-5476. DOI: `DOI10.1007/s11627-000-0056-9`.

[6] E. Helenius et al. “Gene delivery into intact plants using the Helios TM Gene Gun”. In: *Plant Molecular Biology Reporter* 18.3 (2000), pp. 287–288. ISSN: 0735-9640.

[7] Y. Yoshida et al. “Introduction of DNA into rat liver with a hand-held gene gun: distribution of the expressed enzyme, [32P]DNA, and Ca2+ flux”. In: *Biochem Biophys Res Commun* 234.3 (May 1997), pp. 695–700. ISSN: 0006-291X (Print) 0006-291X (Linking). DOI: `10.1006/bbrc.1997.6682`.

[8] D. Rinberg, C. Simonnet, and A. Groisman. “Pneumatic capillary gun for ballistic delivery of microparticles”. In: *Applied Physics Letters* 87.1 (2005), p. 014103. ISSN: 0003-6951.

[9] A. Groisman, C. Simonnet, and D. Rinberg. *Pneumatic capillary gun for ballistic delivery of microscopic particles into tissue*. 2011.

[10] O. Shefi et al. “Microtargeted gene silencing and ectopic expression in live embryos using biolistic delivery with a pneumatic capillary gun”. In: *Journal of Neuroscience* 26.23 (June 2006), pp. 6119–23. ISSN: 1529-2401 (Electronic) 0270-6474 (Linking). DOI: `10.1523/JNEUROSCI.1237-06.2006`.

[11] M. A. Saad. *Compressible Fluid Flow*. Prentice-Hall, 1985. ISBN: 978-0-13-163486-2.

[12] G. Rudinger. *Fundamentals of Gas-Particle Flow*. Vol. 2. Amsterdam, The Netherlands: Elsevier Scientific Publishing Company, 1980.

[13] R. C. Flagan and J. H. Seinfeld. *Fundamentals of air pollution engineering*. Courier Corporation, 2012. ISBN: 0-486-48872-1.

[14] J. Dehn. "A unified theory of penetration". In: *International journal of impact engineering* 5.1-4 (1987), pp. 239–248. ISSN: 0734-743X.

[15] M. Kendall et al. "Effects of relative humidity and ambient temperature on the ballistic delivery of micro-particles to excised porcine skin". In: *J Invest Dermatol* 122.3 (Mar. 2004), pp. 739–46. ISSN: 0022-202X (Print) 0022-202X (Linking). DOI: `10.1111/j.0022-202X.2004.22320.x`.

[16] Y. Liu and M. A. F. Kendall. "Numerical analysis of gas and micro-particle interactions in a hand-held shock-tube device". English. In: *Biomedical Microdevices* 8.4 (Dec. 2006), pp. 341–351. ISSN: 1387-2176. DOI: `10.1007/s10544-006-9596-z`.

[17] M. A. F. Kendall. "The delivery of particulate vaccines and drugs to human skin with a practical, hand-held shock tube-based system". In: *Shock Waves* 12.1 (2002), pp. 23–30. ISSN: 1432-2153. DOI: `10.1007/s001930200126`.

[18] T. J. Mitchell, M. A. Kendall, and B. J. Bellhouse. "A ballistic study of micro-particle penetration to the oral mucosa". In: *International journal of impact engineering* 28.6 (2003), pp. 581–599. ISSN: 0734-743X.

[19] J. X. Xia et al. "Evaluation of biolistic gene transfer methods in vivo using non-invasive bioluminescent imaging techniques". English. In: *Bmc Biotechnology* 11 (June 2011). ISSN: 1472-6750. DOI: `Artn6210.1186/1472-6750-11-62`.

Chapter 3

BIOLISTIC DELIVERY OF MICROPARTICLES INTO THE CORNEA

3.1 Introduction

When one thinks of particles entering the cornea, the first thing that comes to mind is injury. Literature reflects this concern. Some particle-induced corneal injuries result accidentally (e.g., wind borne seeds[1] and sand,[2] or particles accelerated by compressed gas, such as “silly string”).[3,4] Other particle-induced corneal injuries result from attacks, typically involving large (> 4 mm) ballistic objects[5], with particular attention to those that penetrate through the entire thickness of the cornea.[6] Scant attention has been given to the possibility of using particle delivery to the cornea for therapeutic purposes, which is the focus of the present work.

For therapeutic uses, such as drug delivery, particle sizes that are small enough that they would not be perceived visually by the patient or an observer ($\leq$ 30 µm) and large enough that a modest number ($\leq$ 1000 µm) can deliver a therapeutically-relevant dose of drug (> 5 µm for two examples discussed below). From the literature on accidental penetration of particles in the eye, as a study examined mechanisms of corneal injuries to farmworkers toiling in high winds extended to particles as small as 20 microns;[1] they found that particle sizes below 500 microns rarely produced injuries to Bowman’s layer, the basement membrane of the corneal epithelium. However, we were unable to find information relevant to the therapeutic use of find particles, such as their penetration depths, their consequences for epithelial barrier function, or for the refractive surface of the cornea.

While prior literature studied a variety of corneal injuries due to small airborne particles such as mustard seed, silly string, sand, etc. Clinical studies typically evaluated subjects based on ocular function (e.g., the presence of corneal haze viewed through a slit lamp or whether globe rupture occurs) and pain tolerance as opposed to detailing fine details of penetration such as what size the particles are and where they reside in the cornea. Prior research has focused on the wounds caused by large (> 4 mm) ballistics and their effects on the eye, with particular attention to whether there is globe rupture (i.e., one or more particles penetrating through the entire thickness of the cornea).

There exists no literature on the effects specific to each layer of the cornea such as the stroma and epithelium of the cornea. Using animal tissue *ex vivo* (guinea pig), two relevant studies investigate wind-borne onion particles and soil particles relevant to harvesting and found that for particle diameter approximately 25.9±1.75 μm, the threshold wind speed for injury was 7 m/s.[1] When eyes were exposed to particles of a specific size (20–500 μm and 1.5 mm and 3.0 mm), they were examined via slit-lamp microscopy with 2% w/v fluorescein solution and graded for corneal injury. They found that particle size is a stronger determinant of corneal injuries than wind speed; larger onion skin flakes (1.5 mm and 3.0 mm) produced higher rates of corneal injuries due to Bowman's layer injury and smaller particles (up to 500 μm) had a 3% rate of severe corneal injury.

This presents an opportunity for us to use our delivery device to deliver therapeutic particles into the cornea. Small particles below 100 μm are of particular importance because they are less likely to cause severe corneal injuries and previous studies in keratoconus demonstrated relatively few particles in the stromal layer were required for clinical response. If the particles remain in the stroma for long period of time, it may even serve as a drug depot that slowly releases drug over time.

The current state of technology on these delivery devices of particles to the cornea include both devices from Bio-Rad, the Helios gene gun and the PDS-1000. Our group has done work with the PDS-1000,[7] and while it does offer delivery of high-speed particles, it also requires the target to be placed in a vacuum chamber. Bauer,[8] for example, has used the Helios gene gun to deliver 1 μm gold particles into the epithelium and the anterior portions of the stroma. The Helios gene gun also uses upwards of 700 psi of helium gas to propel particles into the tissue, none of which is fully diverted away. A significant portion of that exit gas will impact the target and cause some damage.

Although particles successfully reach the epithelium with both the PDS-1000[7] and the Helios gene gun,[9,10,11] both show that the stroma is incredibly difficult to penetrate with significant depth. There exists a dramatic difference in penetration depths achieved in corneal tissue as compared to gels such as agarose. The majority of the particles delivered to the cornea was found either in the epithelium or near the anterior portion of the stroma. This may be due to the inherent properties of the cornea that is unknown so far.

Recall from Chapter 1, the cornea presents several barriers to entry, including the inherent properties of the epithelium and the stroma. On the anterior side of the epithelium exists the aqueous tear film, with a volume around 7–10 μL. Underneath the tear film but on the surface of the epithelium, are cell surface mucins, which prevent pathogens from adhering to the cornea[12,13,14,15]. This mucin layer is considered as a restrictive barrier[16] for entry for topically applied drugs, though it is unclear by what method. In a parallel context, trans-mucosal delivery are prevented by the mucus layer acting as a filter.

Given the challenges that exist, we hypothesized that the limiting factor in delivering particles to the cornea is actually the cornea itself. Although PDS-1000 might offer higher penetration due to increasing particle velocities, the tradeoff to reach such velocities, such as vacuum chamber, exit gas damage, may not even matter to

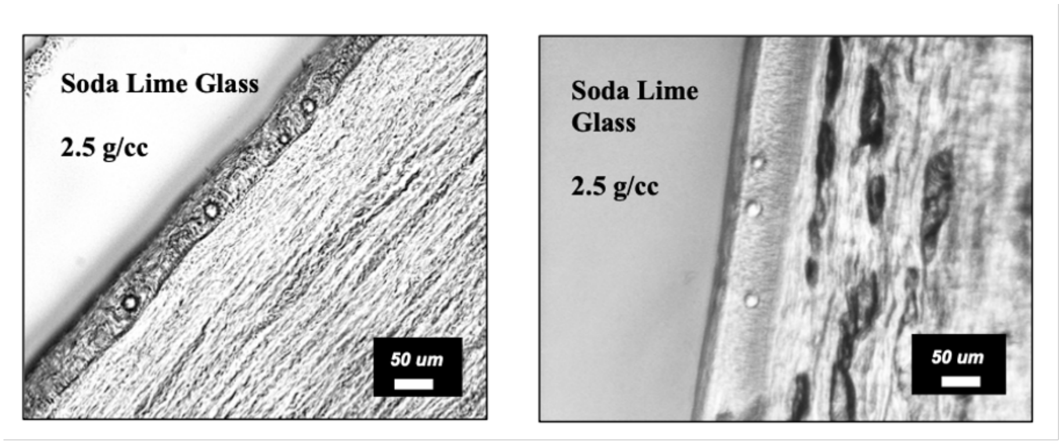

Figure 3.1: Soda lime glass particles (ρ_p = 2.85 g/cm^3) embedded into porcine corneal tissue using the Bio-Rad PDS-1000. Reprinted from Laccetti.

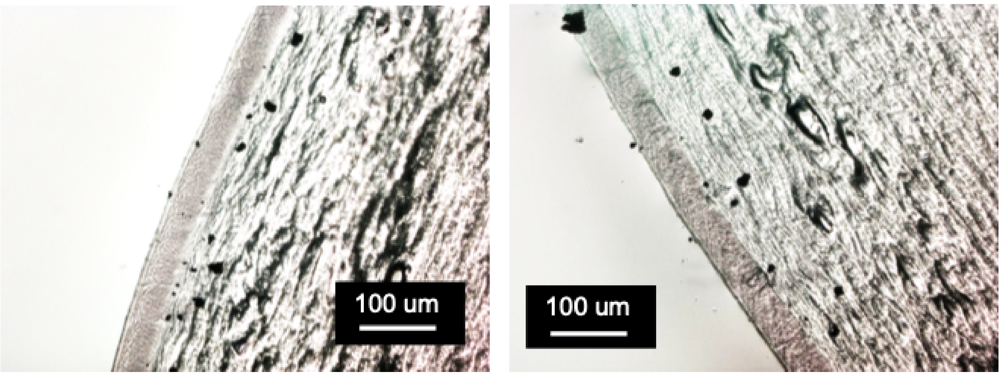

Figure 3.2: Tungsten particles (ρ_p = 19.3 g/cm^3) embedded into porcine corneal tissue using the Bio-Rad PDS-1000. Reprinted from Laccetti.

just enter the cornea, as the ultimate penetration is limited by the material itself. Thus, there is reason to believe that our device can successfully deliver particles to similar depths within the cornea while providing the clinical advantages such as no exit gas flow, use in ambient air, etc.

3.2 Materials and methods

Particle delivery into corneal tissue

Based on our testing with our delivery device in the previous chapter for soda lime glass and tungsten particles in agarose, experiments were done with porcine eyes to evaluate the penetration depths in corneal tissue. Similar to previous work, cartridges were prepared with both soda lime glass and tungsten particles. Each cartridge was prepared with 0.5 µL of 1% w/w soda lime glass particles in ethanol or 1.0 µL of 1% w/w tungsten particles in ethanol. These cartridges were allowed to dry overnight before using. Unless otherwise noted, all deliveries with our device was with –10 psi (–69 kPa) of vacuum.

Preparation of porcine tissue

Sierra for Medical Science supplied porcine eyes from 3–4 month old swine. Excess fat and connective tissue were trimmed off the globes. Eyes were disinfected and stored in tissue culture medium (DMEM/F-12 with 2.5 mM L-glutamine, 120 µg/mL Penicillin, 200 µg/mL Streptomycin sulfate and 5 µg/mL Amphotericin B) for up to 48 hours at 4ºC. The eyes selected are all clear and free of any visible signs of edema.

Epithelial integrity assays

The effect of particle entry into the cornea on its epithelial integrity was examined by looking for the entry of fluorescein stain into the cornea. 2% w/v fluorescein stain was applied immediately after delivery and visualized with blue light to document whether the cornea stains, indicating epithelial failure.

Tissue imaging and particle counting

Immediately after particle delivery, corneas were imaged with optical coherence tomography using a Ganymede 210 Series Spectral Domain OCT imaging System with an OCTP-900 scanner and 8 m later resolution scan lens (Thorlabs, Newton, NJ). Three-dimensional images with pixel sizes of 2.03 µm (x) by 2.03 µm (y) by 2.03 µm (z) were acquired using the medium speed, medium sensitivity of 15 kHz A-scan rate or the low-speed, high sensitivity of 5.5 kHz A-scan rate. Images were exported as a three-dimensional stack of XZ slices. Unlike the previous work with agarose gels, images were processed in Imaris. Since images of the cornea produced a very intense signal, it prevented thresholding to allow for the capture of the particles of interest — signal from the surface would overwhelm the actual particles embedded in the tissue. The "count spots" feature in Imaris was used to identify the surface and the particles. Custom Python code was then used to determine a quadratic fit for the surface of the cornea given the points on the surface. The normal distance from each point to the surface was then determined.

3.3 Results and discussion

Optical coherence tomography images of soda lime glass particles in porcine corneal tissue are shown in Figure 3.3. Most particles on each sample was found on the surface of the cornea. Due to the signal of the OCT from the surface and the particles on the surface, we were unable to determine the exact number of particles that deposit on the surface. However, for soda lime particles with density of 2.85 g/cm^3, we find that all the particles that successfully penetrate the surface fully embed within the epithelium. Each sample shows a range of particles that embed within an approximately 500 micron by 500 micron window in the epithelium.

Due to software limitations with Imaris, we were unable to determine the size of the particle, we could only manually determine the size of the particle using FIJI. OCT images however, show that particles that embed within the cornea were on the larger size (approx. 15 to 20 microns). Smaller particles, similar to the gel, were found closer to the surface. Occasionally, there are smaller particles found at some depth within the epithelium and just like in the agarose gel, we believe that smaller particles cluster with larger particles in flight, and only break apart into separate particles upon impact into the tissue. As with our studies in the agarose gels, smaller particles carry less penetrating power than larger particles, and they also lose their velocity much quicker in stagnant air than larger particles.

Table 3.1: Statistics for penetration into cornea

Particle type	**Density (g/cm^3**	**Average particle size**	**Average number of particles**
Soda lime glass	2.85	18.0 ± 7.4	14.7 ± 4.6
Tungsten	19.3	15.5 ± 5.5	18.0 ± 7.3

One thing to note is that we found much fewer particles that were embedded in the cornea than in the agarose gel. Two reasons may explain this. First, based on our prior knowledge, we expected and saw significant numbers of particles embedded on the cornea surface. The cornea surface reduces much of the particle's penetrating power as compared to the gel. Then, they are imaged along with the cornea surface and we were unable to discern them from the surface. If future improvements in image processing allows us to separate the high signal caused by the anterior cornea surface from the particles that are on it, we would then be able to determine the accurate fraction of particles that actually enter into the epithelium.

Optical coherence tomography images of tungsten particles in porcine corneal tissue are shown in Figure 3.6. We found a distribution of sizes of particles within both the epithelium and the stroma (Table 3.1).

Connecting back to the work done in Chapter 2, tungsten particles with higher densities, carry much more penetrating power than soda lime glass particles would, even as the sizes decrease, explaining this phenomenon. Similar to the work done previously in our group with the PDS-1000, our new device, under clinical settings was able to deliver particles into the stroma and epithelium at much lower inlet pressures (125 vs 1350 psi, 862 kPa vs 9308 kPa) and with no exit gas impacting the tissue.

The shape of tungsten particles is not spherical. Although we did not have the ability to visualize and characterize the shape of the particle and their relationship

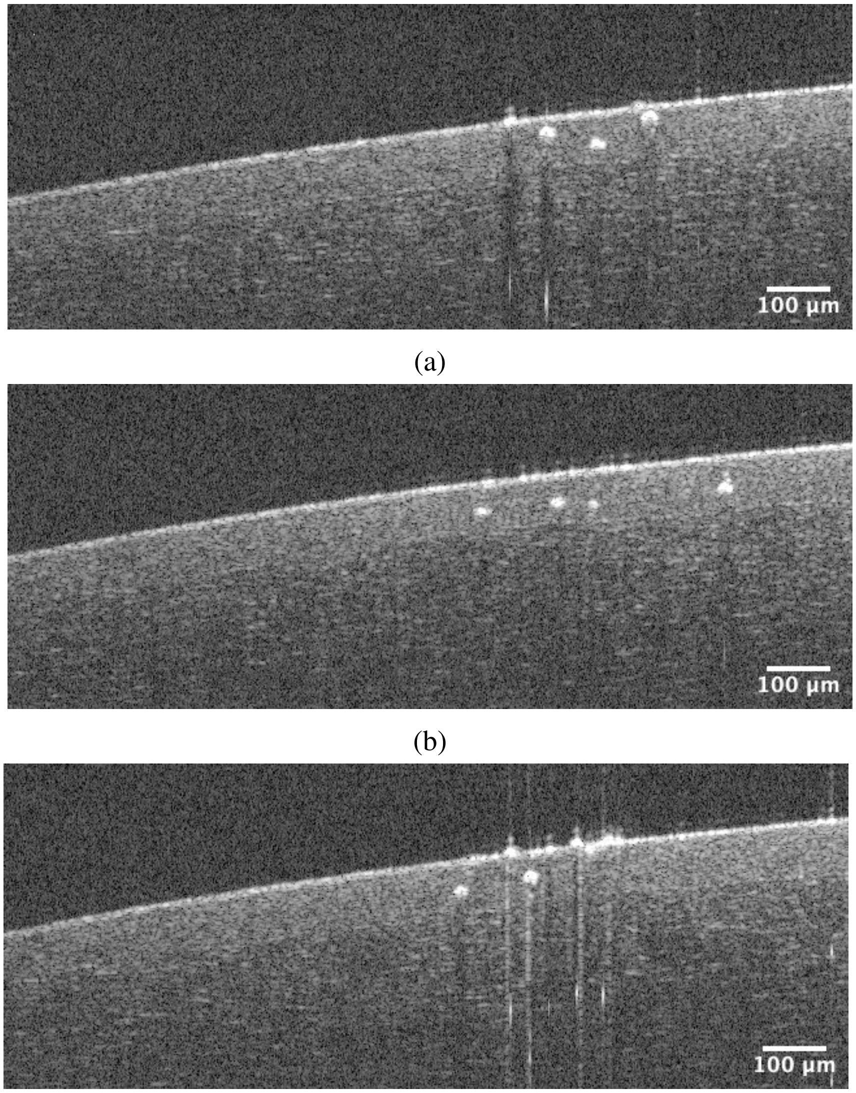

(a)

(b)

(c)

Figure 3.3: Cross sectional view of optical coherence tomography images of silver coated soda lime glass particles (ρ_p = 2.85 g/cm^3) in excised porcine cornea. Images represent three separate X-Z cross sections taken from the same sample. Particles were delivered to the cornea with p_i = 125 psi, z_a = 10 mm, with 3 orifices of 200 µm.

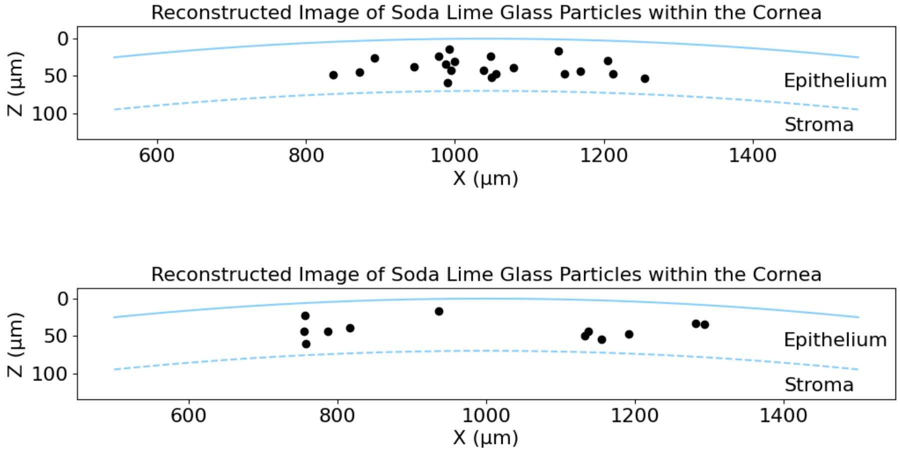

Figure 3.4: Two-dimensional reconstructions of soda lime particles within porcine cornea ($\rho_p = 2.85$ g/cm^3) in excised porcine cornea. Images represent three separate X-Z cross sections taken from the same sample. Particles were delivered to the cornea with p_i = 125 psi, z_a = 10 mm, with 3 orifices of 200 µm.

to penetration, we hypothesize that a particle that might have a sharper end may penetrate deeper into the tissue.

Particle delivery leaves little damage to the cornea

When we applied fluorescein staining and examined the areas where particles were delivered, only at large orifices (e.g., 400 µm) where there was a significant number of particles did we see any significant stanining of the epithelium. Even then, the cornea exhibited the ability to regain its epithelial function after 4 hours.

In delivery with 200 µm orifice discs where there is no exit gas and relatively few particles delivered, when stained with fluorescein, the areas of particles displayed almost no staining. In Figure 3.7, the blue box represents the area where tungsten particles are delivered and the area in red represents where a deliberate wound was created with a 20 gauge needle. Representative OCT images are shown. In the needle wound, OCT images reveal a visible defect in the anterior epithelial surface, whereas in the area with particles, the epithelium remains intact.

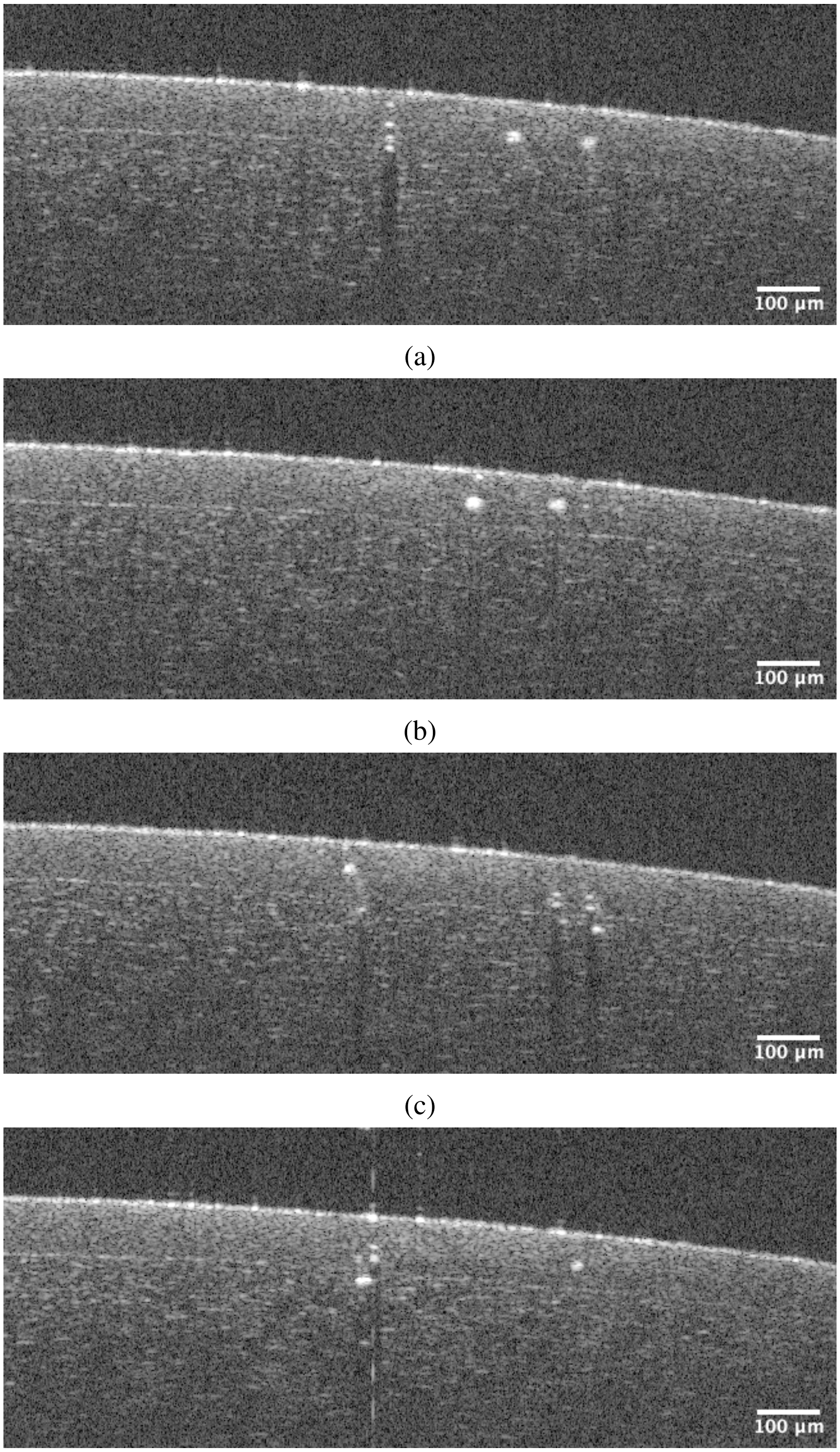

(a)

(b)

(c)

(d)

Figure 3.5: Cross sectional view of optical coherence tomography images of tungsten particles (ρ_p = 19.3 g/cm^3) in excised porcine cornea. Images represent three separate X-Z cross sections taken from the same sample. Particles were delivered to the cornea with p_i = 150 psi, z_a = 10 mm, with 3 orifice discs with 300 µm diameter orifice.

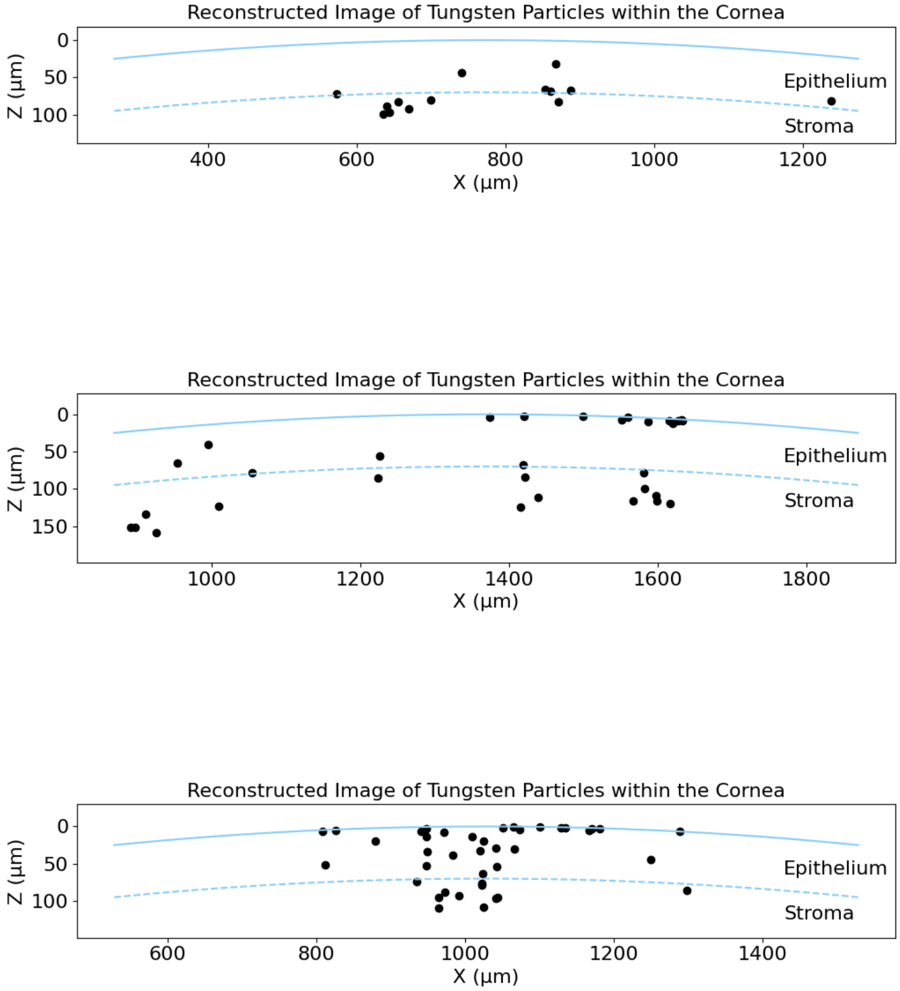

Figure 3.6: Cross sectional view of optical coherence tomography images of tungsten particles (ρ_p = 19.3 g/cm^3) in excised porcine cornea. Images represent three separate X-Z cross sections taken from the same sample. Particles were delivered to the cornea with p_i = 150 psi, z_a = 10 mm, with 3 orifice discs with 300 µm diameter orifice.

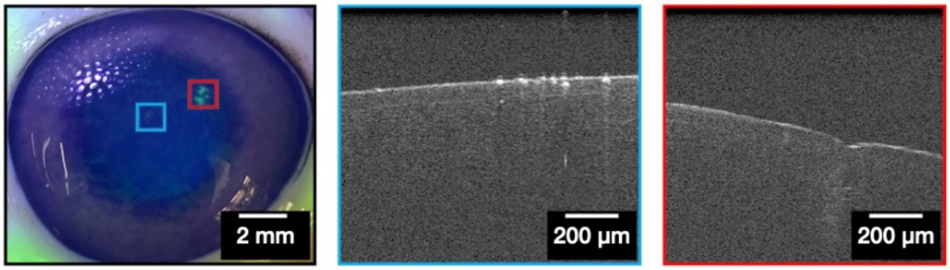

Figure 3.7: A comparison of fluorescein staining on microparticle delivery and deliberate needle wounds in *ex vivo* cornea. The blue square represents an area where microparticles were delivered. The red square represents an area where a 20 gauge needle was applied to deliberately cause an eptheilial defect. OCT images are shown on the right for both scenarios. Note, no defects were visible in OCT for particle delivery, while it was readily apparent for the needle wound.

Examinations of OCT images were done to examine for epithelial defects. Of the numerous samples examined, we could only locate one example where the OCT revealed a visible epithelial defect (Figure 3.8). As seen in Figure 3.8a the diameter of the defect roughly matches the diameter of the particle that came to rest below it ($\sim$ 15 µm).

OCT images were taken at 5 minute intervals until the defect was no longer visible. At 10 minutes, (Figure 3.8b), the size of the defect has reduced in size by roughly 50%. By 30 minutes, the anterior surface of the epithelium appeared continuous and intact (Figure 3.8c). Fluorescein staining was done following 60 minutes of initial particle delivery, and no noticeable staining could be detected on the surface of the cornea. Thus, even in the rare cases that the particle causes damage to the surface of the epithelium, the epithelium's natural properties closes itself within a short period of time and regains its barrier function to the outside environment.

The effect of vacuum on exit gas damage and radial distribution of particle delivery

In studies where the orifice diameter in our orifice discs in the GDU was enlarged to 400 µm, we visualized the soda lime glass particles delivered to the cornea at inlet

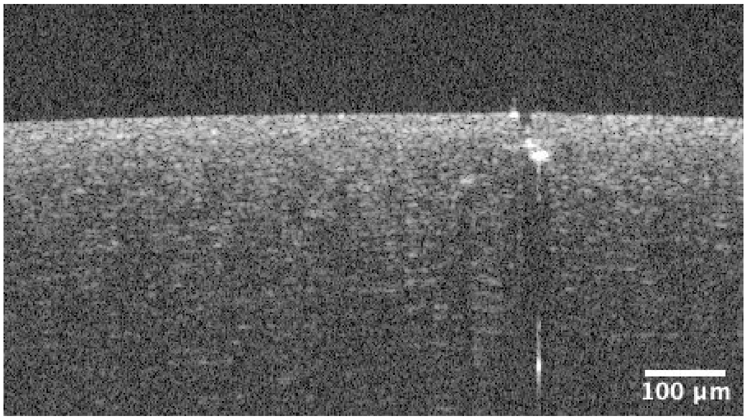

(a) 0 minutes after particle delivery

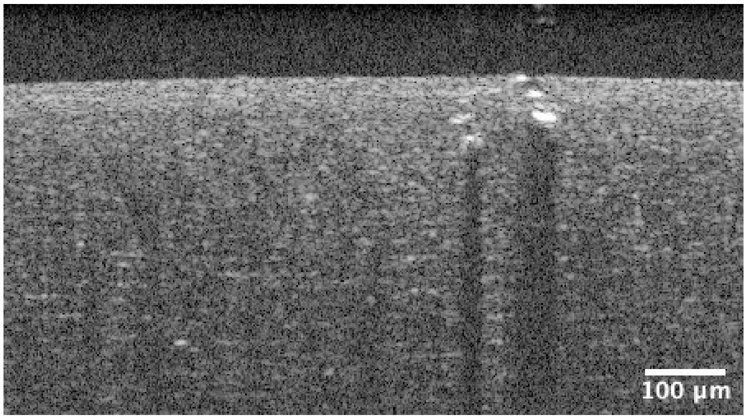

(b) 10 minutes after particle delivery

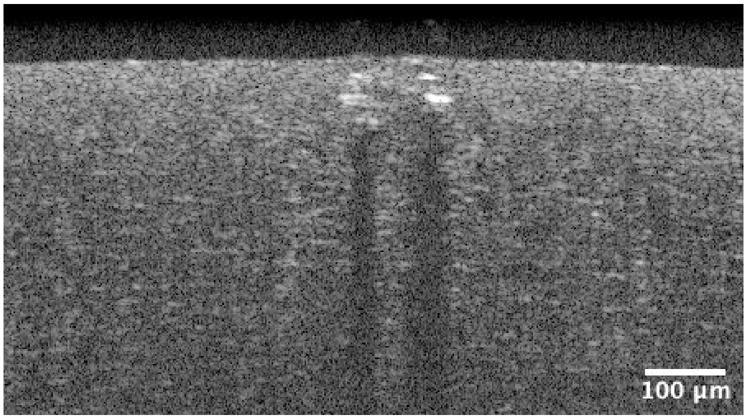

(c) 30 minutes after particle delivery

Figure 3.8: Cross sectional view of optical coherence tomography images of tungsten particles (ρ_p = 19.3 g/cm^3) in excised porcine cornea. Images represent three separate X-Z cross sections taken from the same sample. Particles were delivered to the cornea with p_i = 150 psi, z_a = 10 mm, with 3 orifice discs with 300 μm diameter orifice.

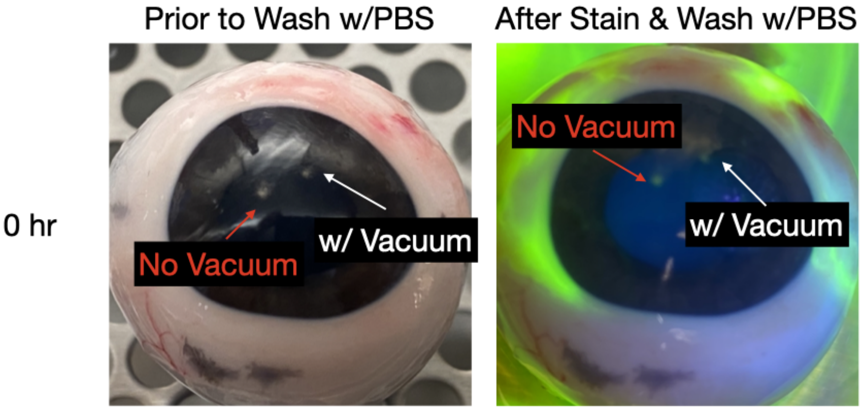

Figure 3.9: Photographs showing the effect of vacuum on the delivery of microparticles into the corneal tissue. Soda lime glass particles ρ_p = 2.85 g/cm$_3$ were delivered into the cornea using the following parameters: inlet pressure, p_i = 125 psi, standoff distance, z_a = 10 mm, three orifice discs of with orifice diameter of 400 µm.

pressure of 125 psi. Particles were readily visible on the cornea (Figure 3.9). In this particular study, we did not use vacuum to divert the exit gas and examined the damage due to the exit gas. The distribution of particles was wider and when stained with fluorescein, produced a larger fluorescence, indicating a greater disruption of the epithelium.

3.4 Conclusion

The studies in this chapter examined the performance of our drug delivery device into *ex vivo* corneal tissue. Previous work into the cornea either used the Helios gene gun (some exit gas) or were done with the PDS-1000 (in vacuum chamber).

Our work here centers around a device that produces zero exit gas and works in ambient pressure.

Even work with the Helios gene gun delivered 1 micron gold particles into the cornea. Using our device, we showed the ability to deliver particles (up to 20 microns) into the epithelium and stroma. An increase of density from soda lime glass particles (ρ_p = 2.85 g/cm^3) to tungsten particles (ρ_p = 19.3 g/cm^3) allowed particles to successfully enter the stroma, due to them having more penetrating power.

These studies into the cornea also proved that these micron sized particles do not cause damage to the cornea. Most of the particles that entered into the cornea did not cause any staining in the epithelium. Inspection of the OCT revealed no discernible tracks left behind in the particle except in a very select few instances. Even in those cases where visible epithelial wounds were detected, we were able to see the cornea close the opening within 30 minutes.

It is interesting that the cornea presents such a challenge for particles to enter. Our device could be tuned to deliver particles into other living materials such as skin.

Clinically, however, it might be important to know the long-term prognosis of the particles that enter. This chapter delves into the performance of our innovative drug delivery device in delivering particles into *ex vivo* corneal tissue, marking a significant advancement over traditional methods like the Helios gene gun and PDS-1000 systems. Our device uniquely operates without exit gas and functions effectively at ambient pressure, a notable deviation from existing approaches.

Contrasting with the Helios gene gun, which delivered 1-micron gold particles into the cornea, our device successfully introduced larger particles (up to 20 microns) into the epithelium and stroma. This was achieved by varying particle density, with a transition from soda lime glass (ρ_p = 2.85 g/cm^3) to denser tungsten particles (ρ_p = 19.3 g/cm^3), enhancing penetration capabilities.

Crucially, our studies confirmed the non-damaging nature of these micron-sized particles to corneal tissues. Most particles caused no staining in the epithelium, and Optical Coherence Tomography (OCT) inspections typically revealed no residual tracks. Notably, even in rare instances of visible epithelial wounds, rapid healing was observed within 30 minutes.

The resistance of the cornea to particle penetration underscores the potential of our device in other biomedical applications, like skin delivery systems. However, understanding the long-term implications of particle presence in tissues remains a vital aspect for future clinical applications, warranting further investigation.

3.5 Supplemental information

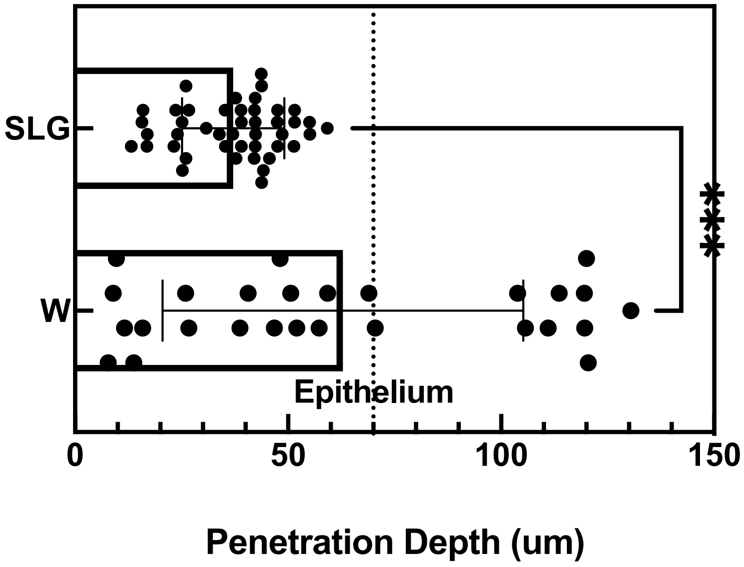

Figure 3.10: A comparison of penetration depths achieved by soda lime glass vs tungsten particles in *ex vivo* porcine cornea. Points represent the depth of one particle within a pooled set of n = 3 samples of each particle material. Dashed line represents the average epithelium thickness of 70 µm. *** = $p < 0.0001$

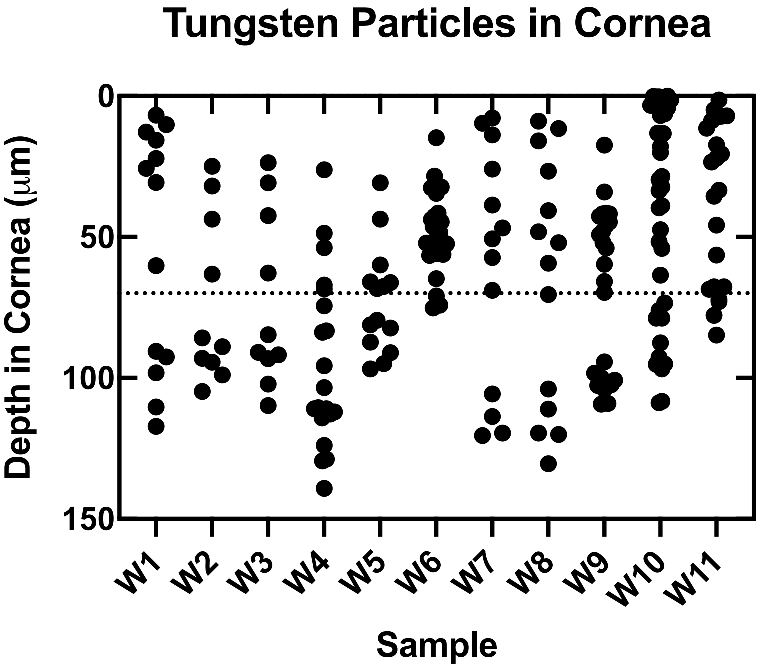

Figure 3.11: Penetration depths of tungsten particles in *ex vivo* corneas. 11 replicates are shown. Dashed line represents the average epithelium thickness. Tungsten particles consistently enter the stroma.

References

[1] Y.-H. Hwang et al. “Suspended Onion Particles and Potential Corneal Injury in Onion Harvesters”. In: *Archives of Environmental Health: An International Journal* 57.1 (Jan. 2002), pp. 78–84. ISSN: 0003-9896. DOI: `10.1080/00039890209602920`.

[2] P. S. Krishnacharya. “A case study of blast eye injury at work place”. In: *Burns & Trauma* 1.3 (2013), pp. 2321–3868.

[3] A. Abulafia et al. “Party foam-induced eye injuries and the power of media intervention”. In: *Cornea* 32.6 (2013), pp. 826–829.

[4] M. A. Al-Amry and H. A. Al-Ghadeer. “Corneal epitheliopathy after trauma by fake snow powder in a 7-year-old child”. In: *Middle East African journal of ophthalmology* 23.3 (2016), p. 274.

[5] E. C. Figueira, I. C. Francis, and G. A. Wilcsek. “Intraorbital glass foreign body missed on CT imaging”. In: *Ophthalmic Plastic & Reconstructive Surgery* 23.1 (2007), pp. 80–82.

[6] E. J. Snider et al. “Development and characterization of a benchtop corneal puncture injury model”. In: *Scientific reports* 10.1 (2020), p. 4218.

[7] B. Laccetti and J. Kornfield. “Ballistic delivery of compounds to inner layers of the cornea is limited by tough mechanical properties of stromal tissue”. In: *Journal of the Mechanical Behavior of Biomedical Materials* 115 (2021), p. 104246.

[8] D. Bauer et al. “Immunomodulation by topical particle-mediated administration of cytokine plasmid DNA suppresses herpetic stromal keratitis without impairment of antiviral defense”. In: *Graefe’s Archive for Clinical and Experimental Ophthalmology* 244 (2006), pp. 216–225.

[9] D. Bauer et al. “Particle-mediated administration of plasmid DNA on corneas of BALB/c mice”. In: *Biolistic DNA Delivery: Methods and Protocols* (2013), pp. 215–220.

[10] J. Hao et al. “Gene delivery to cornea”. In: *Brain research bulletin* 81.2-3 (2010), pp. 256–261.

[11] I. S. Zagon et al. “Regulation of corneal repair by particle-mediated gene transfer of opioid growth factor receptor complementary DNA”. In: *Archives of Ophthalmology* 124.11 (2006), pp. 1620–1624.

[12] Y. Danjo, L. D. Hazlett, and I. K. Gipson. “C57BL/6 mice lacking Muc1 show no ocular surface phenotype”. In: *Investigative ophthalmology & visual science* 41.13 (2000), pp. 4080–4084.

[13] R. Kardon et al. “Bacterial conjunctivitis in Muc1 null mice.” In: *Investigative ophthalmology & visual science* 40.7 (1999), pp. 1328–1335.

[14] T. D. Blalock et al. “Functions of MUC16 in corneal epithelial cells”. In: *Investigative ophthalmology & visual science* 48.10 (2007), pp. 4509–4518.

[15] P. Argüeso et al. “Mucin characteristics of human corneal-limbal epithelial cells that exclude the rose bengal anionic dye”. In: *Investigative ophthalmology & visual science* 47.1 (2006), pp. 113–119.

[16] M. Ruponen and A. Urtti. “Undefined role of mucus as a barrier in ocular drug delivery”. In: *European Journal of Pharmaceutics and Biopharmaceutics* 96 (2015), pp. 442–446.

Chapter 4

[INTENTIONALLY REDACTED]

Chapter 5

[INTENTIONALLY REDACTED]